

# **Systematic Studies on Reconstruction Efficiency at Belle II**

von

**Martin Sobotzik**

Masterarbeit in Physik  
vorgelegt dem Fachbereich Physik, Mathematik und Informatik (FB 08)  
der Johannes Gutenberg-Universität Mainz  
am 3. Dezember 2019

1. Gutachter: Prof. Dr. Wolfgang Gradl
2. Gutachter: Prof. Dr. Habe Dünkel



Ich versichere, dass ich die Arbeit selbstständig verfasst und keine anderen als die angegebenen Quellen und Hilfsmittel benutzt sowie Zitate kenntlich gemacht habe.

Mainz, den 03.12.2019 [Unterschrift]

Martin Sobotzik  
Institut für Kernphysik  
Johannes-Joachim-Becher-Weg 45  
Johannes Gutenberg-Universität D-55128 Mainz  
[msobotzi@students.uni-mainz.de](mailto:msobotzi@students.uni-mainz.de)



*Take two steps north into the  
unsettled future, south into the  
unquiet past, east into the present  
day, or west into the great unknown.*

---

~ Unknown

As the proverb says, a picture is  
worth a thousand words...

---



---

## Contents

<b>1. Introduction</b>	<b>1</b>
<b>2. Theoretical Foundations</b>	<b>3</b>
2.1. The Standard Model . . . . .	3
2.2. Physics Beyond The Standard Model . . . . .	5
2.3. Bhabha Scattering . . . . .	5
2.3.1. Bhabha Process . . . . .	5
2.3.2. Differential Cross Section Of Bhabha Processes . . . . .	6
2.3.3. Bhabha Kinematics At Belle II . . . . .	7
<b>3. Experimental Setup At SuperKEKB</b>	<b>11</b>
3.1. KEKB And SuperKEKB . . . . .	11
3.2. The Belle II Detector . . . . .	13
3.3. Coordinate System . . . . .	15
3.4. Vertex detector . . . . .	15
3.4.1. Pixel Vertex Detector . . . . .	16
3.4.2. Silicon Vertex Detector . . . . .	18
3.5. Central Drift Chamber . . . . .	18
3.6. TOP And ARICH . . . . .	20
3.7. Electromagnetic Calorimeter . . . . .	22
3.8. $K_L^0$ And Muon Detector . . . . .	23
<b>4. Trigger And Data Acquisition System</b>	<b>25</b>
4.1. Trigger . . . . .	25
4.2. Data Acquisition System . . . . .	26
<b>5. Tools</b>	<b>29</b>
5.1. Basf2 . . . . .	29
5.2. GridKa . . . . .	29
<b>6. Preparation For Calculating The Tracking Efficiency Of Phase2</b>	<b>31</b>
6.1. Phase2 . . . . .	31
6.2. Definition Of Tracking Efficiency . . . . .	31

## *Contents*

6.3. Reconstructing Bhabha Events With Basf2 . . . . .	32
6.4. Best Candidate Selection On Phase2 Monte Carlo . . . . .	34
6.4.1. ECL-Cut . . . . .	34
6.4.2. Mass-Cut . . . . .	35
6.4.3. Additional Cuts . . . . .	36
6.4.4. Cut Efficiency . . . . .	38
6.4.5. No MC-Truth Information . . . . .	39
6.5. Best Candidate Selection on Phase2 Data . . . . .	39
6.6. Selecting Bhabha Events . . . . .	41
6.7. ECL-Trigger . . . . .	44
6.8. More Events . . . . .	45
6.9. Dividing The ECL In Areas Of Interest . . . . .	45
<b>7. Phase2 Tracking Efficiency</b>	<b>53</b>
7.1. Momentum Efficiencies . . . . .	53
7.1.1. Forward End Cap . . . . .	53
7.1.2. Barrel . . . . .	55
7.1.3. Backward End Cap . . . . .	58
7.1.4. $\theta$ Efficiencies . . . . .	60
7.2. Transverse Momentum Efficiencies . . . . .	64
7.2.1. Forward End Cap . . . . .	64
7.2.2. Barrel . . . . .	65
7.2.3. Backward End Cap . . . . .	67
7.2.4. $\theta$ Efficiencies . . . . .	68
<b>8. Phase3 Tracking Efficiency</b>	<b>71</b>
8.1. Phase3 . . . . .	71
8.2. Location . . . . .	71
8.3. Exp7 . . . . .	71
8.4. Exp8 . . . . .	71
8.5. Selected Candidates . . . . .	71
8.6. Tracking Efficiency . . . . .	71
<b>9. Conclusion</b>	<b>73</b>
<b>A. Additional Preparation Plots</b>	<b>75</b>
<b>B. Additional Phase2 Plots</b>	<b>91</b>
<b>List of Figures</b>	<b>117</b>
<b>List of Tables</b>	<b>121</b>
<b>Bibliography</b>	<b>123</b>

CHAPTER

# 1

---

## Introduction



---

# 2 Theoretical Foundations

THE first part of this chapter will give short introduction to the standard model of particle physics. The standard model of particle physics (SM) is a theory that describes three of the four fundamental known forces in the universe: the electromagnetic, the weak and the strong force.

At the current level of experimental precision and the reached energies so far, it is the best theory describing these forces.

Unfortunately, the standard model fails to explain a variety of different observations and since gravitation is not included in the standard model, it is easy to see that the standard model is not complete.

Finally this chapter will shortly describe the electron-positron scattering process, also known as Bhabha scattering, which plays a very important role in this thesis.

## 2.1. The Standard Model

The standard model is based on the idea that matter is made of particles with no internal structure. These particles can interact with each other by exchanging other particles which are associated to the fundamental forces. The standard model includes the *quantum electrodynamic* (QED), the *electroweak theory* (EWT) and the *quantum chromodynamic* (QCD) as well as the *Higgs mechanism*.

The QED describes all phenomena caused by photons ( $\gamma$ ) and charged point-like particles like electron and positrons. In the 1920s Paul Dirac laid the foundation for the QED while computing the coefficient of spontaneous emission of an atom. The description of the weak force (*quantum flavor dynamics*, QFD) and the QED got merged by Sheldon Glashow in the early 1960s. The exchange particles of the weak force are the  $Z$  and  $W^\pm$  *bosons*. A few years later, Steven Weinberg and Abdus Salam independently proposed a theory that included the *Higgs mechanism* whereby the *electroweak theory* (EWT) emerged. The Higgs mechanism is the reason why the *gauge bosons* have mass. Finally the standard model reached its modern form after combining the EWT and the theory of the strong interaction (*quantum chromodynamic*, QCD). This was done by Abraham Pais and Sam Treiman in 1975. The exchange particles for the strong force are the *gluons* ( $g$ ). They «glue» *quarks*

## 2. Theoretical Foundations

(fundamental particles) together, forming *hadrons* like *mesons* (even number of quarks) and *baryons* (odd number of quarks). [1]

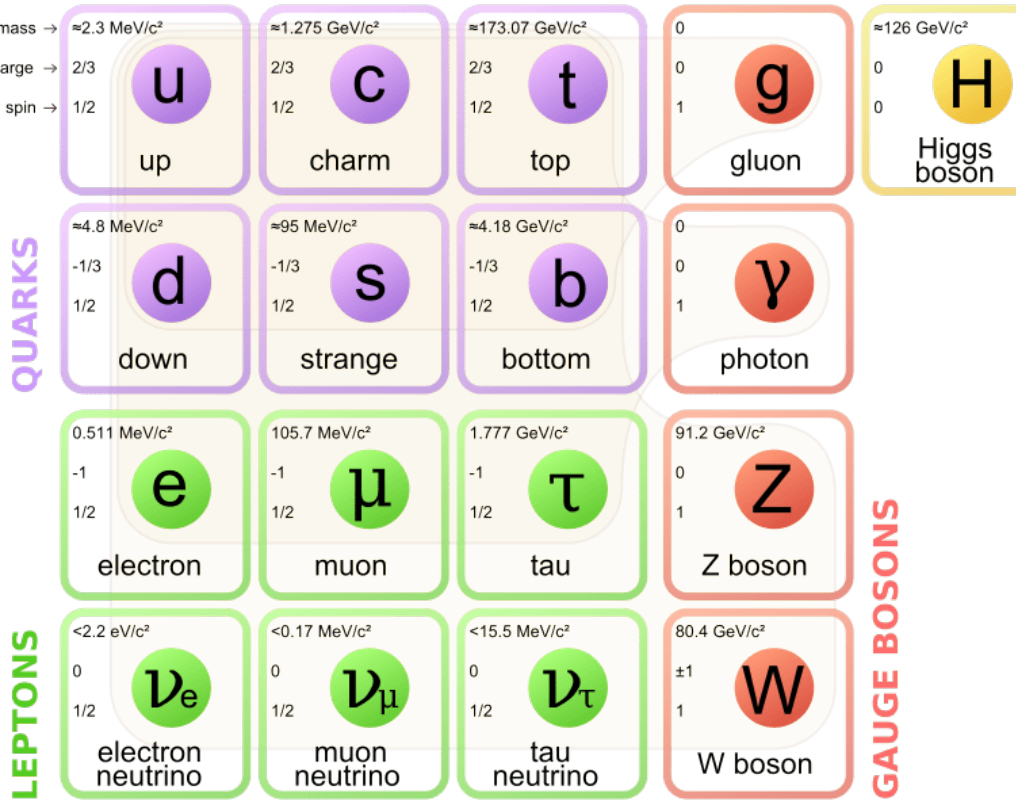


Figure 2.1.: The particles of the Standard Model include three families of quarks and leptons, four gauge bosons and the Higgs boson. The beige background indicates which bosons interact with which fermions. [2]

Figure 2.1 shows the fundamental particles of the standard model. It includes three families of quarks and leptons so-called *fermions*, four *gauge bosons* and the *Higgs boson*. Fermions and bosons differ by the spin. Spin is a degree of freedom, which had to be introduced to conserve the angular momentum in the Dirac equation. The matter forming fermions have a half-integral spin (in units of the reduced Planck constant  $\hbar$ ) and the bosons (the exchange particles as well as the Higgs particle) have an integer spin. The fermion family can be sectioned into two families. The quark and the lepton family. The quark family consists of up- ( $u$ ), down- ( $d$ ), strange- ( $s$ ), charm- ( $c$ ), bottom- ( $b$ ) and top- ( $t$ ) quark. Quarks have fractional electric charge values.  $u$ -,  $c$ - and  $t$ -quark have an electric charge of  $2/3 e$  and  $d$ -,  $s$ - and  $b$ -quark have an electric charge of  $-1/3 e$ . As indicated in figure 2.1 by the beige background, quarks can interact with all four gauge bosons. The lepton family is made of the electron ( $e$ ), the muon ( $\mu$ ) and the tau ( $\tau$ ) and their corresponding neutrinos  $\nu_e$ ,  $\nu_\mu$  and  $\nu_\tau$ .

## 2.2. Physics Beyond The Standard Model

The neutrinos can only interact via the weak exchange particles ( $W^\pm$  and  $Z$  bosons). Since the electrons, muons and taus are charged, they can also interact with photons. All fermions also have so-called *antiparticles*. Antiparticle have the same mass as their corresponding particle but they have opposite charge. For example, the antiparticle of the electron is the positron. Both have the same mass and the same spin but the electron has an electric charge of  $-1\text{ e}$  and the positron has an electric charge of  $+1\text{ e}$ . When a particle collides with its antiparticle annihilation can occur. In an annihilation process the incoming particles are destroyed to produce other particles. The final particles carry the same energy and momentum as the initial particles.

All visible matter in the universe is made of fermions from the first family. For example, atoms consist of protons and neutrons, each of which is a combination of up and down quarks. In the electron shell of an atom the eponymous electrons are located. Pauli proposed the neutrino in the 1930 to explain the energy spectrum of electrons in  $\beta$ -decays. Since neutrinos are only weak interacting particles, they were not observed until 1956.[3] With increasing energy, the second and third family have been gradually discovered, first from cosmic ray experiments in the 1930s up to the discovery of the Higgs boson at the Large Hadron Collider (LHC) at Cern in 2012. Parallel to the experimental discoveries, the theory also evolved, partially explaining the results and in part motivating new experiments through predictions.

## 2.2. Physics Beyond The Standard Model

Despite the success of the standard model as an effective theory, it fails answering a lot of open questions. As already mentioned, the standard model only includes three out of four fundamental forces. It does not include gravity, therefore, the standard model is not valid at energy scales approaching the Planck energy  $E_P \approx 1.22 \cdot 10^{19} \text{ GeV}$ .[4] It is also unable to explain dark matter, dark energy and the matter/antimatter asymmetry in the universe which is directly linked to charged-parity violation.[5]

## 2.3. Bhabha Scattering

In this section, we want to shortly discuss Bhabha scattering. We will start with the physics of Bhabha scattering and then discuss the Bhabha kinematics at Belle II.

### 2.3.1. Bhabha Process

Bhabha scattering is a quantum electromechanical process between an electron and a positron. It is named after the Indian physicist H. Bhabha who first derived the electron-positron scattering cross section in 1935.[6]

Bhabha scattering contains two different processes. Both have in common that there are an electron and positron in the initial and final state. Figure 2.2 shows the Feynman diagrams for both Bhabha processes. The time passes from the left to

## 2. Theoretical Foundations

the right side. In the left process, the initial electron and positron annihilate to form a virtual photon  $\gamma^*$ . This virtual photon then decays into an electron and a positron. The right Feynman diagram describes a classic electrodynamic scattering process. Here the incoming electron and positron are scattering by the interaction with a virtual photon. In contrast to the right diagram, the left diagram can only be explained by quantum field theory, due to the creation and destruction of particles.

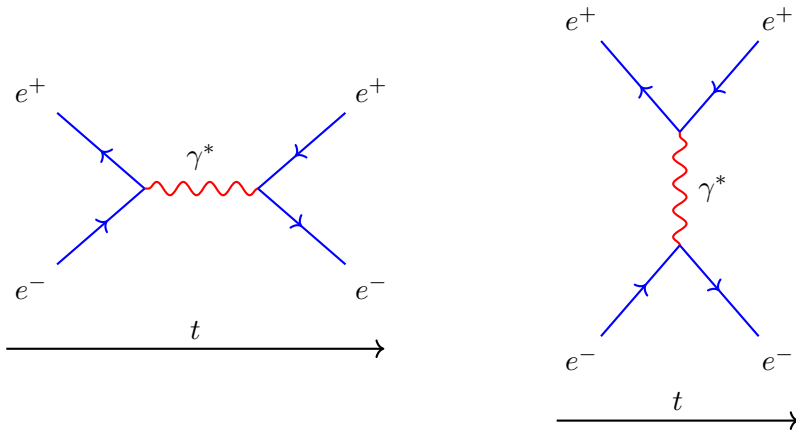


Figure 2.2.: The two Bhabha process Feynman diagrams. The left diagram describes the annihilation and pair production process, while the right diagram describes a classic electromagnetic scattering process.

### 2.3.2. Differential Cross Section Of Bhabha Processes

The cross section is the probability that two particle will interact with each other when they collide. If this collision creates secondary radiation, then the intensity distribution over the spatial direction  $\Omega$  is described by the differential cross section  $d\sigma/d\Omega$ .

The differential cross section for the electron<sup>1</sup> in a Bhabha process is given by equation 2.1.

$$\left(\frac{d\sigma}{d\Omega}\right)_{\text{cms}} = \frac{e^4}{32\pi^2 E^2} \left( \frac{1 + \cos^2(\theta)}{2} + \frac{1 + \cos^4(\theta/2)}{\sin^4(\theta/2)} - \frac{2\cos^4(\theta/2)}{\sin^2(\theta/2)} \right) \quad (2.1)$$

In figure 2.3 on the left, the differential cross section for electrons is plotted. Since, most incoming particles are only very slightly deflected, the cross section is very high for small angels and gets smaller with increasing angle. Equation 2.1 is also true for positron but since they are moving in the opposite direction,  $\theta$  in the equation has to be replaced by  $\pi - \theta$ . This result is plotted in figure 2.3 on the right.

---

<sup>1</sup>The electrons are moving along the x-axis. The positrons are moving in the opposite direction

### 2.3. Bhabha Scattering

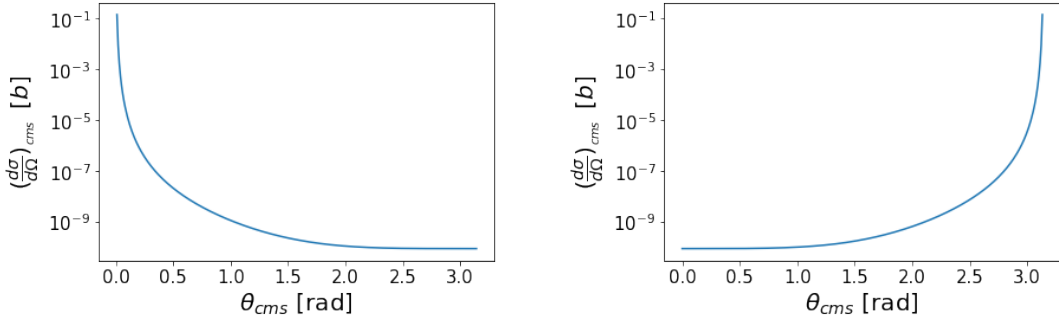


Figure 2.3.: Differential cross-section for Bhabha events. Left: The Cross-section for electrons is shown and on the left for positrons.  
These plots were created with python3.

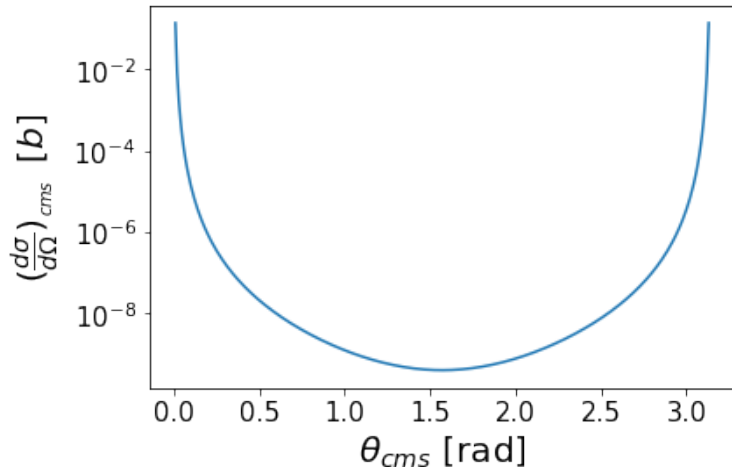


Figure 2.4.: This figure shows to differential cross section for Bhabha events.  
This plot was created with python3.

To get to differential cross section for Bhabha events, one has to add the differential cross section of electrons and positrons. This is shown in figure 2.4. As you can see, most of the outgoing particles will have a very small or very large  $\theta$  angle.

#### 2.3.3. Bhabha Kinematics At Belle II

At Belle II the electron and the positron beams have different energies. Also, they are hitting each other under an angle. Therefore, it is interesting to look at the Bhabha kinematics in the lab system of Belle II.

Figure 2.5 on the left, you can see the momentum of the Bhabha particles as a function of the  $\theta$  angle in the center of mass frame. Since the incoming electron and the positron have the same mass and they are hitting each other with the same energy, the outgoing

## 2. Theoretical Foundations

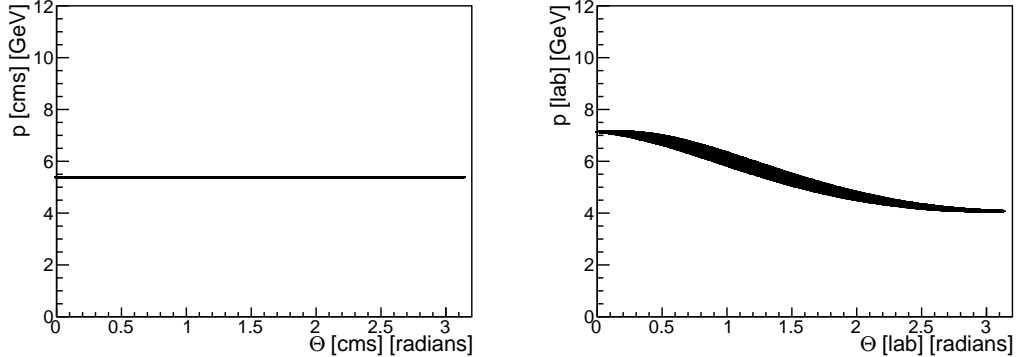


Figure 2.5.: Bhabha scattering in different frames. In the cms the particle has the same Belle II energy in every  $\theta$ -direction. Left: The  $\theta$ -Energy-distribution in the cms frame is shown. Right: The  $\theta$ -Energy-distribution in the lab frame is shown.

particles always have the same momentum independent of the  $\theta$  angle in the center of mass frame. In the right plot, you can see the momentum distribution after the boost in the lab system. For small  $\theta$  angles a higher momentum of the outgoing particles is expected compared to high  $\theta$  angles. The fanning of the distribution is caused by the fact that the beams are hitting each other under an angle at BelleII. Also, due to the fanning, we expect a range of energies at a fixed  $\theta$  angle.

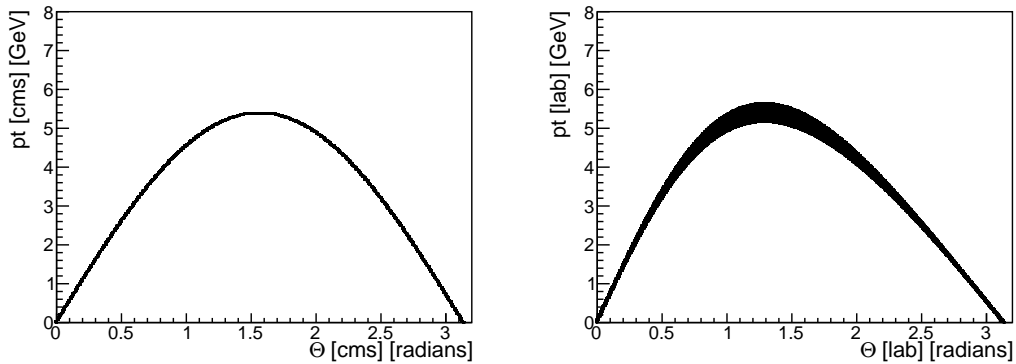


Figure 2.6.: The transverse momentum of the outgoing Bhabha particles in different frames. Left: transverse momentum in the center of mass frame. The highest transverse momentum is expected at an  $\theta$  angle of  $\pi/2$ . Right: The transverse momentum in the lab frame. The highest transverse momentum is shifted a bit to smaller values of  $\theta$ .

Figure 2.6 shows the transverse momentum as a function of  $\theta$  for the outgoing Bhabha particles at BelleII. The left plot shows the distribution in the center of mass frame,

### 2.3. Bhabha Scattering

while the right plots shows it for the lab frame. In both frames, we expect the highest transverse momentum at an  $\theta$  angle of about  $\pi/2$ .

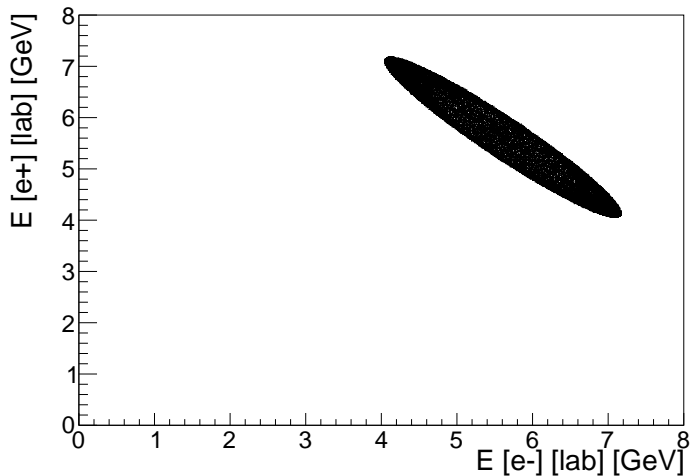


Figure 2.7.: The energy of the two outgoing Bhabha particles in the lab frame at BelleII.

In figure 2.7 the energy of the outgoing Bhabha particles in the lab frame at BelleII are plotted against each other. As you can see, if for example the electron has an energy of 7 GeV than the positron will have an energy of just about 4 GeV and vice versa.



# 3

---

## Experimental Setup At SuperKEKB

SUPERKEKB is an two-ring, asymmetric<sup>1</sup>, electron positron accelerator, which is located at KEK (*High Energy Accelerator Research Organization*) in Tsukuba Japan. The electron beam has an energy of 7 GeV and the positron beam has an energy of 4 GeV. These beams collide with a center-of-momentum energy of about 10.58 GeV, which is close to the mass of the  $\Upsilon(4S)$  resonance. Therefore SuperKEKB is a so-called *B-factory*. The decay products are then detected by the Belle II detector to study the properties of these B mesons with high precision. In early 2018 Belle II started taking data. One goal of Belle II is to study CP-Violation with respect to new physics.[7]

### 3.1. KEKB And SuperKEKB

This section will only provide a rough overview of the SuperKEKB accelerator since the focus of this work is on the analysis.

SuperKEKB is an upgrade of the KEKB accelerator. KEKB was also an asymmetric electron positron accelerator in the period from 1998 to 2010, but the energies were different compared to SuperKEKB. At KEKB the electrons were accelerated to an energy of 8 GeV and the positrons to an energy of 3.5 GeV. KEKB was also a B-factory and the reaction products were then detected in the Belle detector. In 2009 KEKB achieved an instantaneous luminosity of  $\mathcal{L} = 2.11 \cdot 10^{34} \text{ cm}^{-2}\text{s}^{-1}$ . This was the world record at that time. KEKB was discontinued after more than 10 years, to be upgraded to SuperKEKB.[8]

In figure 3.1 you can see the schematic layout of the SuperKEKB accelerator. The electrons are start at the Low emittance gun. They are then accelerated in the *J*-shaped linear particle accelerator (linac). Due to lack of space, the linac has to have this special form.[10] After the curve and a second acceleration stage the electrons hit the positron production target, where the positrons are created. After this target there are more acceleration stages, before the two beam are then injected into their independent storage rings. The electrons are stored in the high-energy ring (HER)

---

<sup>1</sup>asymmetric means that there is an energy difference between the two colliding beams

### 3. Experimental Setup At SuperKEKB

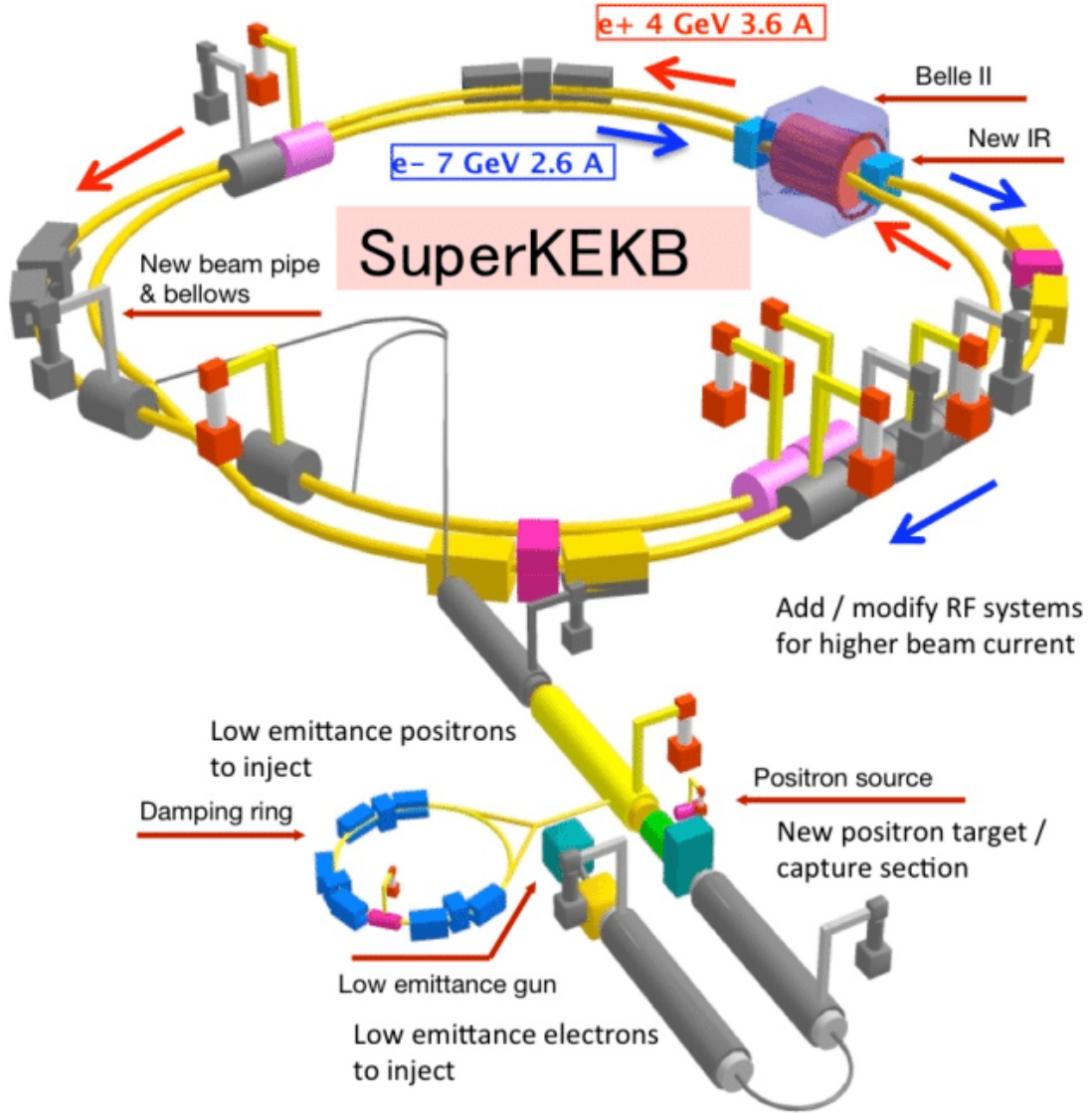


Figure 3.1.: The SuperKEKB collider.[9]

and the positrons are stored in the low-energy ring (LER). Each of these rings has a circumference of about 3 km. Both beams collide at the interaction region (IR). The products of the collisions are then detected by the Belle II detector, an upgraded version of the Belle detector.[7] (See chapter 3.2)

SuperKEKB uses a smaller asymmetry in the beam energies compared to KEKB. This allows the usage for higher beam currents and better focusing magnets. This can then result into a higher luminosity. The goal is to achieve a 40 times higher luminosity

### 3.2. The Belle II Detector

with SuperKEKB compared to KEKB. An integrated luminosity of  $50 \text{ ab}^{-1}$  will be achieved by 2025.[7]

The instantaneous luminosity  $\mathcal{L}$  specifies the performance of the collider. Knowing  $\mathcal{L}$  and the cross section  $\sigma$  one can calculate the events per second for a process by the following formula.

$$\frac{dN}{dt} = \mathcal{L} \cdot \sigma \quad (3.1)$$

To increase the event rate one has to increase the instantaneous luminosity since  $\sigma$  is given by the processes. The instantaneous luminosity can be calculated by

$$\mathcal{L} = \frac{N_{e^-} N_{e^+} f_c}{4\pi \sigma_x \sigma_y} \cdot S \quad (3.2)$$

assuming that both beams have a Gaussian profile of horizontal and vertical size  $\sigma_x$  and  $\sigma_y$ . In equation 3.2  $N_{e^-}$  is the number of particles in an electron bunch and  $N_{e^+}$  is the number of particles in a positron bunch.  $f_c$  is the average crossing rate, which can be calculated by  $f_c = n \cdot f_r$ . Where  $n$  is the number of bunches and  $f_r$  is the revolution frequency.  $S$  is a reduction factor which takes geometrical effects linked to the finite cross section and bunch length into account.[11] SuperKEKB increased the luminosity by a factor of two compared to KEKB by increasing the number of bunches and the number of particles per bunch.

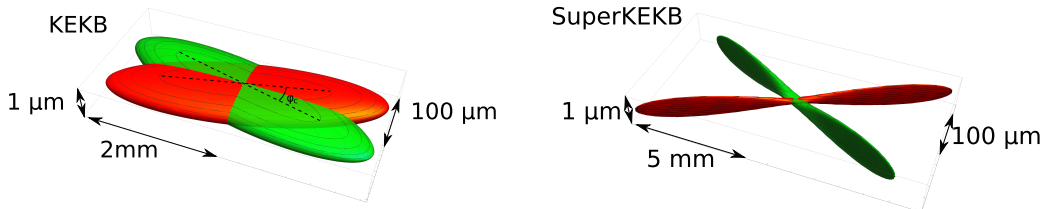


Figure 3.2.: Sketch of the beam crossing at KEKB (left) and SuperKEKB (right).

At KEKB the size of the interaction region was about 10 mm. At SuperKEKB it is about 0.5 mm.[12] This figure was edited in order to make the axis more readable.

Also the size of the interaction region at SuperKEKB is just one twentieth of what it was at KEKB, resulting in a vertical beam size of  $\sigma \approx 50 \text{ nm}$ . This can be seen in figure 3.2. This decrease in beam size, along with the increase in the beam currents, it results in a overall 40-fold increase in luminosity. [13] [7]

## 3.2. The Belle II Detector

The Belle II detector is an upgraded version of the Belle detector which was a solid-angle magnetic spectrometer located at the interaction region of KEK. In figure 3.3 a sketch of the Belle II detector is shown. The detector contains of a variety of sub-detectors, each fulfilling a specific purpose.

### 3. Experimental Setup At SuperKEKB

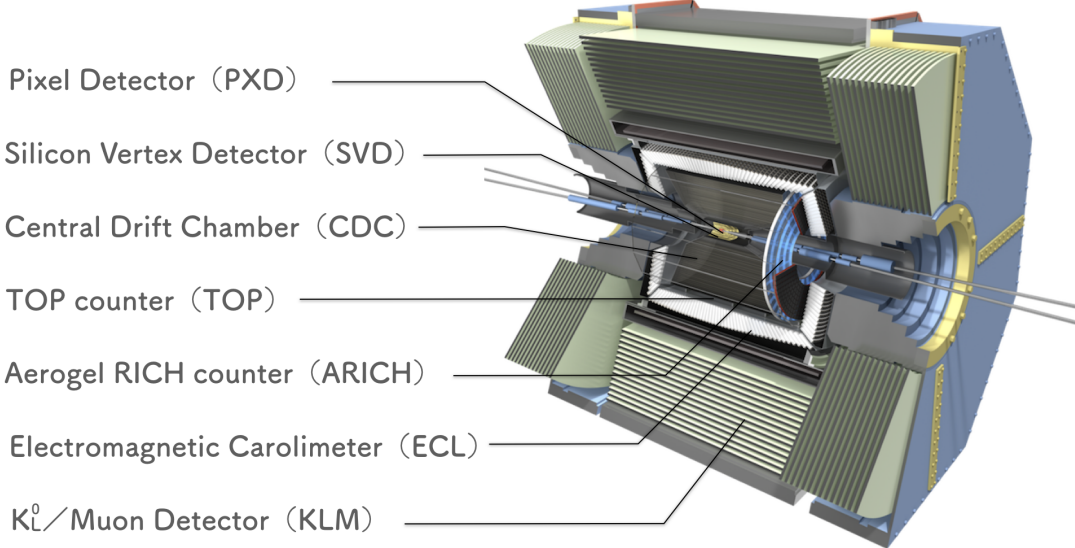


Figure 3.3.: Schematic view of the Belle II detector. The different detector elements are labeled. Also the beam pipes for the electrons and positrons with their corresponding energies are shown. [14] This figure was modified in order to make the text more readable.

In the innermost of the detector, three tracking sub-detectors are located, surrounding the IR. These sub-detectors are in a axial magnetic field of 1.5 T, provided by a solenoid, to be able to reconstruct the tracks of charged particles.

The vertex detectors, consisting of the silicon vertex detector (SVD), an upgraded version of the SVD used in Belle, and the pixel detector (PXD), a new detector designed for Belle II, are used to measure the momenta of charged particles and to reconstruct decay vertices and particles with a momentum to low to reach the central drift chamber (CDC).

The CDC also already existed in the Belle detector and has been upgraded for Belle II. The CDC scans the trajectories of charged particles. From these trajectories the charge, momentum and energy loss can be determined by ionization.

These three innermost tracking detectors are surrounded by a barrel. The time-of-propagation (TOP) detector, which also got an upgrade for Belle II, surrounds the inner detectors parallel to the beam-pipes. The TOP detector, as the name suggests, measures the flight-time of charged particles. Knowing the flight-time and the momentum of the charged particles, it is possible to conclude their mass and to identify them. In the forward end-cap of the barrel are closed with an Aerogel Ring-Imaging Cerenkov detector (ARICH) which also identifies charged particles.

The next outer detector is the electromagnetic calorimeter (ECL). It surrounds all the previously mentioned detectors, and was already installed in Belle. With the ECL the

### 3.3. Coordinate System

energy of electromagnetically interacting particles, especially photons and electrons, can be measured.

The task of the outermost detector the  $K_L^0$  and muon detector (KLM) is to identify  $K_L^0$  and muons. The KLM also got upgraded for Belle II. [7]

## 3.3. Coordinate System

For clarification, the coordinate system of Belle II will be described in this section, before the detectors are explained in more detail.

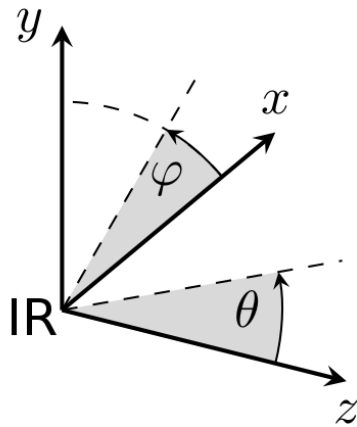


Figure 3.4.: A sketch of the coordinate system of Belle II. The original figure was modified to make the coordinate system more visible. [15]

A sketch of the coordinate system is shown in figure 3.4. The origin of the coordinate system corresponds to the interaction region. For the Cartesian coordinate system: The  $z$ -axis points in the direction of the magnetic field. This is also the so-called forward direction. The  $y$ -axis points up to the upper part of the detector. The  $x$ -axis points along the radial direction of the accelerator. The electrons are moving roughly along the positive  $z$  axis, while the positrons are moving in the opposite direction. In figure 3.4 also the spherical coordinate system is shown. Here  $\theta$  corresponds to the polar angle and  $\phi$  to the azimuthal angle.[16]

## 3.4. Vertex detector

The vertex detectors (VXD) is able to make precise measurements of the tracks of particles close to the interaction region. This allows the reconstruction of decay-vertices of long-lived particles. For this it is very important to determine the distance and the spatial resolution of the first measured hit, and the effect of multiple scattering. The VXD consists of the pixel vertex detector and the silicon vertex detector, both can be seen in figure 3.5. These two detectors complement each other.

### 3. Experimental Setup At SuperKEKB



Figure 3.5.: Sketch of the vertex detectors. The vertex detector itself consists of two sub-detectors. The PXD is surrounded by the SVD. [17]

#### 3.4.1. Pixel Vertex Detector

The purpose of the PXD is to reconstruct the spatial position of the decay vertices of  $B$ ,  $D$  and  $\tau$ . The PXD is based on Depleted P-channel Field-Effect Transistor (DePFET) technology. This technology allows the sensors of the PXD to be very thin ( $50\ \mu\text{m}$ ).

As you can see in figure 3.6, the PXD consists of two layers of sensors. The inner layer is made out of eight planar sensors (ladder), each has a width of 15 mm and an effective length of 90 mm. This layer has a radius of 14 mm. The second layer consists of 12 planar sensors. These sensors also have a width of 15 mm, but a length of 123 mm. The radius for the second layer is 22 mm. The PXD provides a spatial resolution of about  $1.2\ \mu\text{m}$ .[13]

Due to the vicinity of the PXD to the interaction region, the quantum-electrodynamics background is very high, so the sensors must withstand high radiation. The DePFET technology fulfills this condition. [13] [18]

### 3.4. Vertex detector



Figure 3.6.: Sketch of the PXD [13]

DePFET is a semiconductor detector concept invented in 1987 by J. Kemmer and G. Lutz of the MPI for Physics. This concepts combines detection and amplification in one single device. [13]

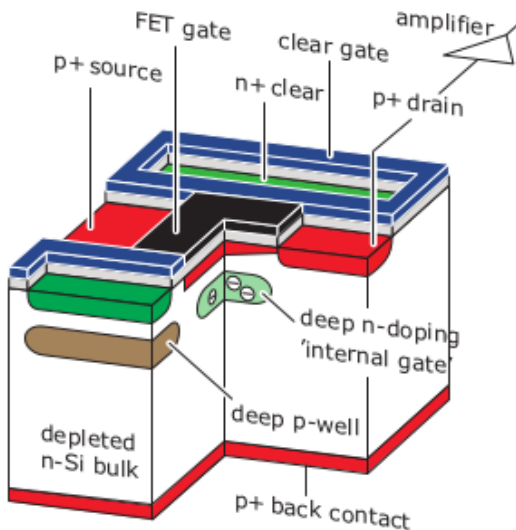


Figure 3.7.: Illustration of the DePFET technology.[13]

### 3. Experimental Setup At SuperKEKB

A cross section of the device is shown in figure 3.7. The structure of a DePFET cell consists of fully depleted silicon. In this silicon substrate depleted by a high negative voltage a  $p$ -channel MOSFET (metal oxide semiconductor field effect transistor) or a JFET (junction field effect transistor) is integrated. The field effect transistors act as a first pre-intensification. When radiation or a particle hits the detector, electron-hole pairs are created. These pairs get separated by the potential field of the sideward depletion. The positive charged holes drift to the negatively charged back contact. The negative charged electrons are collected in the potential minimum. The so-called internal gate. Above the internal gate a field emission transistor is located. The signal charged is amplified right above the position where it was generated. This avoids the leakage of lateral charge transfers. One of the most important main features of the DePFET is that the internal gate has a very small capacitance. This makes it possible to measure events affected by low noise even at room temperature.[13]

#### 3.4.2. Silicon Vertex Detector

The SVD consists of four layers of double-sided strip detectors. The layers are located at radii of 38, 80, 115 and 140 mm. There are two different shapes of these sensors. The rectangular sensors are used in the barrel part and the trapezoidal sensors are used in the forward region of the SVD. Each sensor has a thickness of  $320\ \mu\text{m}$  but the sensors have different dimensions depending on the layer they are located. The barrel sensors in the most inner layer of the SVD have a dimension of  $38.4 \times 122.8\ \text{mm}^2$ . The size for the barrel sensors of the other layers is  $57.6 \times 122.8\ \text{mm}^2$ . The trapezoidal sensors have a dimension of 38.4 mm on the small side of the trapez to 57.6 mm on the long side of the trapez times a length of 122.8 mm.[13] An illustration of the SVD can be seen in figure 3.8.

In the barrel region the  $p$ -side of the double-sided-strip sensors is arranged parallel to the beam axis and facing the interaction region. The  $n$ -side is facing outside the detector and the  $n$ -strips are perpendicular arranged to the beam axis.

When a particles travels through the sensors it creates electron-holes pairs along its path by ionization. The electrons then propagate to the  $n$ -strips and are accumulated there. The holes propagate to the  $p$ -strips and are collected there. The sensors then produce a signal from which the coordinate of the particle position can be read out. The  $p$ -side provides the  $z$ -direction and the  $n$ -side provides the  $r - \theta$  direction.[13] [20]

### 3.5. Central Drift Chamber

The CDC surrounds the SVD. It consists of 14336 wires arranged in 56 layers and has an inner radius of 16 cm and an outer radius of 113 cm. The volume is filled with a 50 % helium and an 50 % ethane gas mixture. The purpose of the CDC is to reconstruct the momenta and tracks of charged particles, to identify these particles by measuring their specific energy loss within the gas volume. The CDC alone is able to identify low-momentum tracks, which are unable to reach the particle identification

### 3.5. Central Drift Chamber

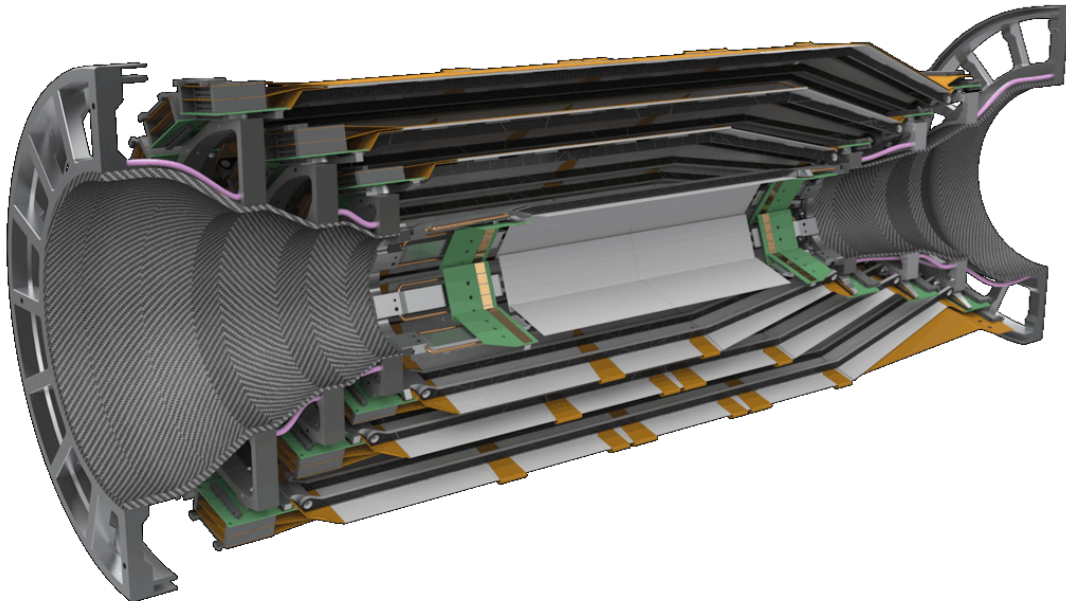


Figure 3.8.: Cross section of the silicon vertex detector[19]

device. The CDC also acts as a reliable trigger for charged particles.[13] A small cross section of the CDC is shown in figure 3.9.

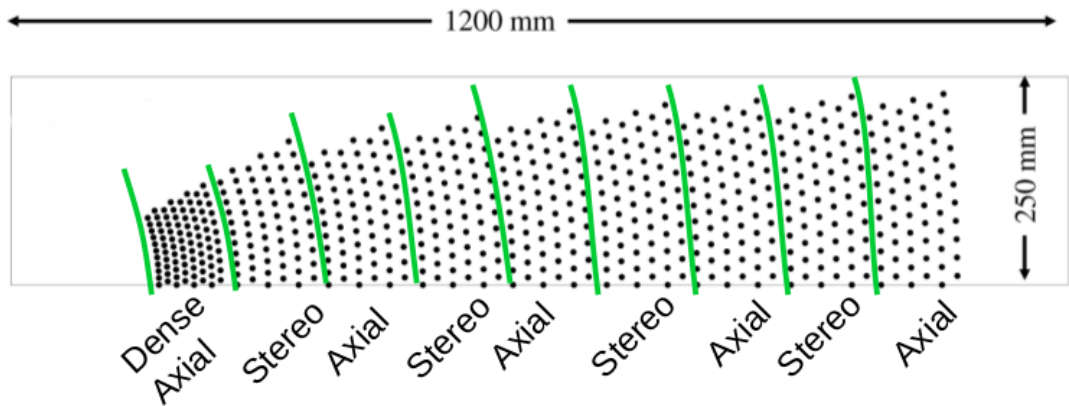


Figure 3.9.: Cross section and only a small part of the CDC. Each dot represent a wire. Also the area for the different superlayers is shown by the green line. All of these wires are immersed in a helium-ethane mixture.[21]

When a charged particle passes through the CDC it loses energy due to ionization of the gas. This produces electron-ion pairs, which are then separated by the electric field provided by 42240 aluminum field wires, with a diameter of  $125 \mu\text{m}$ . The signal

### 3. Experimental Setup At SuperKEKB

is then read out by the sense wires. These have a radius of  $30\ \mu\text{m}$  and are made out of gold-plated tungsten.[13]

As indicated in figure 3.9 there are different superlayers in the CDC. The Dense Axial and Axial sense wires allow the reconstruction of the track in the  $r - \phi$  plane. The stereo sense wires gives information about the  $z$  direction. These stereo wires are tilted in respect to the  $z$  direction. Six layers of sense wires are combined to a superlayer. The CDC consists of five axial superlayers (A), and four stereo superlayer. The four stereo superlayer subdivide into two stereo superlayer (U) with a positive stereo angle and two stereo superlayers (V) with a negative stereo angle. Starting with the innermost superlayer, every second superlayer is an axial superlayer. The stereo superlayers are between them, alternating between U and V. In total there are nine superlayers. The innermost superlayer is called *small-cell chamber* has a total of eight superlayers. (compared to the other superlayers with just six layers) This was done to lower the influence of the background, which is higher in the innermost superlayer due to the vicinity to the interaction region. The CDC has a spatial resolution of about  $100\ \mu\text{m}$ .[13]

## 3.6. TOP And ARICH

There are two additional detectors for particle identification, the TOP and the ARICH. The TOP counter is located in the barrel part and it uses a combination of time-of-flight and Cerenkov angle measurements. When a charged particle with the velocity  $\beta$  is faster than the speed of light  $c_n$  in a medium with a reflective index  $n$  then this particle emits Cerenkov radiation under the angle  $\theta_C$ .[22]

$$c_n = \frac{c_0}{n} \leq \beta \quad (3.3)$$

The Cerenkov angle is given by:[22]

$$\cos(\theta_C) = \frac{1}{n\beta} \quad (3.4)$$

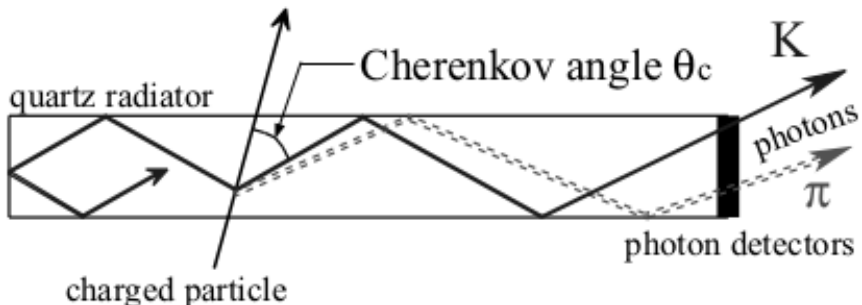


Figure 3.10.: Operating mode of a TOP detector.[13]

### 3.6. TOP And ARICH

Figure 3.10 shows an illustration of the functionality of a TOP bar. The charged particle emits Cerenkov light when it passes the quartz crystal. These photons then travel inside the crystal due to reflection until they are detected by a photon detector. Measuring the time difference between the emitted photons it is possible to calculate the position of the track of the charged particle. The outgoing photons are then focused by mirrors and are then detected by PMTs. Cerenkov photons with different  $\theta_C$  will be detected by different PMTs. Therefore, the TOP reconstructs the Cerenkov ring image using the information of time,  $x$  and  $y$ .[13]

The TOP counter consists of 32 quartz bars. They have a length of 1250 mm, a width of 45 mm and a depth of 20 mm. There are two quartz bars per module. The TOP counter has a  $K/\pi$  separation of over 99 %.[13]

The ARICH detector is located in the forward endcap region. It is designed to distinguish between kaons and pions over most of their momentum spectrum. It is also able to identify particles with a momentum below 1 GeV.

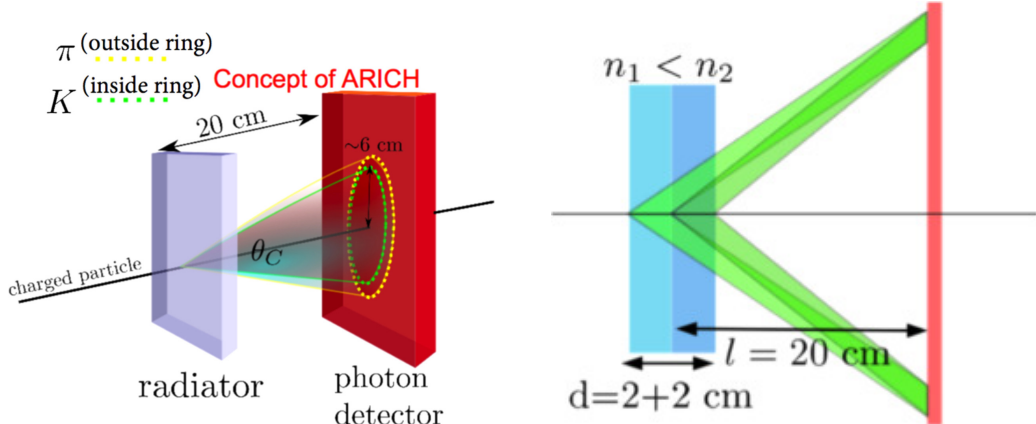


Figure 3.11.: Left: Illustration of the working principle of the ARICH detector. The yellow Cerenkov ring on the photon detector is produced by a  $\pi$ , the green ring by a  $K$ . Right: The radiator is shown in more detail. The radiator consists of two aerogel layers with different reflective indexes. [23]

In figure 3.11 the working principle of the ARICH detector is shown. A charged particle passes through two layers of an aerogel radiator with different reflective indexes and emits Cerenkov photons under an Cerenkov angle  $\theta_C$ . Behind the radiator is an extension volume for the Cerenkov rings to form. At a distance of 20 cm behind the radiator is the photon detector.[13] Once the Cerenkov ring is reconstructed, the radius of the ring can be determined and, knowing the distance and the radius, the Cerenkov angle can be calculated.

### 3. Experimental Setup At SuperKEKB

#### 3.7. Electromagnetic Calorimeter

One of the main tasks of the ECL is the detection of photons with a high efficiency. It also determines the energy and the angular coordinates of these photons with high precision. It is also used for electron identification and the generation of a proper signal for the trigger. The ECL consists of a 3 m long barrel section with an inner radius of 1.25 m. The circular endcaps are located at a distance of  $z = 1.96$  m in the forward direction and  $z = -1.02$  m in the backward direction from the interaction point. The ECL covers a polar angle region of  $12.4^\circ < \theta < 155.1^\circ$ . Due to construction, there are two  $\sim 1^\circ$  wide gaps between the barrel and the endcaps. The barrel section of the calorimeter consists of 6624 CsI(Tl)<sup>2</sup> crystals with 29 distinct shapes. Each of these crystals is a truncated pyramid with an average size of about  $6 \times 6 \text{ cm}^2$  in cross section and 30 cm in length. The length of these crystals corresponds to around 16.1 radiation lengths  $X_0$ . The endcaps consist of 2122 CsI crystals of 69 shapes. At the end of each crystal, photo-multiplier are mounted to detect the excitation of the scintillators. The detected number of photons corresponds directly to the energy released by absorbed particles. The energy resolution of the calorimeter can be approximated as:[13] [24]

$$\frac{\sigma_E}{E} = \sqrt{\left(\frac{0.066\%}{E}\right)^2 + \left(\frac{0.81\%}{\sqrt[4]{E}}\right)^2 + (1.34\%)^2} \quad (3.5)$$

The energy E is in GeV.

Photons and electromagnetic particles are creating electromagnetic cascades when they pass through material.[25] When a high energetic photon passes through a material it creates an electron-positron pair by pair production. For this, the photon must have at least an energy of  $2 \cdot m_{e^-} = 1.022 \text{ MeV}$ . This energy is evenly distributed between the two particles. Because these two particles are charged and their velocity changes in an the electric field of a nuclei, they generate photons through Bremsstrahlung. These processes are repeated and a electromagnetic shower is created. The energies of the particles continue to decrease until the critical energy  $E_c$  is reached. At the critical energy, the energy loss due to Bremsstrahlung is as high as the energy loss due to ionization.

If the average energy of an electron becomes  $E_0/e$  then the distance the electron traveled is called radiation length  $X_0$ .

Assuming that the electromagnetic particles and photons interact after one radiation length and that they loose half of their energy each time they do, the total number of particles and their energy after  $t$  cascades can then be calculated by:[25]

$$N \simeq 2^t \quad (3.6)$$

$$E(t) \simeq \frac{E_0}{2^t} \quad (3.7)$$

---

<sup>2</sup>Thallium activated Cesium Iodide

### 3.8. $K_L^0$ And Muon Detector

This shower both spreads longitudinally and transversely. The transverse propagation can be described by the Molière radius. It can be calculated by:

$$R_M = 21 \text{ MeV} \cdot \frac{X_0}{E_c} \quad (3.8)$$

95 % of all particles of a shower are within two Molière radii.[25]

## 3.8. $K_L^0$ And Muon Detector

The KLM consists of an alternating sandwich structure of a 4.7 cm thick iron plates and resistive plate chambers (RPC) in between.

RPCs consist of two glass sheets, separated by a thin gas volume. These sheets act as high voltage electrodes. When a particle passes through the volume, they create ion-electron pairs which are then accelerated by the strong electric field. They therefore initiate more ionizations, which leads to a streamer between the electrodes. This causes a voltage drop in the nearby electrodes, which is detected by pick-up strips, located on both sides of the chamber. These strips are a few centimeters wide and are placed orthogonal on each side. Therefore, the particle track can be localized in  $z/\phi$  for the barrel region and  $\phi/\theta$  for the endcaps.

To distinguish between muons and hadrons, the KLM takes advantage of the high penetration power of muons. Hadrons deplete their energy through hadronic showers in the ECL and KLM. Electrons have a shorter radiation length and are therefore absorbed by the ECL, most of the time.  $K_L^0$  create clusters in the ECL and the KLM. These clusters are than grouped and geometrically matched to charged tracks which are detected by the inner detectors. If no corresponding charged track can be found by geometrical matching, the detected particle is then treated as a  $K_L^0$  candidate.[13][26]



---

# 4 Trigger And Data Acquisition System

In this chapter a short introduction to the trigger system and the data acquisition system at Belle II is provided.

## 4.1. Trigger

The online event selection system (trigger) for Belle II makes it possible to acquire data from the detector based on information from a set of sub-detectors. The individual triggers are structured in an hierarchy. Each sub-trigger system provides the trigger information from the corresponding sub-detector to the global decision logic (GDL). This global trigger finally decides whether the event should be written out or not. [13] A schematic overview of this trigger hierarchy can be found in figure 4.1.

The trigger system has to fulfill the following requirements:[13]

0. high efficiency for hadronic events from  $\Upsilon(4S) \rightarrow B\bar{B}$  and from continuum
1. a maximum average trigger rate of 30 kHz
2. a fixed latency of about  $5\ \mu s$
3. a timing precision of less than 10 ns
4. a minimum two-event separation of 200 ns
5. a trigger configuration that is flexible and robust

At SuperKEKb bunch crossing happens almost continuously, since the radio-frequency (RF) is about 508 Hz and every second or third period produces an event.[13] The total cross section and trigger rates at a luminosity of  $\mathcal{L} = 8 \cdot 10^{35} \text{ cm}^{-2}\text{s}^{-1}$  for various physics processes is shown in table 4.1.

The luminosity is measured by using Bhabha and  $\gamma\gamma$  events. These events are also used to calibrate the detector response. Due to the high luminosity, these events are very dominant. That is the reason why there is a prescaling factor of 100 on these

#### 4. Trigger And Data Acquisition System

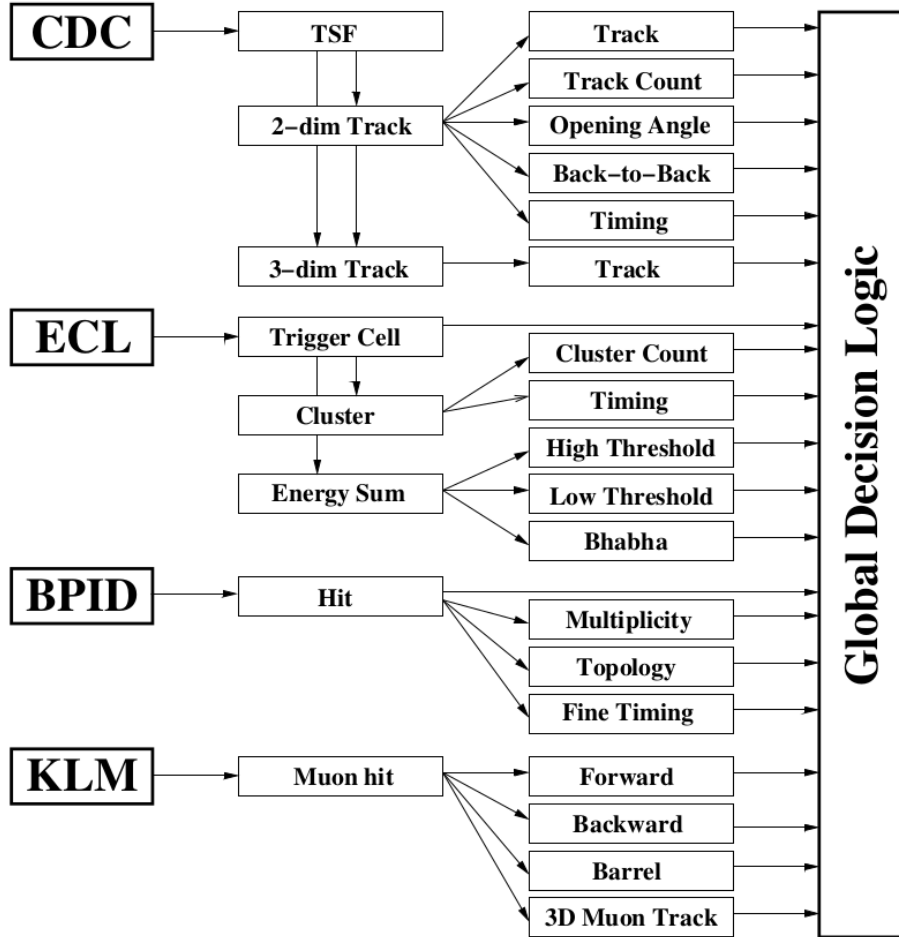


Figure 4.1.: Schematic overview of the Belle II trigger system. The four sub-trigger systems send their outputs to the Global Decision Logic. The GDL then performs the final online trigger decision. [27]

events. This means that on predetermined fraction of these events are accepted after satisfying the trigger requirements. After a beam collision, the GDL decides within about  $5\ \mu\text{s}$  if the event should be accepted and if it should be written out. Since the GDL is the first module to make a decision, and since it is dead time free, it is also called Level-1 trigger.[13]

## 4.2. Data Acquisition System

The data acquisition system (DAQ) reads out the detector signals once the Level-1 trigger decision is given by the trigger system. Starting from the front-end electronics, DAQ transfers the data through multiple steps of data processing to the storage system. With the exception of the PXD, all sub-detectors are read out by the unified data link

## 4.2. Data Acquisition System

Table 4.1.: Total cross section and trigger rates for  $\mathcal{L} = 8 \cdot 10^{35} \text{ cm}^{-2}\text{s}^{-1}$  from various physics processes at the  $\Upsilon(4\text{S})$ .[27]

Physics process	Cross section (nb)	Rate (Hz)
$\Upsilon(4\text{S} \rightarrow B\bar{B})$	1.2	960
$e^+e^- \rightarrow \text{continuum}$	2.8	2200
$\mu^+\mu^-$	0.8	640
$\tau^+\tau^-$	0.8	640
Bhabha ( $\theta_{\text{lab}} \geq 17^\circ$ )	44	350 <sup>a</sup>
$\gamma\gamma$ ( $\theta_{\text{lab}} \geq 17^\circ$ )	2.4	19 <sup>a</sup>
$2\gamma$ processes ( $\theta_{\text{lab}} \geq 17^\circ, p_t \geq 0.1 \text{ GeV}/c$ )	$\sim 80$	$\sim 15000$
Total	$\sim 130$	$\sim 20000$

<sup>a</sup>The rate is pre-scaled by a factor of 1/100

system called the Belle2Link. The working principle of the DAQ can be seen in figure 4.2.

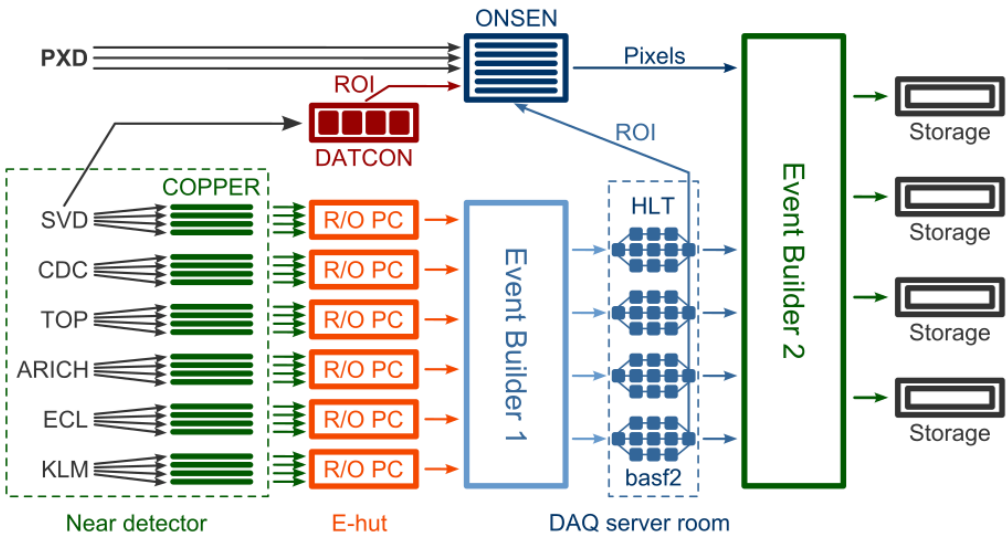


Figure 4.2.: Working principle of the Belle II DAQ. The data is transferred by about 300 COPPER boards to about 30 R/O PCs. The data is then put together by the first event builder and the events are reconstructed by the HLT afterwards. The HLT contains  $O(10)$  units with about 400 cores each. Then, the reconstructed data is merged with to data coming from the PXD. Finally, the data is saved on about 10 storage units. [28]

The first part of the Belle2Link is the common readout platform (COPPER). This platform transforms the different data formats coming from the sub-detectors into a

#### *4. Trigger And Data Acquisition System*

common data format. The COPPER boards then send their output signal to the event builder, which merges the data coming from the same collision to an event. With the information from the fully reconstructed events, the high level trigger (HLT) is able to finally decide whether the event should be stored or not. If the event should be recorded, it is then merged with the information coming from the PXD data in the second event builder.

Once the PXD receives the trigger signal, the readout starts. These data are stored on online selector nodes for up to 5 s. Meanwhile, the HLT performs the event reconstruction. Based on information coming from the SVD and CDC, the charged tracks, reconstructed in the HTL, are transferred back to the PXD and regions of interest (ROI) are formed. Only pixels of the PXD within the ROI are kept and considered in the second event builder. Complementarity to the HLT, the data concentrator also searches for RIOs. The HLT is optimized for high momentum and the data concentrator is optimized for low momentum particles. Both systems require hits in all SVD layers.

THIS chapter will give a short introduction on the two most important tools that were used in this thesis: Basf2 and GridKa.

## 5.1. Basf2

The software framework used at Belle2 is called BASF2 (Belle AnalysisS Framework). It is designed to prosecute off-line and analysis tasks. The majority of the code is written in C++, but python scripts are used for framework execution. The user specifies a sequence of modules in the python steering file which than process events. It also provides access to external libraries like ROOT which allows processing, statistical analysis, visualization and storage of common data and Geant4 for simulating the full detector.[29]

OffLineTracking

## 5.2. GridKa



## Preparation For Calculating The Tracking Efficiency Of Phase2

THIS chapter will provide an overview on how the cuts where chosen and which selection was applied in order to calculate a reasonable tracking efficiency on phase2 data. We will start with a definition of the tracking efficiency we want to calculate. Then the reconstruction and selection of the Bhabha events will be described. The same selection and cuts used on phase2 will also be used on phase3 later on.

### 6.1. Phase2

Phase2 data were taken in the time between March 2018 and July 2018. During this time, only a small azimuthal fraction of the vertex detector was installed. The main focus of this phase was to study the background of the newly installed BelleII detectors, in order to be certain that the operation of the vertex detector is compatible with the much higher luminosity expected for physics data taking. Also, hardware controls were tested in this phase.

### 6.2. Definition Of Tracking Efficiency

First of all, a definition of efficiency has to be declared, since there are different ways to define a tracking efficiency. The physics case we are considering is Bhabha events  $e^+e^- \rightarrow e^+e^-$ . As described in chapter 3, charged particles leave a track in the detector. So, when we look at an outgoing particle with a track, then we know that the other particle should also have a track. If the other particle has no track associated, then this is an inefficiency. If both particles have a track associated, then this is the efficient case.

So for this work, we will use the following definition for the tracking efficiency:

$$\epsilon = \frac{\text{Number of Bhabha events with exactly 2 reconstructed tracks}}{\text{Number of Bhabha events with 1 or more reconstructed tracks}} \quad (6.1)$$

To calculate an efficiency according to equation 6.1 one needs two histograms. One histogram filled particle information in the case that both particles are charged, and a

## 6. Preparation For Calculating The Tracking Efficiency Of Phase2

histogram filled with particle information in the case that at least one particle in the event is reconstructed as a charged particle. The first will be referred to as *enumerator* histograms and the later will be referred to as *denominator* histograms.

The particle we investigate will be called *probe*. The other particle will be called *tag*. We know that *tag* is always reconstructed as a charged particle. Therefore, we will calculate the efficiency for two different cases:

- Electron: *tag* is reconstructed as a positron
- Positron: *tag* is reconstructed as an electron

### 6.3. Reconstructing Bhabha Events With Basf2

To analyze a Monte Carlo/data file, a python script using Basf2 has to be written. The following code is a simplified version of the steering file I wrote. The whole steering file is located on KEK at:

```
/home/belle2/msobotzi/bhabha/bhabha_vpho.py
```

The goal of this steering file is to reconstruct the virtual photon in a Bhabha event. This virtual photon decays into two daughters which hit the ECL. Since we want to calculate the tracking efficiency, we need to be able to reconstruct the virtual photon from two daughters both associated with a track, and two daughters one associated with a track (reconstructed as a charged particle by the framework) and one with no track associated (reconstructed as a photon by the framework).

The same steering file is used for data, MC and MC on GridKa.

```
1 fillParticleList('gamma:all', 'clusterE > 0.01', path=mypath)
2 fillParticleList('e+:all', 'clusterE > 0.01', path=mypath)
3
4 reconstructDecay('vpho:gamma -> gamma:all', '', path=mypath)
5 reconstructDecay('vpho:elec -> e+:all', '', path=mypath)
6
7 copyLists(outputListName = 'vpho:ECLObjectUnranked', inputListNames=['vpho:
8     ↪ elec', 'vpho:gamma'], path=mypath)
9
10 rankByHighest('vpho:ECLObjectUnranked', 'daughter(0,clusterE)', path=mypath)
11 cutAndCopyList('vpho:ECLObject', 'vpho:ECLObjectUnranked', '', path=mypath)
12
13 reconstructDecay('vpho:bhabha -> vpho:ECLObject vpho:ECLObject', '',
14     ↪ mypath)
15
16 variablesToNtuple('vpho:bhabha', variables, treename = 'vpho_bhabha',
17     ↪ filename = output.root, path=mypath)
```

### 6.3. Reconstructing Bhabha Events With Basf2

In the first line of code all particles which hit the ECL and have no track associated are filled into a gamma list called `gamma:all`. The clusters created by those particles must have an energy (`clusterE`) of at least 0.01 GeV. In the second line a list called `e+:all` is created. All particles with an associated track are filled in this list independently of their charge. Therefore, this list contains for example electrons, positrons and even muons. Therefore, a cut is applied to the cluster energy and not on the energy of the particles.

Due to the fact, that we want to calculate the efficiency of the tracking, we need to somehow combine the `e+:all` and the `gamma:all` lists. As mentioned earlier, we need to be able to reconstruct the virtual photon from particles reconstructed as electrons/positrons and photons. Unfortunately, the Basf2 framework prevents a combination of two different particle lists, like `e+:all` and `gamma:all`. Therefore, we need to use a trick. This is shown in lines four and five. In line four, we tell the framework that the reconstructed gamma is the only daughter of a virtual photon called `vpho:gamma`. The same is done for the electron list. Here, the virtual photon is called `vpho:elec`.

Now, these two lists can be combined to one list called `vpho:ECLObjectUnranked`. This is done in line seven.

In line nine and ten the daughters in the `vpho:ECLObjectUnranked` list are sorted by their cluster energy and filled in a list called `vpho:ECLObject`.

In line twelve, a virtual photon of the bhabha event is reconstructed from the ECL objects in the `vpho:ECLObject` list. The number of reconstructed virtual photon candidates per event  $n_{\text{cand}}$  is determined by the following equation[30]:

$$n_{\text{cand}} = \frac{n_p(n_p + 1)}{2} \quad (6.2)$$

$n_p$  is the number of reconstructed particles per event. Equation 6.2 is also known as the equation to calculate *triangular numbers*. For example, if four ECL particles are reconstructed in a single event then ten virtual photon candidates are reconstructed according to equation 6.2. Since we only expect one virtual Bhabha photon per event, we have to select the best candidate in each event. This will be done in section 6.4.

Since the entries in the `vpho:ECLObject` list are sorted by energy, the first daughter of the reconstructed virtual bhabha photon always has a higher energy than the second daughter. I will refer to the first daughter as `Hc1E` and the second daughter as `Lc1E`. You can see that the `Hc1E` daughter has always a higher energy than the `Lc1E` daughter in figure A.1. Here the `clusterE(Lc1E)` is subtracted from the `clusterE(Hc1E)` and only positive values remain. Therefore, `Hc1E` is the daughter with the higher energy.

Finally, in the last line of code, all variables of the candidates like mass, momentum, cluster energy of each daughter, does the daughter have a track and so on are written in a tree `vpho_bhabha` in a file. The `outputname` of the output file depends on whether the steering file is running on data or MC.

## 6. Preparation For Calculating The Tracking Efficiency Of Phase2

### 6.4. Best Candidate Selection On Phase2 Monte Carlo

We use Monte Carlo simulation due to the fact that on MC we know everything about the generated and reconstructed particles. So on MC we can select Bhabha events which hit the ECL and with this knowledge we can introduce cuts in such a way that we only reconstruct these Bhabha events. To calculate an efficiency it is extremely important to select only Bhabha events. At first, we are also running on only one  $e^+e^- \rightarrow e^+e^-$  MC file which is located at:

```
/belle/MC/release-01-00-02/DB00000294/MC10/prod00004668/s00/e1002/4S/  
r00000/3600520000/mdst/sub00/mdst_000050_prod00004668_task10010000050.root
```

The generated file is located at:

```
/home/belle2/msobotzi/bhabha/bhabha_vpho_mc.root
```

#### 6.4.1. ECL-Cut

Due to the fact that we can verify a Bhabha event with only ECL informations and we are therefore only interested in events which hit the ECL, we apply a  $\theta$ -cut on the generated daughters (generated daughters means the true generated Monte Carlo daughters).

$$0.296706 < \theta_{HclE,LclE} < 2.617990 \quad (6.3)$$

All the events which survive this cut are written into a list (*mcEvtECL*). We know that the file Monte Carlo file contains 140000 generated Bhabha events. After this cut, only 24286 Bhabha events remain. In section 2.3.1, we saw that Bhabha events have a very high cross-section in forward and backward direction. So, we expect that most of the generated daughters are not hitting the ECL.

Now we will take a look at the reconstructed Monte Carlo events. All of these reconstructed events have to appear in the *mcEvtECL* list because we know that only in these events both daughters are hitting the ECL. A total of 24100 events have at least one reconstructed candidate.

In figure 6.1 on the left, we see the number of reconstructed candidates per event. Since we do not have a cut on the reconstruction, the number of reconstructed candidates  $n_{cand}$  follows equation 6.2. On the right, we see the invariant mass of the reconstructed candidates. Note that we are now looking at candidates and as we can see on the left we oftentimes have more than one candidate per event. Therefore, the numbers of entries for the mass is way higher then for the number of candidates per event. Consequently, we need some cuts to select the best candidate in each event and thereby reduce the number of candidates per event to one.

#### 6.4. Best Candidate Selection On Phase2 Monte Carlo

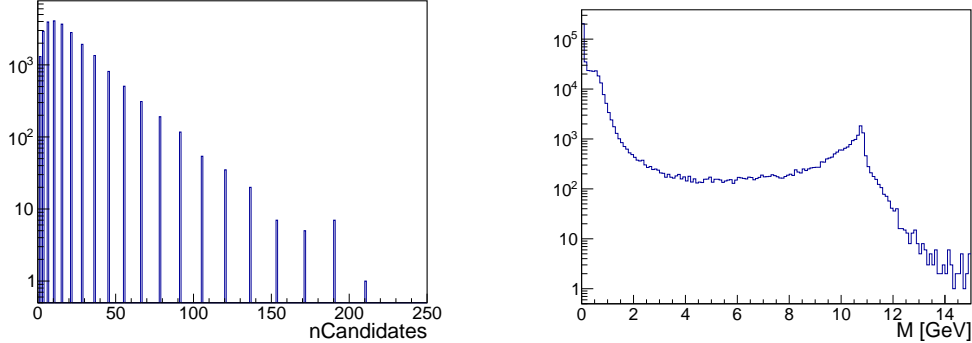


Figure 6.1.: Left: The number of reconstructed candidates per event is shown. We select 24100 events. Right: The invariant mass of the reconstructed candidates is shown. We select 417899 candidates.

##### 6.4.2. Mass-Cut

The first cut to reduce the number of reconstructed candidates per event is a mass cut (The cut is called  $M$ ). As we saw in figure 6.1, a lot of candidates are reconstructed with an low invariant mass and we know from section 2.3.1 that the mass of the reconstructed candidate should be the invariant mass of the collider. For Belle II this is around 10.58 GeV. Due to some acceptance for reconstruction error the mass cut is with an lower-cut of 8 GeV rather loose.

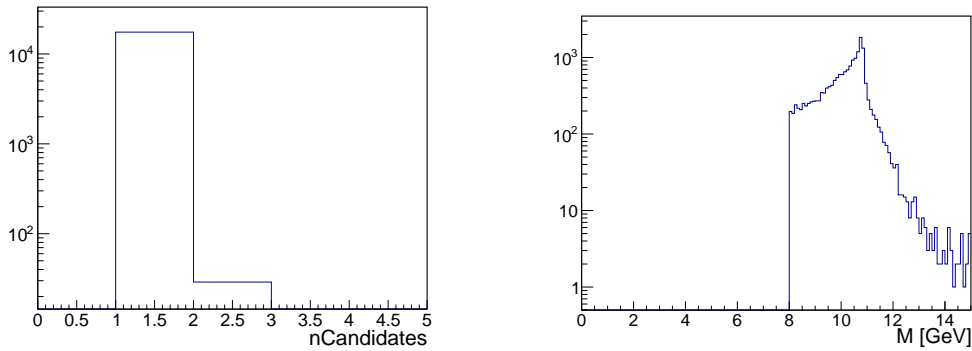


Figure 6.2.: A cut on the invariant mass is applied. The reconstructed invariant mass has to be bigger than 8 GeV. Left: The number of reconstructed candidates per event is shown. We select 17539 events. Right: The invariant mass of the reconstructed candidates is shown. We select 17558 candidates.

As you can see in figure 6.2 on the right, all reconstructed candidates with an invariant mass below 8 GeV are neglected. Therefore the number of candidates per event is reduced. We see this in the left plot. Unfortunately, sometimes we still have two

## 6. Preparation For Calculating The Tracking Efficiency Of Phase2

candidates per event and consequently, we have to introduce some more additional cuts.

### 6.4.3. Additional Cuts

To reduce the number of candidates per event to one, some additional cuts are needed. Sometimes it can happen that two reconstructed particles are associated to one Monte Carlo particle. Some examples of this effect can be seen in table 6.1.

Table 6.1.: Some examples for events with cluster splitting. mcE is the same for LclE and HclE. The energies are in GeV.

Event Number	HclE				LclE			
	E	mcE	PDG	mcPDG	E	mcE	PDG	mcPDG
41890065	0.9432	4.1278	11	11	3.1900	4.1278	22	-11
41890118	1.5993	4.3465	22	11	2.6462	4.3465	-11	-11
41890668	3.1758	6.8878	22	-11	3.1059	6.8878	11	11
41891214	2.3290	6.1585	22	-11	3.9079	6.1585	11	11
41892596	1.4193	4.2997	22	11	2.9673	4.2997	-11	-11

As you can see, the Monte Carlo generated energy (mcE) for both HclE and LclE is the same and the reconstructed energy (E) of the HclE and the LclE particle sum up roughly to their respectively mcE. You can also see that the generated particle is always a electron/positron and that the *additionally* reconstructed particle is always a photon.

In figure A.2 you can see the angular distribution of this effect. For this plot there were no cuts on the reconstruction. It was just checked if exactly two reconstructed particles have the same generated Monte Carlo particle associated. Then the clusterPhi- and clusterTheta-values of these particles were filled into their histograms. On the left you can see that the both reconstructed particle have the same clusterTheta angle. On the right you can see that they have a slightly different clusterPhi angle. Therefore, the one *original* cluster is separated into two clusters with the same  $\theta$ -angle and a different  $\Phi$ -angle. One cluster is associated with a track produced by the generated particle and for the other cluster is no track left, therefore, it is labeled as a photon. This effect will be referred to as *cluster splitting*.

In figure 6.3 you can see the energy of the particles in a cluster splitting process. Since we only want to select Bhabha events, we want to neglect these kinds of events. In section 2.3.3 we saw that the particles have an energy of at least 4 GeV. Therefore we are able to apply a cut on the cluster energy. We are now requiring a cluster energy of at least 3.5 GeV (The cut is called **Mc1E**). With this cut almost all events with cluster splitting should be neglected.

Next, we require that we have exactly two clusters per event, each with an energy of at least 3.5 GeV, since we only expect two high energetic particles in the ECL. Also, due to the kinematics at BelleII, we can require that one of the outgoing particles

#### 6.4. Best Candidate Selection On Phase2 Monte Carlo

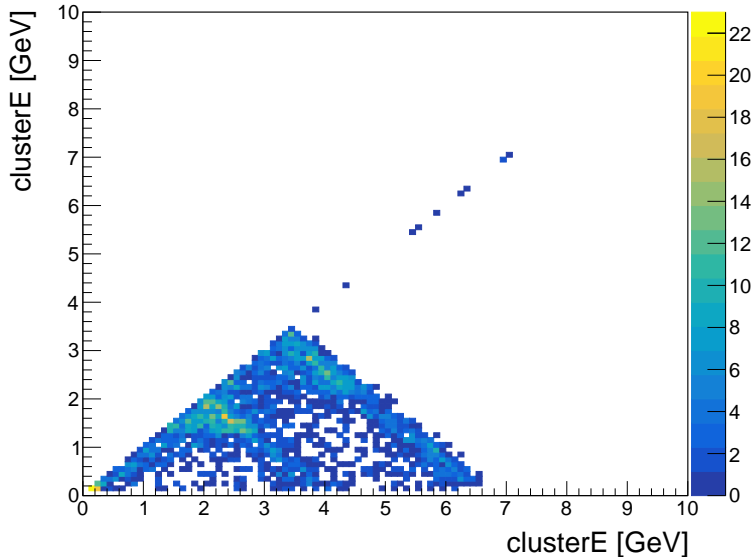


Figure 6.3.: Cluster Energy vs. Cluster Energy in the case that both particles are associated to the same Monte Carlo particle. Here, no cuts are applied. The total number of entries is 2891.

have an cluster energy of at least 4.5 GeV. This is required due to the trigger we will add in section 6.7. (the cut is called **Mc1E2H**).

As an additional safety net, a cut on the number of reconstructed tracks per event is applied. On data it can happen that there are way more than two tracks reconstructed per event. To select only *clean* events we apply a cut on the number of reconstructed charged particles per event (The cut is called **Mc1E2HnT**). This number should not be greater than six.

Table 6.2.: Some examples for events with too much energy in the ECL.

Note: Here the energy of the particles is shown not clusterE.

Event Number	M	Energy(Hc1E)	Energy(Lc1E)	Total Energy ECL
41890917	30.6657	33.8368	7.2455	41.0823
26574414	108.4056	235.3918	13.0644	248.4563
21222871	11.6553	2.1733	15.6648	17.8381
26372406	10.3229	0.2465	190.2663	194.5971

As you can see in table 6.2, sometimes the invariant mass of the reconstructed candidates is way bigger than 10.58 GeV. To neglect these candidates an upper cut on the reconstructed invariant mass is introduced. Now, the reconstructed invariant mass also has to be smaller than 12 GeV.

## 6. Preparation For Calculating The Tracking Efficiency Of Phase2

Also, sometimes the total energy in the ECL is way higher than expected. To exclude these events an upper cut on the total energy per event in the ECL is added (The cut is called `Mc1E2HnTSumE`). The total energy in the ECL must not exceed 15 GeV.

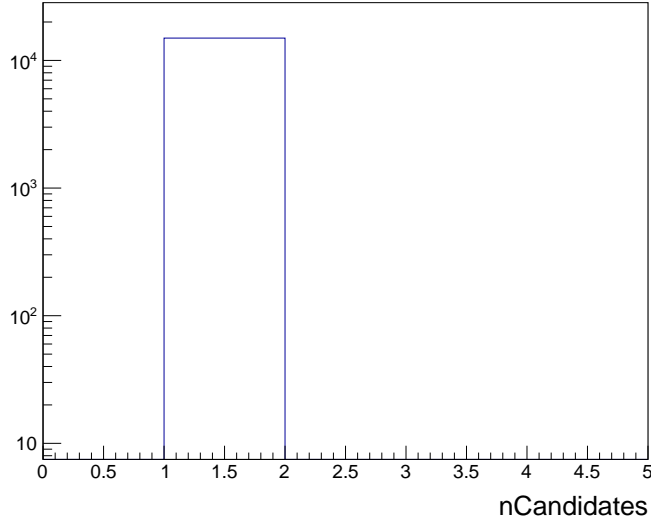


Figure 6.4.: Number of candidates per event after applying all cuts.  $n = 14545$

After applying all mentioned cuts, the number of candidates per event is shown in figure 6.4. As you can see, now, we only select one candidate per event. Therefore, we select 14545 events and candidates.

There is no cut on the interaction point since this would require a backtracking of the particles.

### 6.4.4. Cut Efficiency

In this section we want to discuss different efficiencies of the previously introduced cuts. We will take a look at the relative and the total efficiency. The results can be seen in table 6.3.

$$\epsilon_{\text{tot}} = \frac{n_{\text{cut}}}{n_{\text{total}}} \quad (6.4)$$

To calculate the total efficiency of a cut we have to use equation 6.4. Here the number of events after a cut  $n_{\text{cut}}$  is divided by the total number of events  $n_{\text{total}}$  before all cuts<sup>1</sup>.

$$\epsilon_{\text{rel; Cut B}} = \frac{n_{\text{Cut B}}}{n_{\text{Cut A}}} \quad (6.5)$$

---

<sup>1</sup>The cut that requires that the generated particles have to hit the ECL is still applied  $\rightarrow n_{\text{total}} = 24100$

## 6.5. Best Candidate Selection on Phase2 Data

Equation 6.5 shows the equation used to calculate the relative efficiency. To calculate the efficiency of cut B we have to divide the number of events after cut B by the number of events after the previous cut A. The relative efficiency with no cut is defined as 1.

Table 6.3.: A table with the total number of events after the respective cuts. Also the relative and the total efficiency of these cuts is shown. The total number of entries in the *mcEvtECL*-list is 24286.

Cut	Number Of Events	Relative Efficiency	Total Efficiency
No Cut	24100	1.0000	1.0000
M	17529	0.7273	0.7273
Mc1E	14903	0.8502	0.6183
Mc1E2H	14896	0.9995	0.6180
Mc1E2HnT	14896	1.0000	0.6180
Mc1E2HnTSumE	14545	0.9764	0.6035

Table 6.3 shows the relative and total efficiency of the cuts. As you can see, after all cuts a total of about 62% generated Bhabha events are reconstructed.

### 6.4.5. No MC-Truth Information

In the previous sections we saw that we are able to select only one candidate in a Bhabha event under the condition that we know that both daughters are hitting the ECL. Unfortunately we do not have this information on phase2 data. Therefore, we also check how many candidates we reconstruct when we do not have MC-Truth information. We will analyze the same MC-file as before to compare the number of reconstructed events.

In figure 6.5 we see that we reconstruct a total number of 14581 events. Therefore, we reconstruct only 36 events more with no MC-Truth information. Also, we are still able to select only one candidate per event.

Since we only reconstruct a few more events and still only one candidate per event, we can be very confident that we only select Bhabha events.

## 6.5. Best Candidate Selection on Phase2 Data

Until now we only run on MC but ultimately we want to calculate the tracking efficiency on Beamtime-data. Therefore, we have to test the selection also on Beamtime-Data. I used the same steering file as described in section 6.3 and run over the following files located at:

```
/ghi/fs01/belle2/bdata//Data/release-03-00-03/DB00000528/proc00000008/e0003/
4S/r02608/all/mdst/sub00/*.root
```

The generated file is located at:

## 6. Preparation For Calculating The Tracking Efficiency Of Phase2

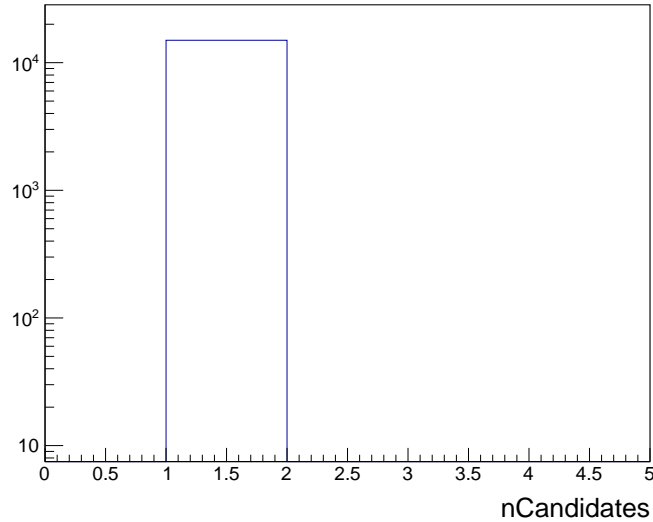


Figure 6.5.: Number of candidates per events with no MC-Truth information and all cuts. Same MC file as before. We also select just one candidate per event. The total number of selected events is 14581.

/home/belle2/msobotzi/bhabha/bhabha\_vpho\_data\_608.root

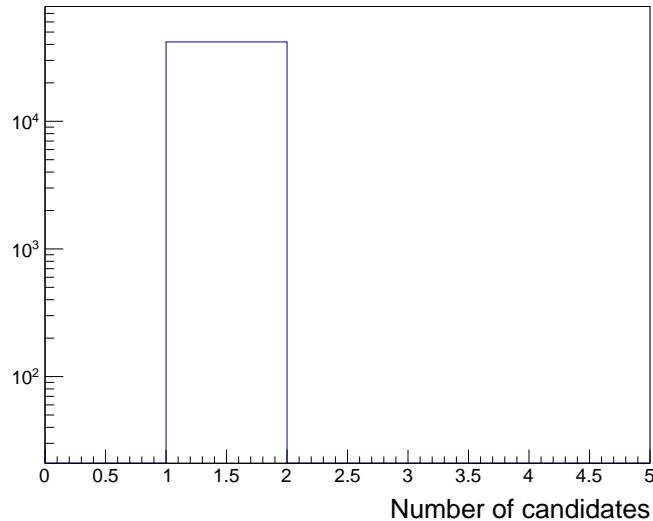


Figure 6.6.: Number of candidates per event for Beamtime-Data. We also select only one candidate per event on Beamtime-Data. A total number of 41853 events and candidates is selected.

## 6.6. Selecting Bhabha Events

Figure 6.6 shows the number of reconstructed candidates on phase2 data after the `Mc1E2HnTSumE` cut. You can see that we reconstruct only one candidate per event even on phase2 data.

### 6.6. Selecting Bhabha Events

Now, that we are satisfied with the selection of events and candidates we need to be sure that we only select  $ee \rightarrow ee$  events and not for example  $ee \rightarrow \gamma\gamma$ . To do this we can use the so-called b2b-variable (back-to-back).

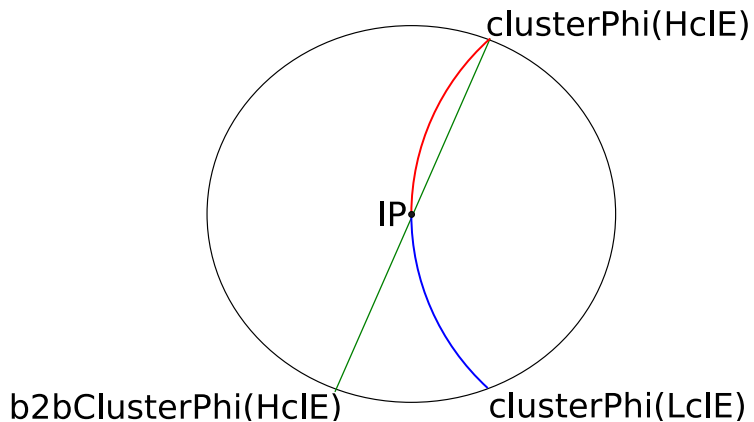


Figure 6.7.: Simplified representation of the `b2bClusterPhi` variable. The track of charged particles are bend in the detector. This sketch was created with Inkscape.

A simplified sketch of the `b2bClusterPhi` variable is shown in figure 6.7. This sketch shows the ECL in beam direction, so the magnetic field in the ECL is pointing into the paper. At the interaction point an electron (in this example the red line) and a positron (in this example the blue line) are created. Since both particles are charge their trajectory is bended by the magnetic field. The electron hits the ECL and creates a cluster with at the  $\Phi$ -angle `clusterPhi`. As described in section 2.3.3 the center-of-momentum frame at Belle II has a non zero  $x - y$  fraction. Therefore, the `b2bClusterPhi` variable is not just `clusterPhi`  $- \pi$  (as in the sketch). To calculate the `b2bClusterPhi` variable we have to boost the particle in the center-of-momentum frame then calculate `clusterPhi`  $- \pi$  and finally boost back in the lab frame. With this variable we can kind of predict the `clusterPhi` angle of the other particle.

In the sketch you see that there is a difference between the predicted and the true `clusterPhi` angle due to the magnetic field. This also means that in an  $ee \rightarrow \gamma\gamma$  event the predicted and the true `clusterPhi` angle are the same because the trajectory of photons are not bend in the magnetic field. Therefore, we are able to differ between  $ee \rightarrow ee$  and  $ee \rightarrow \gamma\gamma$ .

## 6. Preparation For Calculating The Tracking Efficiency Of Phase2

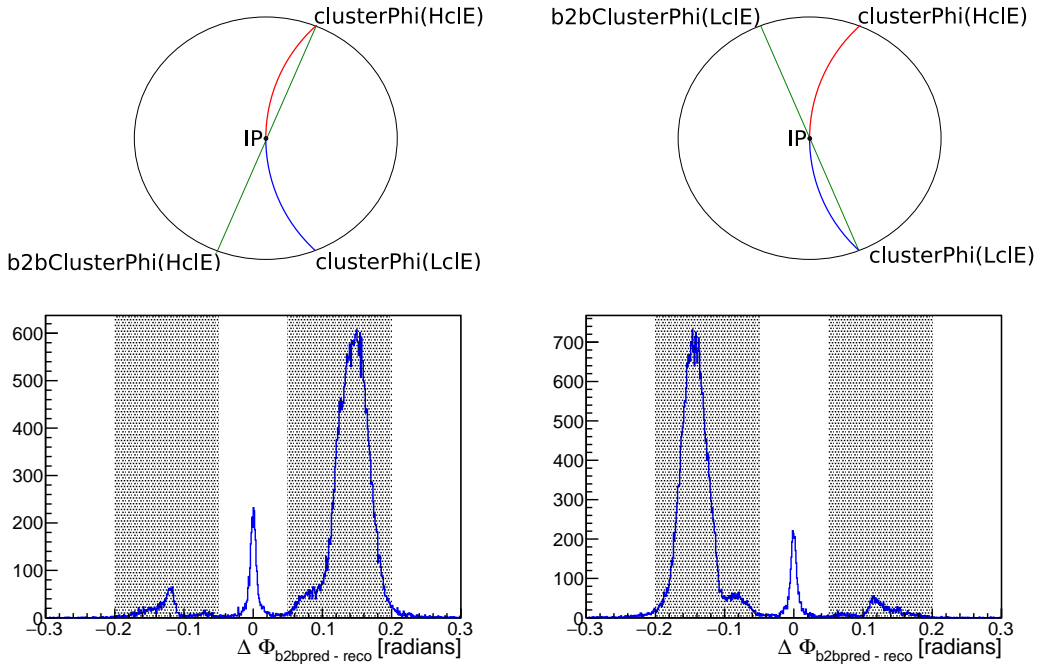


Figure 6.8.: Left: Predicted clusterPhi(HcIE) - Reconstructed clusterPhi(LcIE). Right: Predicted clusterPhi(LcIE) - Reconstructed clusterPhi(HcIE). Only particles within the gray area are taken into account. Both plots are created with phase2 data. The variable to get the predicted clusterPhi value is the b2bclusterPhi variable which was described earlier. The two top sketches represent what is calculated.

In figure 6.8 the difference between the predicted and the reconstructed clusterPhi angle for Beamtime-Data is shown. In the left plot the reconstructed clusterPhi angle of the LcIE particle is subtracted by the b2bClusterPhi angle of the HcIE particle. In the right plot it is vice versa. In both plots we have three peaks. The middle peaks are  $ee \rightarrow \gamma\gamma$  events since the predicted and the reconstructed clusterPhi angle is the same. So these are events we want to cut away. The left peak is caused by electrons (most of the HcIE particles are electrons, therefore the left peak on the right plot is significantly higher<sup>2</sup>), the right peak by positrons. This means that if for example we only cut on the left peak we are only selecting electron particles even if they are wrongly reconstructed as photons, using ECL information only. Therefore, the last cut we will add is a cut on the b2bClusterPhi angle. We will only consider events in with:

---

<sup>2</sup>As described in section 6.3, the HcIE daughter is the daughter with the higher cluster energy

## 6.6. Selecting Bhabha Events

$$0.05 \leq \text{abs}(\text{b2bClusterPhi(HclE)} - \text{clusterPhi(LclE)}) \leq 0.2 \quad \text{and} \quad 0.05 \leq \text{abs}(\text{b2bClusterPhi(LclE)} - \text{clusterPhi(HclE)}) \leq 0.2$$

A special case occurs for  $\Phi \approx \pi$  or  $\Phi \approx -\pi$ . It can happen that the reconstructed clusterPhi angle is around  $\pi$  but the b2bClusterPhi angle is calculated to be around  $-\pi$ , then the difference between the predicted and reconstructed clusterPhi angle is around  $2\pi$ . This can be seen in figure A.3

Finally, the b2bClusterPhi variable cut can be summarized in the following three conditions. Each event has to fulfill one of them to be taken into account.

- (a)  $0.05 \leq \text{abs}(\text{b2bClusterPhi(HclE)} - \text{clusterPhi(LclE)}) \leq 0.2 \&\& 0.05 \leq \text{abs}(\text{b2bClusterPhi(LclE)} - \text{clusterPhi(HclE)}) \leq 0.2$
- (b)  $2\pi - 0.2 \leq \text{abs}(\text{b2bClusterPhi(HclE)} - \text{clusterPhi(LclE)}) \leq 2\pi - 0.05 \&\& 0.05 \leq \text{abs}(\text{b2bClusterPhi(LclE)} - \text{clusterPhi(HclE)}) \leq 0.2$
- (c)  $0.05 \leq \text{abs}(\text{b2bClusterPhi(HclE)} - \text{clusterPhi(LclE)}) \leq 0.2 \&\& 2\pi - 0.2 \leq \text{abs}(\text{b2bClusterPhi(LclE)} - \text{clusterPhi(HclE)}) \leq 2\pi - 0.05$

These cuts are visualized by the gray area in figure 6.8. Only particles within these areas are taken into account.

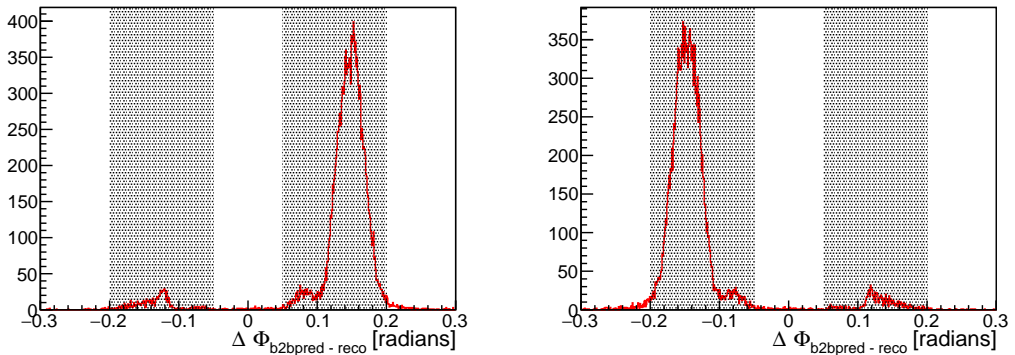


Figure 6.9.: Left: Predicted clusterPhi(HclE) - Reconstructed clusterPhi(LclE). Right: Predicted clusterPhi(LclE) - Reconstructed clusterPhi(HclE). Only particles within the gray area are taken into account. Both plots are created with MC data. There is no middle peak because only ee  $\rightarrow$  ee events were generated.

Figure 6.9 shows the same plots as figure 6.8 but with MC data. Note that there is no middle peak because only ee  $\rightarrow$  ee events were generated. In figure A.4 the b2bClusterPhi plot with full range is shown for MC.

## 6. Preparation For Calculating The Tracking Efficiency Of Phase2

### 6.7. ECL-Trigger

Last but not least, we need to be sure that each event has a trigger signal coming from the ECL. Otherwise, the trigger signal could come only from the tracking detectors. Then, there would be a bias on the efficiency, since the tracking detectors require at least one track. Therefore, a cut on the trigger called `bhabha` is introduced. `bhabha`. This trigger requires a signal coming from the ECL and some additional conditions. Both reconstructed particles have to have an energy of at least 3 GeV each and one of them has to have at an energy of 4.5 GeV or more.

[31] [cut von bhabha aendern](#)

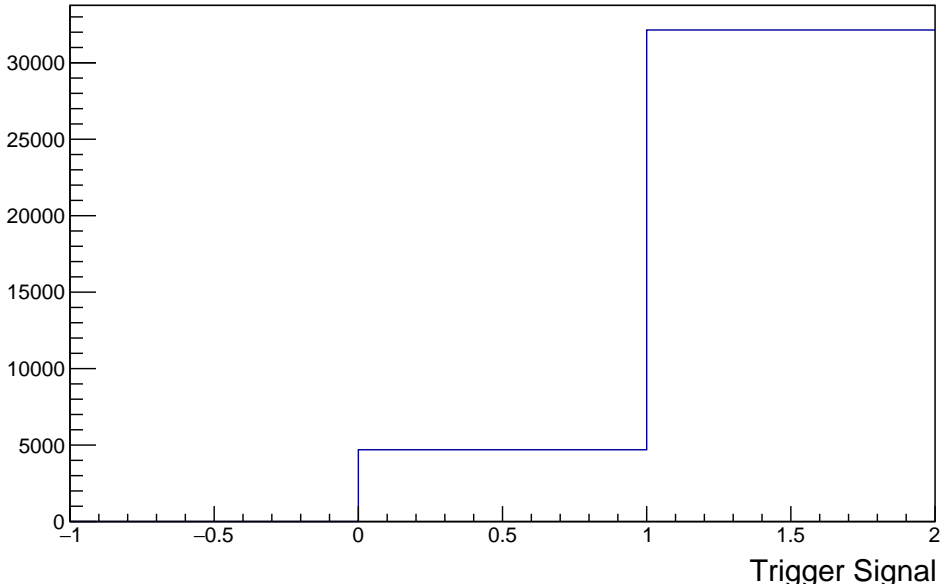


Figure 6.10.: `bhabha` trigger signal for a single data file after the selection.

Trigger Signal == 0 means that there was no trigger signal in the event.

Trigger Signal == 1 means that there was a trigger signal in the event.

(Trigger Signal == -1 means that there are no trigger informations in the file.) As you can see, in most of the selected events there is a trigger signal coming from the ECL.

In figure 6.10 you can see the `bhabha` trigger signal for a single phase2 data file after the selection. Most of the time, there was an ECL trigger signal and in only about 8 % of the events there was no trigger signal coming from the ECL. These events have to be cut out.

This is not done for Monte Carlo, since the trigger does not work reliable on MC and we only look at events we want to consider. Therefore, a trigger cut is only done for phase2 data (and phase3 data in chapter 8). This is also the reason why the cuts on

## 6.8. More Events

the cluster energy were chosen as they are. Otherwise, a comparison between phase2 MC and phase2 data would be impossible.

### 6.8. More Events

The efficiency errors are calculated with the following equation:

$$\Delta\epsilon = \sqrt{\frac{\epsilon(1 - \epsilon)}{n}} \quad (6.6)$$

In equation 6.6,  $\epsilon$  is the calculated efficiency and  $n$  is the total number reconstructed particles with and without an associated track in the investigated bin. This equation is only true for large  $n$ , since according this equation, an efficiency of 1 has always an error of zero. Therefore, the efficiency will be calculated by the root class TEfficiency. This class is able to calculate the right efficiency error even for small  $n$ . [32] To reduce the error on the calculated efficiency,  $n$  has to be as big as possible. Therefore, more phase2 data and phase2 MC files are needed. For Monte Carlo we will consider all files located at:

```
/belle/MC/release-01-00-02/DB00000294/MC10/prod00004668/s00/e1002/4S/
r00000/3600520000/mdst/sub00
```

Also, we will take all available phase2 data files into account. They are located on KEK at:

```
/ghi/fs01/belle2/bdata//Data/release-03-00-03/DB00000528/proc00000008/e0003/
4S/r0*/all/mdst/sub00/*.root
```

In figure 6.11, you can see the number of candidates per event after the selection. You can see that we reconstruct only one virtual photon per event on both phase2 data and MC.

### 6.9. Dividing The ECL In Areas Of Interest

As described in section 3.7, the ECL is divided in three areas. The barrel, the forward end cap and the backward end cap. Therefore, we will take a look at the efficiency of these areas separately. The first will only contain the forward end cap. This means, only particles with a predicted theta angle of  $0^\circ < \theta < 32^\circ$  will be taken into account. The second area of interest is the barrel. Here the predicted  $\theta$  angle of the investigated particle has to be  $32^\circ < \theta < 130^\circ$ . The last area of interest is the backward end cap with an cluster  $\theta$  angle of  $130^\circ < \theta < 180^\circ$ .

In section 2.3.3, we saw that the azimuth angle and the momentum of the particles are correlated in the lab frame. Therefore, we need to look at momentum intervals. Otherwise, it would be impossible to interpret the calculated efficiencies. For example,

## 6. Preparation For Calculating The Tracking Efficiency Of Phase2

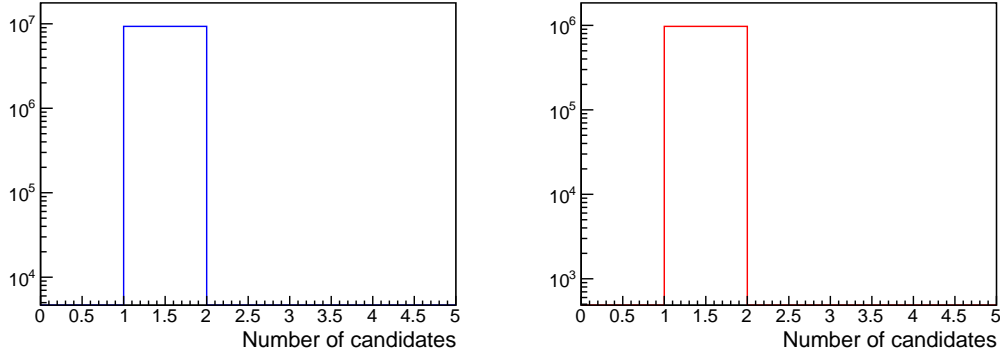


Figure 6.11.: The number of candidates per event after the selection is shown. Left: Phase2 Data. Right: Phase2 MC. A total of 9323903 candidates are selected for phase2 data and 973181 candidates are selected for phase2 MC.

a low efficiency in  $\phi$  could be the results of an inefficient forward end cap or created by momentum dependencies.

In figure 6.12 you can see the denominator histograms for the electron. In these plots, their predicted  $\theta$  and  $\phi$  angles for different momenta for Phase2 MC are shown. Also, the three areas of interest are indicated in these plots by a pink line. Phase2 MC was used to determine the momenta ranges because the statistics are lower on phase2 MC compared to phase2 data.

Figure A.5 shows the same plots but for phase2 data. Small differences for momenta between 4 GeV and more at an  $\phi$  angle of about  $0^\circ$  are caused by the geometry of the vertex detector. As already mentioned in section 6.1, only a small azimuthal fraction at  $\phi = 0$  was installed but not simulated properly on Monte Carlo. The corresponding phase2 data plots for positrons are shown in figure A.8.

In these four figures one can also see that it makes sense to look only at some momenta for different areas of interest. The different momenta regions are listed in table 6.4.

Table 6.4.: Momenta ranges for different *probe* cases and different areas of interest.

	$e^-$	$e^+$
Forward End Cap	4 GeV – 8 GeV	/
Barrel	4 GeV – 7 GeV	3 GeV – 7 GeV
Backward End Cap	/	2 GeV – 6 GeV

The same is done for the transverse momenta for the three different cases. The denominator plots of phase2 MC for the electrons can be seen in figure 6.14. Figure 6.15 shows the denominator plots for phase2 MC positrons. The different transverse momenta regions are listed in table 6.5.

### 6.9. Dividing The ECL In Areas Of Interest

Table 6.5.: Transverse Momenta ranges for different *probe* cases and different areas of interest.

	$e^-$	$e^+$
Forward End Cap	1 GeV – 4 GeV	/
Barrel	2 GeV – 6 GeV	3 GeV – 6 GeV
Backward End Cap	/	1 GeV – 4 GeV

We will also look at the tracking efficiency as a function of  $\theta$ . For this, we also have to choose momenta regions. They can be determined by the same plots as before. The selected ranges can be found in the following table.

Table 6.6.: Momenta and transverse Momenta Ranges for the tracking efficiency as a function of  $\theta$ .

	$e^-$	$e^+$
Momentum	4 GeV – 9 GeV	2 GeV – 7 GeV
Transverse Momentum	1 GeV – 6 GeV	1 GeV – 6 GeV

## 6. Preparation For Calculating The Tracking Efficiency Of Phase2

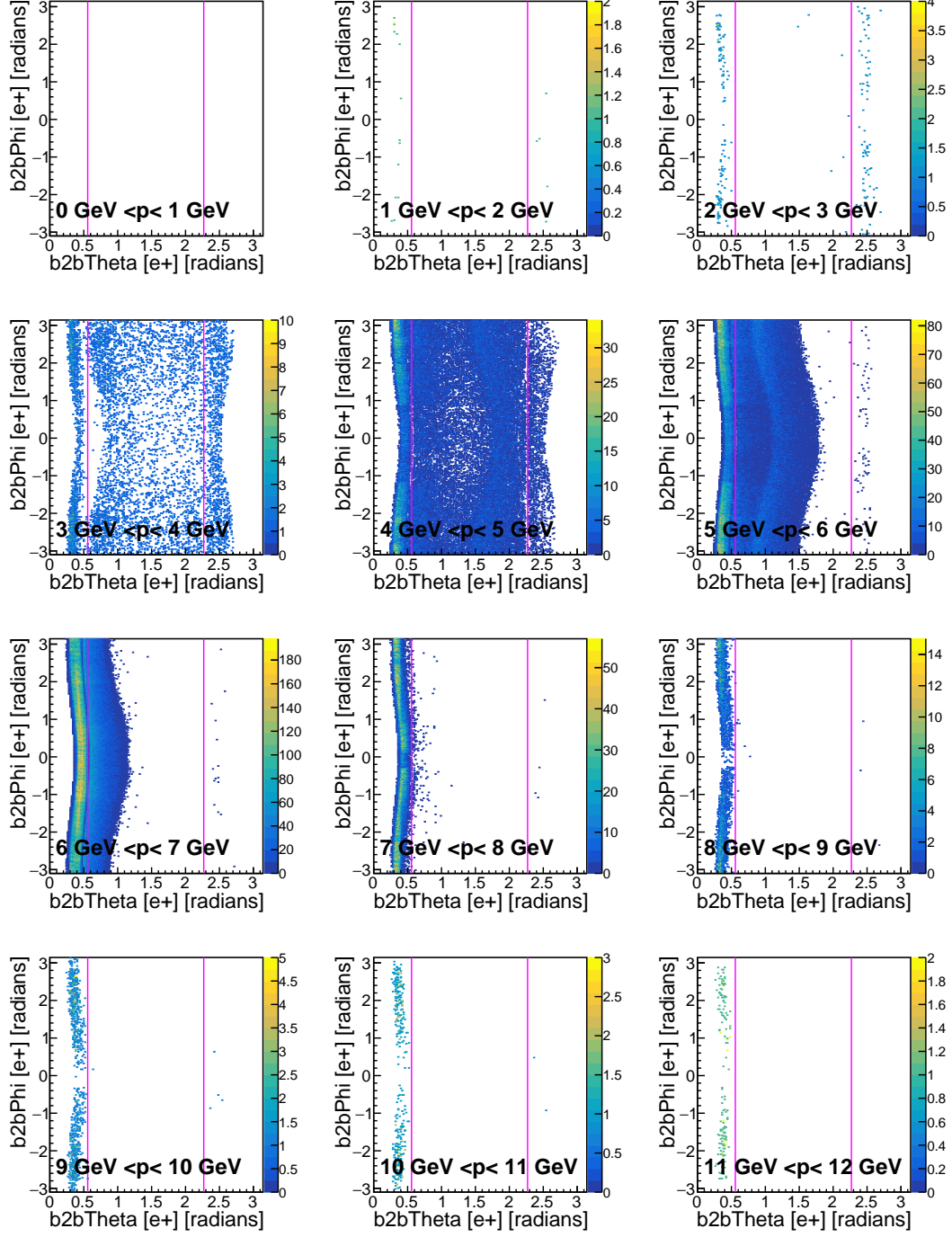


Figure 6.12.: Predicted  $\theta$  and  $\phi$  denominator histograms of the electron for different momenta for phase2 MC are shown. The different areas of interest are indicated by the pink line.

## 6.9. Dividing The ECL In Areas Of Interest

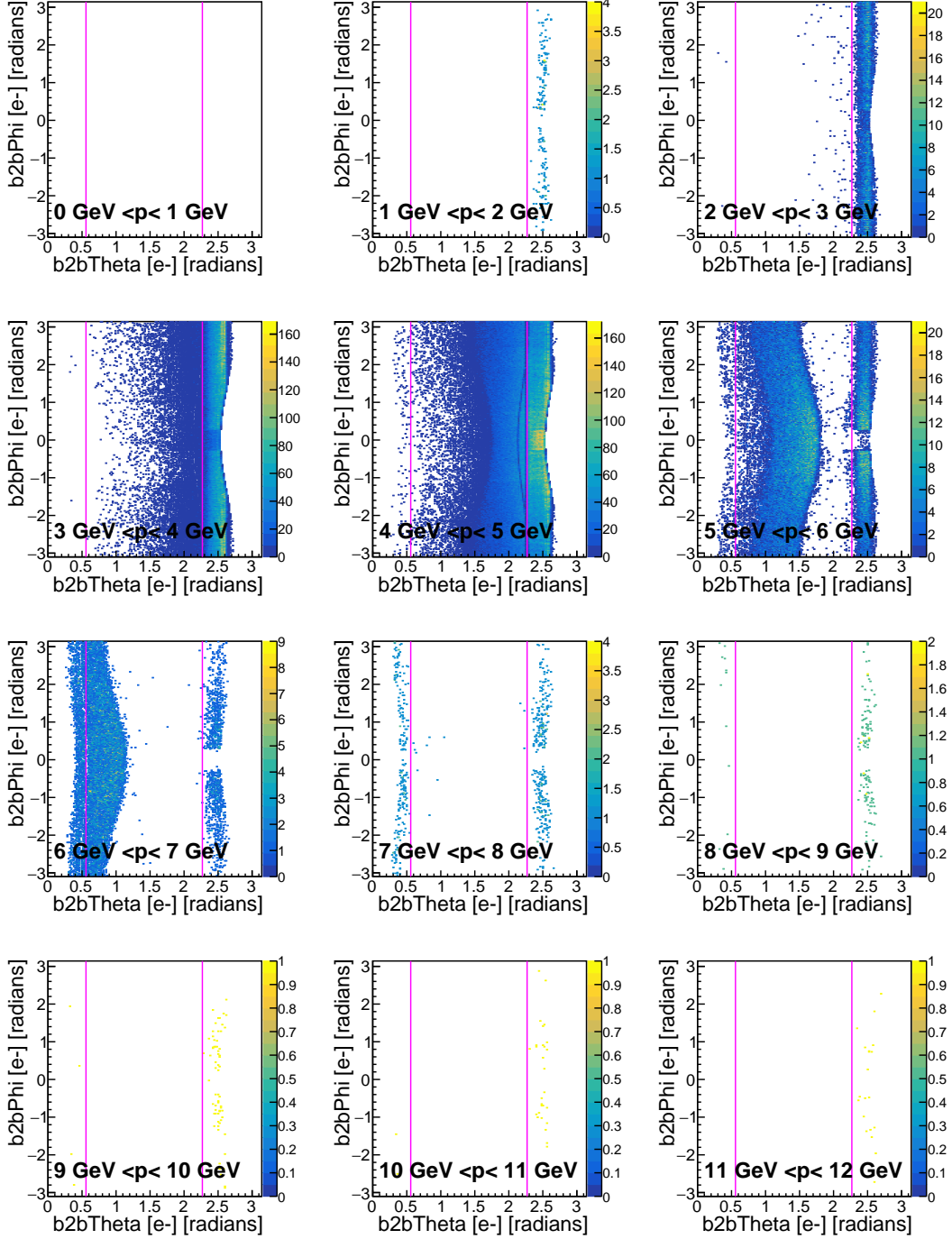


Figure 6.13.: Predicted  $\theta$  and  $\phi$  denominator histograms of the positron for different momenta phase2 data are shown. The different areas of interest are indicated by the pink line.

## 6. Preparation For Calculating The Tracking Efficiency Of Phase2

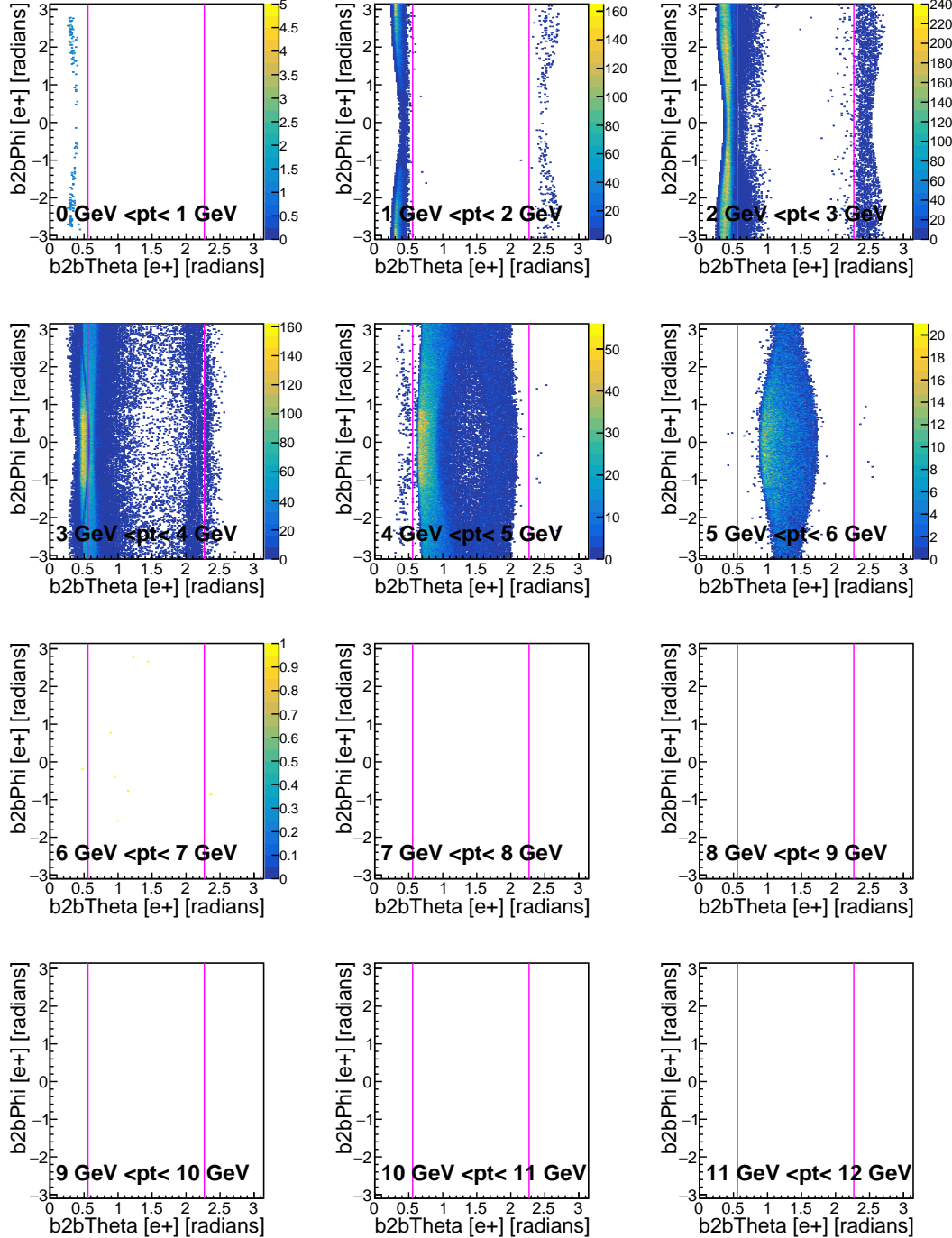


Figure 6.14.: Predicted  $\theta$  and  $\phi$  denominator histograms of the electron for different transverse momenta for phase2 MC are shown. The different areas of interest are indicated by the pink line.

### 6.9. Dividing The ECL In Areas Of Interest

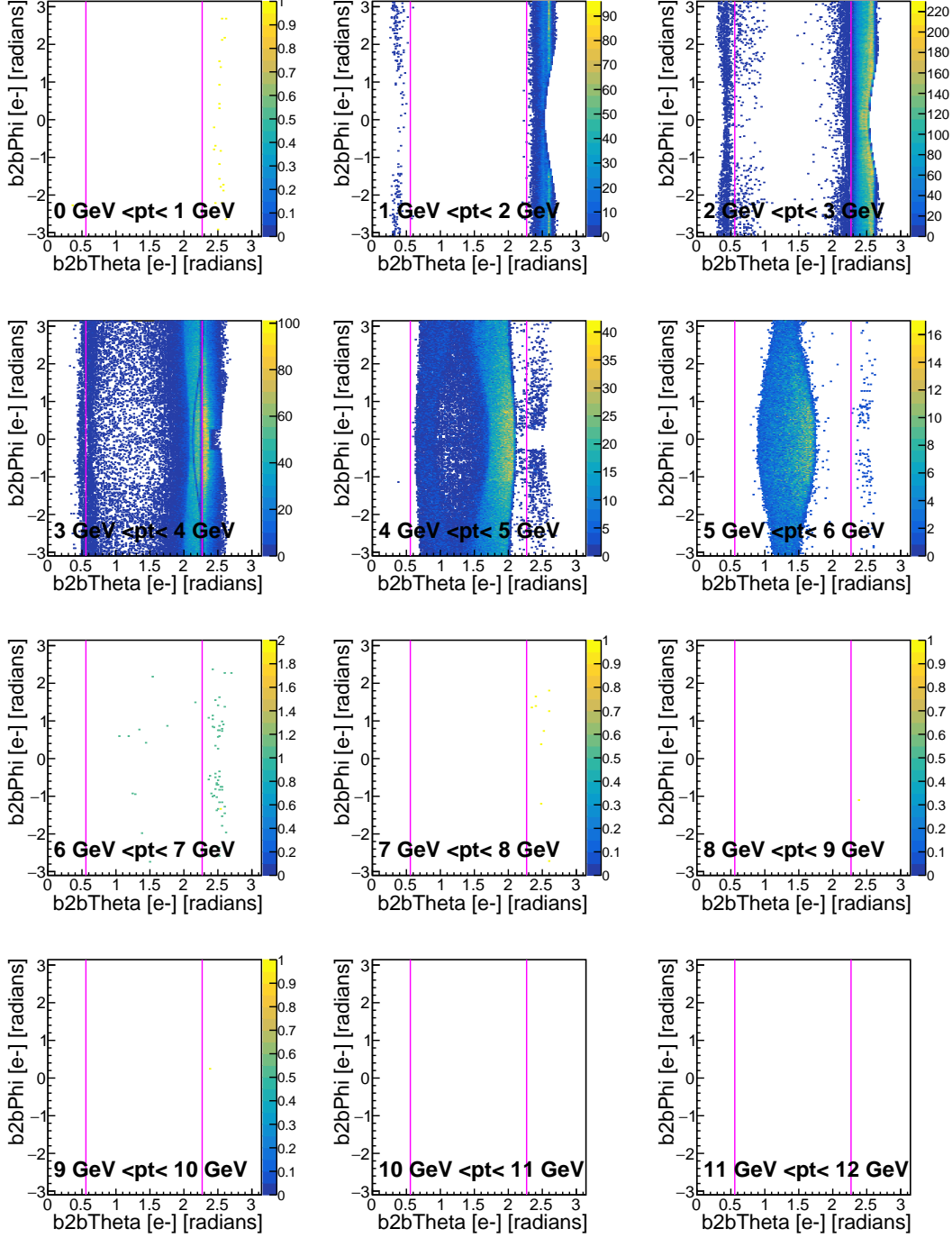


Figure 6.15.: Predicted  $\theta$  and  $\phi$  denominator histograms of the positron for different transverse momenta for phase2 data are shown. The different areas of interest are indicated by the pink line.



In this chapter the tracking efficiency studies on phase2 will be presented. The selection described in chapter 6 will be used in this chapter. Phase2 data in blue and phase2 Monte Carlo in red will be shown together, in order to make comparison between these two easier. The individual tracking efficiencies can be found in the appendix.

## 7.1. Momentum Efficiencies

### 7.1.1. Forward End Cap

In figure 7.1 you can see the calculated electron tracking efficiency for different momenta. As expected, the tracking efficiency for phase2 data is almost all of the time worse than the efficiency for phase2 MC for all momenta. For momenta between 4 GeV and 5 GeV, phase2 MC and phase2 data have a similar efficiency. In both cases, the lowest efficiency occurs at  $\phi \approx 0$ . According to figures 6.12 and A.5, we expect that most electrons have a momentum between 5 GeV and 8 GeV. For momenta between 5 GeV and 6 GeV phase2 data and phase2 MC have some differences in the calculated tracking efficiency. Phase2 MC has an efficiency between 0.80 and 0.95 with an exception of an efficiency drop at  $\phi \approx 0$ . This drop also appears on phase2 data, but for  $\phi > \text{abs}(1.5)$  the efficiency on phase2 data is much worse than phase2 MC. Here the efficiency falls partially below 0.7 for phase2 data. The biggest difference occurs for momenta between 6 GeV and 7 GeV. For phase2 MC, the tracking efficiency ranges between 0.87 and almost 1.00. But the efficiency oscillates heavily between 0.71 and 0.98 for phase2 data. In both cases the highest efficiency occurs at  $\phi \approx 0$ . For momenta between 7 GeV and 8 GeV, phase2 MC has a tracking efficiency of above 0.99 for all  $\phi$  angles. For phase2 data, the efficiency is also very high for  $\phi > \text{abs}(1)$ . But for  $\phi < \text{abs}(1)$  the efficiency falls down by over 10 %. The large errors for phase2 MC for momenta between 8 GeV and 9 GeV are caused by low statistics. This can be seen in the enumerator (figure ??) and denominator (figure ??) plots in the appendix. For phase2 data, the calculated tracking efficiency is around 0.95 most of the time. For  $\phi \approx 0$  the efficiency falls down a little.

change to only electrons

## 7. Phase2 Tracking Efficiency

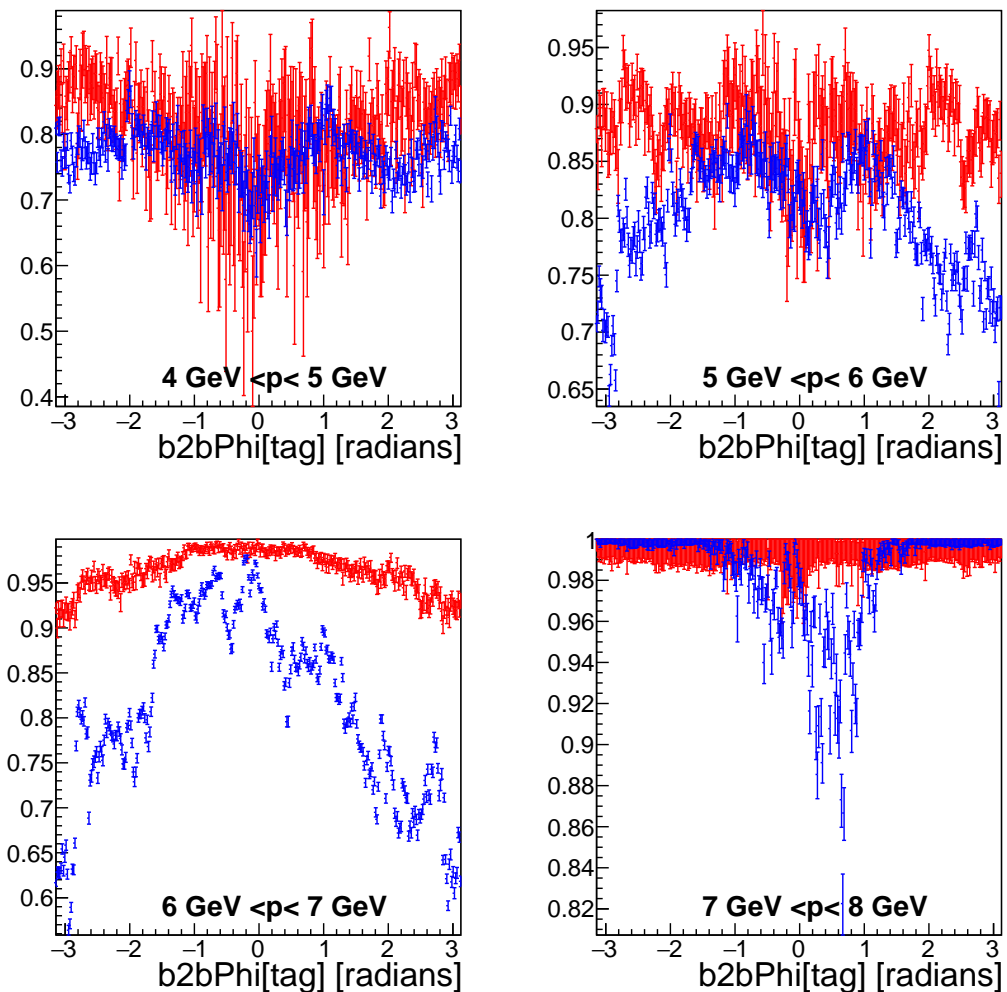


Figure 7.1.: Electron  $\phi$  tracking efficiency plots in the forward end cap. The tracking efficiency for phase2 data is shown in blue and phase2 MC in red.

## 7.1. Momentum Efficiencies

### 7.1.2. Barrel

In figure ?? the calculated tracking efficiency for the random case in the barrel is shown. For momenta between 3 GeV and 4 GeV, the efficiency of phase2 data and phase2 MC are close together and between 0.7 and 0.9. The only difference occurs at  $\phi \approx -2$ . Here, we have a slightly higher tracking efficiency for phase2 data than for phase2 MC. For momenta between 4 GeV and 6 GeV, the calculated tracking efficiency is between 0.95 and 0.99 for phase2 MC and 0.94 and 0.98 for phase2 data. The highest efficiencies are reached by momenta between 6 GeV and 7 GeV in the random case. For these momenta, phase2 MC has a calculated efficiency of over 0.99 for all  $\phi$  angles. The efficiency for phase2 data is slightly worse compared to phase2 MC. Especially for  $\phi \approx 0.5$ . For this  $\phi$  angle falls down to about 0.97.

Figure 7.2 shows the efficiencies of reconstructing an electron in the barrel for different momenta. For low electron momenta i.e. 3 GeV and 4 GeV, the efficiency is between 0.4 and 0.8 for phase2 MC and 0.5 and 0.8 for phase2 data. The tracking efficiency becomes better with increasing momenta. For momenta between 4 GeV and 5 GeV it is already between 0.74 and 0.94 for phase2 MC and between 0.75 and 0.91 for phase2 data. For both phase2 MC and phase2 data the efficiency has its minimum at  $\phi \approx 0$ . For momenta between 5 GeV and 6 GeV, the efficiency becomes even better. The tracking efficiency ranges between 0.92 and 0.99 for phase2 MC and between 0.91 and 0.97 for phase2 data. The structure of this efficiency is very similar compared to the tracking efficiency for momenta between 4 GeV and 5 GeV. In both cases the lowest efficiency occurs at  $\phi \approx 0$ . The best tracking efficiencies for electrons in the barrel appears at momenta between 6 GeV and 7 GeV. Here the efficiency for phase2 MC is between 0.99 and 1 and for phase2 data between 0.955 and 0.995. Again, the lowest calculated tracking efficiency occurs at  $\phi \approx 0.5$ . Without this drop, the tracking efficiency of phase2 data is between 0.980 and 0.995.

The calculated tracking efficiencies for positrons in the barrel can be found in figure 7.3. You can see that for momenta between 3 GeV and 4 GeV, the calculated tracking efficiency is between 0.74 and 0.92 for phase2 MC and phase2 data. The structure of the efficiency is also very similar between phase2 MC and phase2 data, meaning that in both cases the lowest efficiency occurs at  $\phi \approx 0$ . For momenta between 4 GeV 5 GeV the tracking efficiency is between 0.980 and 0.995 for phase2 MC and between 0.955 and 0.985 for phase2 data. The biggest difference between phase2 data and phase2 MC appears at  $\phi \approx 0.5$ . Here, the efficiency for phase2 data falls down significantly. For momenta between 5 GeV and 6 GeV, the tracking efficiency ranges between 0.97 and 1 for phase2 MC and 0.95 and 0.99 for phase2 data. The tracking efficiency for phase2 MC is higher by 0.02 compared to phase2 data for almost all  $\phi$  angles. The same is true for momenta between 6 GeV and 7 GeV except that the efficiency difference is about 0.03 in this case.

## 7. Phase2 Tracking Efficiency

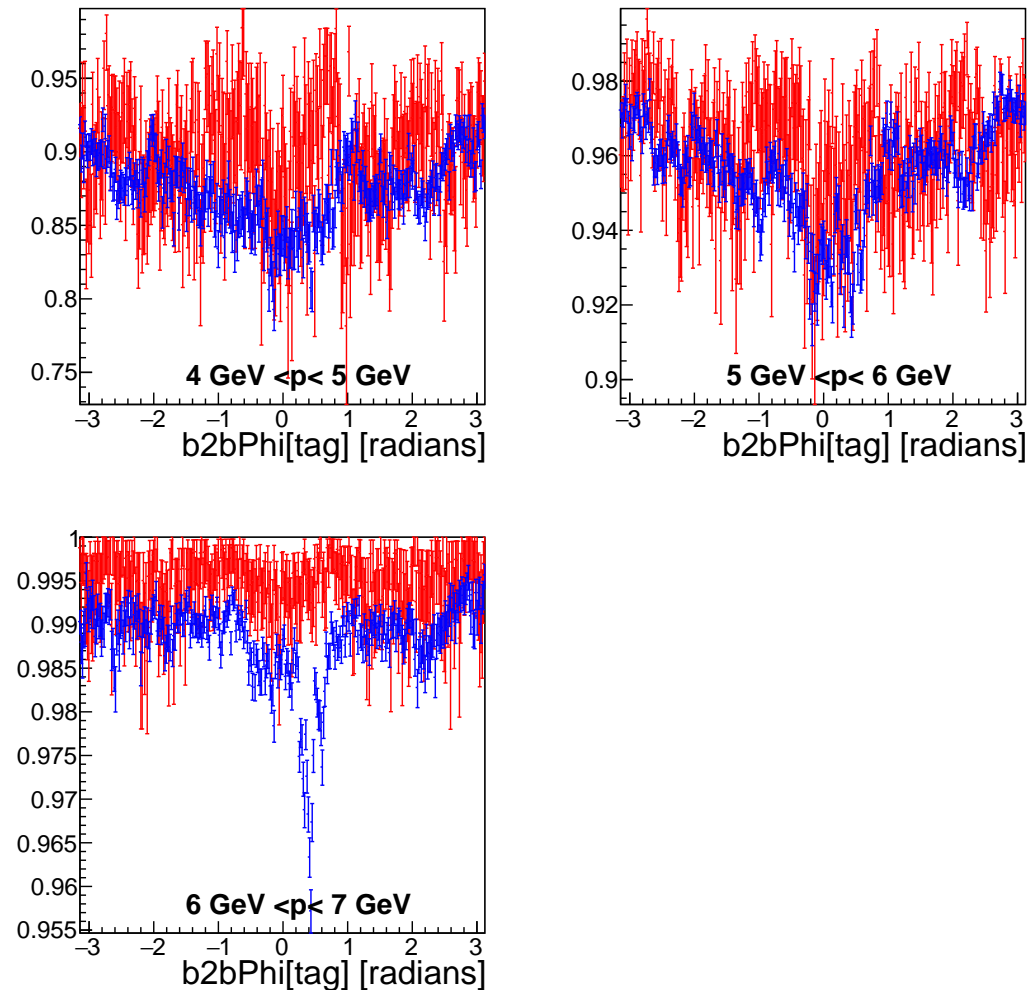


Figure 7.2.: Electron  $\phi$  tracking efficiency plots in the barrel. The tracking efficiency for phase2 data is shown in blue and phase2 MC in red.

### 7.1. Momentum Efficiencies

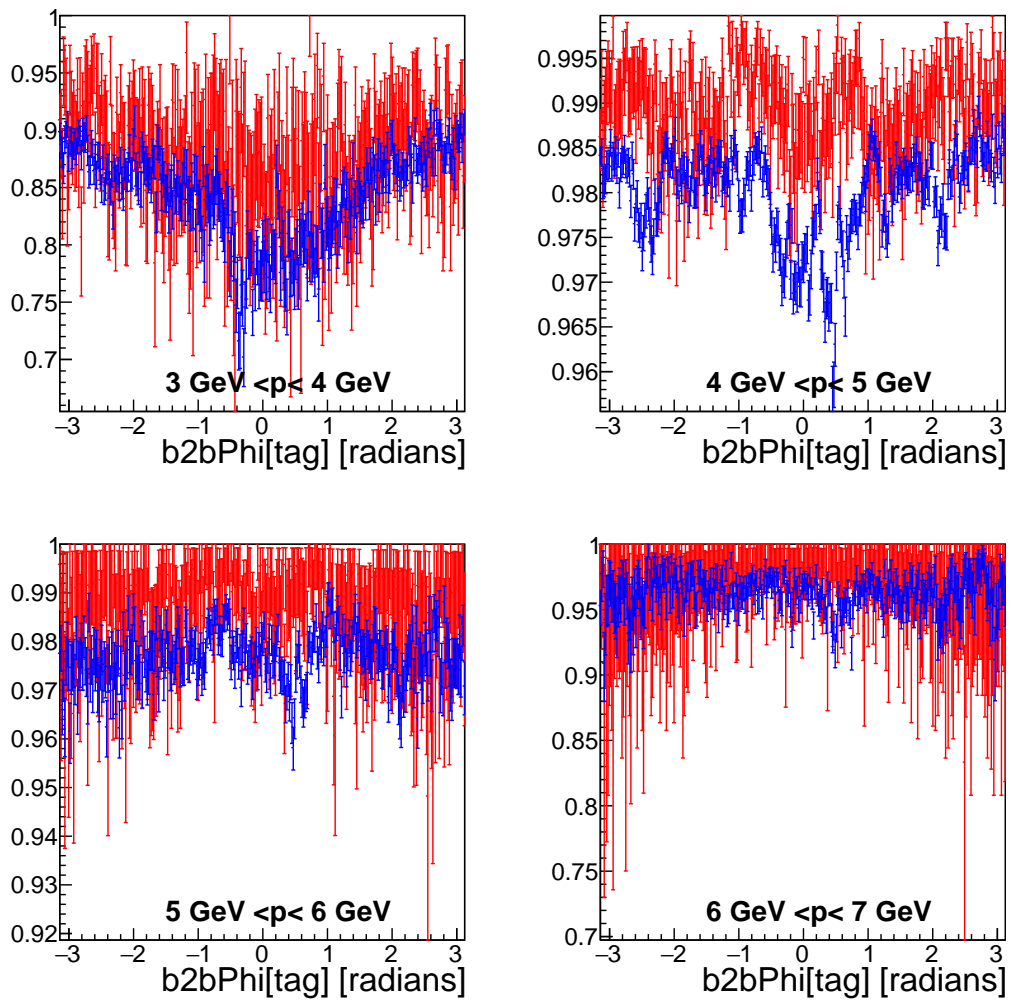


Figure 7.3.: Positron  $\phi$  tracking efficiency plots in the barrel. The tracking efficiency for phase2 data is shown in blue and phase2 MC in red.

## 7. Phase2 Tracking Efficiency

### 7.1.3. Backward End Cap

In figure ?? you can see the calculated tracking efficiency for different momenta in the random case in the backward end cap. But due to the kinematics at BelleII, most *probe* particles are positrons in the backward end cap. Therefore, the tracking efficiency in this figure is mostly influenced by positrons. For momenta between 2 GeV and 3 GeV, the calculated tracking efficiency is between 0.9 and 1 for phase2 MC and phase2 data. For momenta between 3 GeV and 4 GeV the tracking efficiency covers a very large range. For phase2 MC the efficiency is between 0.35 and 0.95 and for phase2 data between 0.25 and 0.85. For  $\phi < -1$ , the efficiency is slightly larger for phase2 data compared to phase2 MC. A strange structure occurs at  $\phi \approx 0$ . Starting at around  $\phi \approx -1.5$  the efficiency goes up from 0.5 to 0.85 at  $\phi \approx -0.5$ , then it goes back down to 0.7 before it reaches its maximum at  $\phi \approx 0$ . For phase2 data the highest efficiency is reached around  $\phi = 0$ . At  $\phi = 0$  the efficiency is down to 0.45. At  $\phi$  values slightly bigger than 0, the efficiency is back to its maximum, before it falls back down to 0.7 for phase2 MC and 0.4 for phase2 data. After that, for phase2 MC the efficiency goes back up with a local maximum at  $\phi \approx 0.5$  before it falls back down for higher  $\phi$ . For phase2 data, the efficiency stays roughly the same for  $0.5 < \phi < 1.5$ . For higher  $\phi$  values the efficiency falls down, reaching its minimum at  $\phi \approx 2$ . After this the efficiency goes back up a little bit. A similar structure can be found for momenta between 4 GeV and 5 GeV. The only difference is that the efficiency is higher compared to the lower momenta. For momenta between 5 GeV and 6 GeV the efficiency is above 0.95 for both phase2 MC and phase2 data with the exception of  $\phi \approx 0$ . Here, the error of the calculated efficiencies are very large due to the lack of statistics. This can be seen in figures ?? to ??.

Figure 7.4 shows the calculated tracking efficiencies for the positron in the backward end cap. Since there are almost no electrons detected in the backward end cap, the tracking efficiency for positrons is almost the same as for the random case.

### 7.1. Momentum Efficiencies

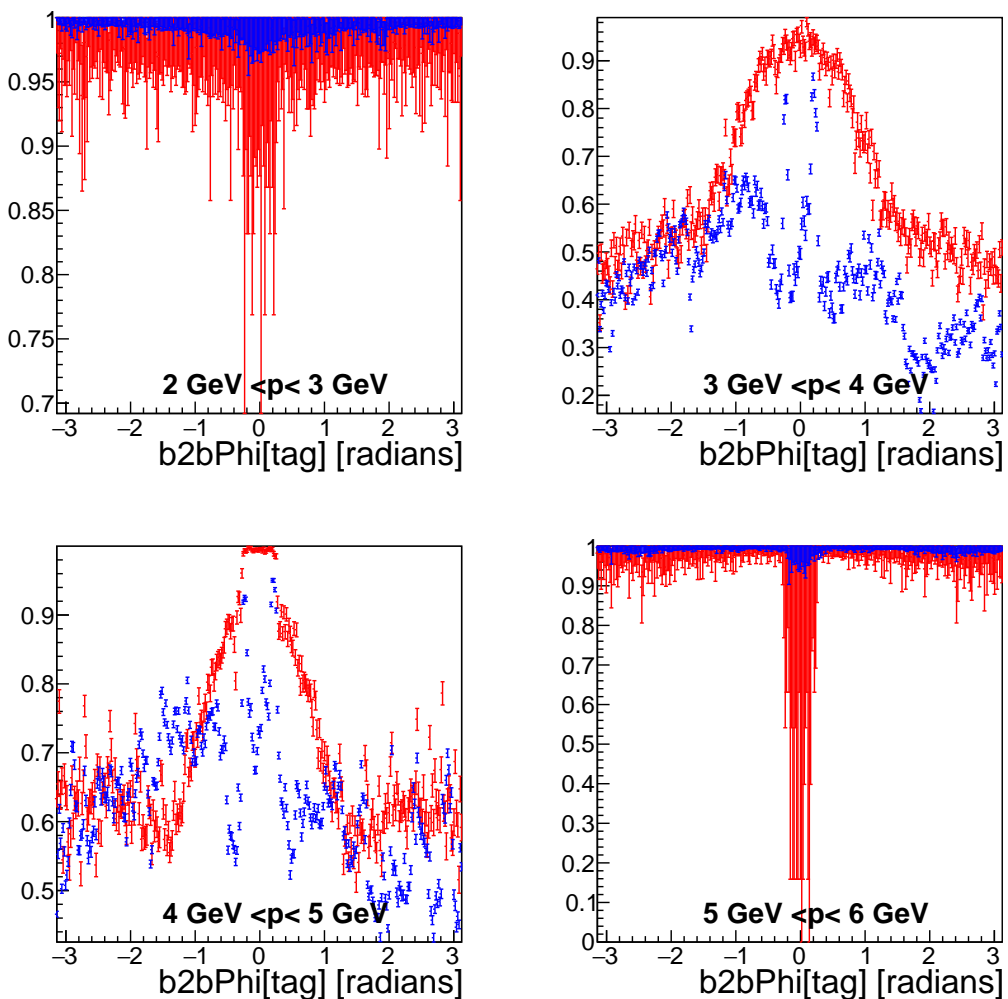


Figure 7.4.: Positron  $\phi$  tracking efficiency plots in the backward end cap. The tracking efficiency for phase2 data is shown in blue and phase2 MC in red.

## 7. Phase2 Tracking Efficiency

### 7.1.4. $\theta$ Efficiencies

This section will present the present the calculated tracking efficiencies as a function of the polar angle  $\theta$ . The pink lines in each of the following plots will indicate the different areas of the ECL. Due to the construction of the detector, it is only possible to detect particles with a polar angle of  $0.2967 < \theta < 2.6179$ .

auf electron aendern

Figure 7.5 shows the calculated tracking efficiency for different momenta in the random case as a function of the polar angle. For momenta between 2 GeV and 3 GeV, most reconstructed particles are positrons. Due to the kinematics at BelleII, most positrons hit the ECL with a high  $\theta$  angle. Therefore, they are mostly hitting the backward end cap. This efficiency was already discussed in section 7.1.3. In the barrel the error bars of the efficiency are getting bigger with decreasing  $\theta$  angle. For momenta between 3 GeV and 4 GeV, the calculated tracking efficiency starts rather high for small  $\theta$  angles. For phase2 MC and phase2 data the highest efficiency is in the forward end cap with roughly 0.9. But it falls down very quickly with increasing  $\theta$ . At the transition between the forward end cap and the barrel, the efficiency has a local minimum of only 0.2. For  $0.5 < \theta < 0.7$ , the efficiency goes back up to 0.6 very quickly. After this, the efficiency increases slowly to around 0.85 at  $\theta \approx 2.2$ . At roughly this angle the barrel ends and the backward end cap begins. In the backward end cap the efficiency goes up to over 0.9 at first for phase2 MC before it falls down to 0 rather quickly. In contrast, phase2 data falls down strictly monotonic in the backward end cap. For momenta between 4 GeV and 5 GeV the structure of the efficiency is similar to the momentum region we just look at. The only difference is that the efficiency drop at the forward end cap to barrel transition is not as dominant as before. Here, the efficiency only falls down to 0.6. Also, the highest efficiency is reached in the barrel at  $1.7 < \theta < 2.3$  for phase2 MC and  $1.7 < \theta < 2.2$  for phase2 data. The biggest difference between phase2 MC and phase2 data occurs again in the backward end cap. Here the efficiency for phase2 data falls down noticeably earlier compared to phase2 MC. For momenta between 5 GeV and 6 GeV, there is no dip in the efficiency at the transition between forward end cap and barrel. In the forward end cap the efficiency of phase2 data starts lower compared to the phase2 MC efficiency. But they meet at  $\theta \approx 0.4$  and increase up to approximately 0.95 and more at  $\theta \approx 1$ . For higher  $\theta$  values the efficiency in the barrel and the backward end cap stays more or less the same with the exception of a small dip in phase2 data at  $\theta \approx 1.8$ . The large error bars for phase2 MC at  $\theta \approx 2.1$  are caused by low statistic in this region. This can be seen in figure ?? and ???. In the plot for the momentum range between 6 GeV and 7 GeV, the efficiency for phase2 data starts lower compared to phase2 MC efficiency. In the barrel both efficiencies stay above 0.98 with an exception of a dip similar to the dip already mentioned at momenta between 5 GeV and 6 GeV. But this time, the dip appears at  $\theta \approx 1.2$ . Also, in the backward end cap, the tracking efficiency of phase2 data is higher than phase2 MC. For momenta between 7 GeV and 8 GeV most particles are reconstructed in the forward end cap. For phase2 MC the efficiency is about 0.99. This was already discussed in section 7.1.1. For phase2 the tracking

### 7.1. Momentum Efficiencies

efficiency is slightly lower. Again for phase2 data, a small dip in the tracking efficiency appears. The dip has a  $\theta$  angle of 0.4. For the last momentum range, similar to the previous momenta range, almost all of the reconstructed particles are reconstructed in the forward end cap. The tracking efficiency for phase2 MC and phase2 MC are above 0.95. The additional plots for the calculated tracking efficiency for the random case as a function of  $\theta$  can be found in the appendix, figures ?? to ??.

Figure 7.5 shows the calculated tracking efficiency of electrons as a function of the polar angle  $\theta$ . The efficiency for momenta between 3 GeV and 4 GeV is very similar to the efficiency we already discussed in the random case with the same momentum range. The only difference for electrons is that the error bars are larger due to the lower statistic. In the next momentum range a larger difference to the random case appears. For electrons the tracking tracking efficiency of phase2 data starts to decline at  $\theta \approx 1.5$ . This is not true for phase2 MC which starts to decline in the backward end cap. The tracking efficiencies for the momenta between 5 GeV and 6 GeV for the electrons is again similar to the random case. But since only electrons are taken into account the errors for  $\theta$  angles are large. The additional plots for the calculated electron tracking efficiency as a function of  $\theta$  can be found in the appendix, figures B.9 to ??.

In figure 7.6 the calculated tracking efficiency for positrons as a function of the polar angle  $\theta$  is shown.

## 7. Phase2 Tracking Efficiency

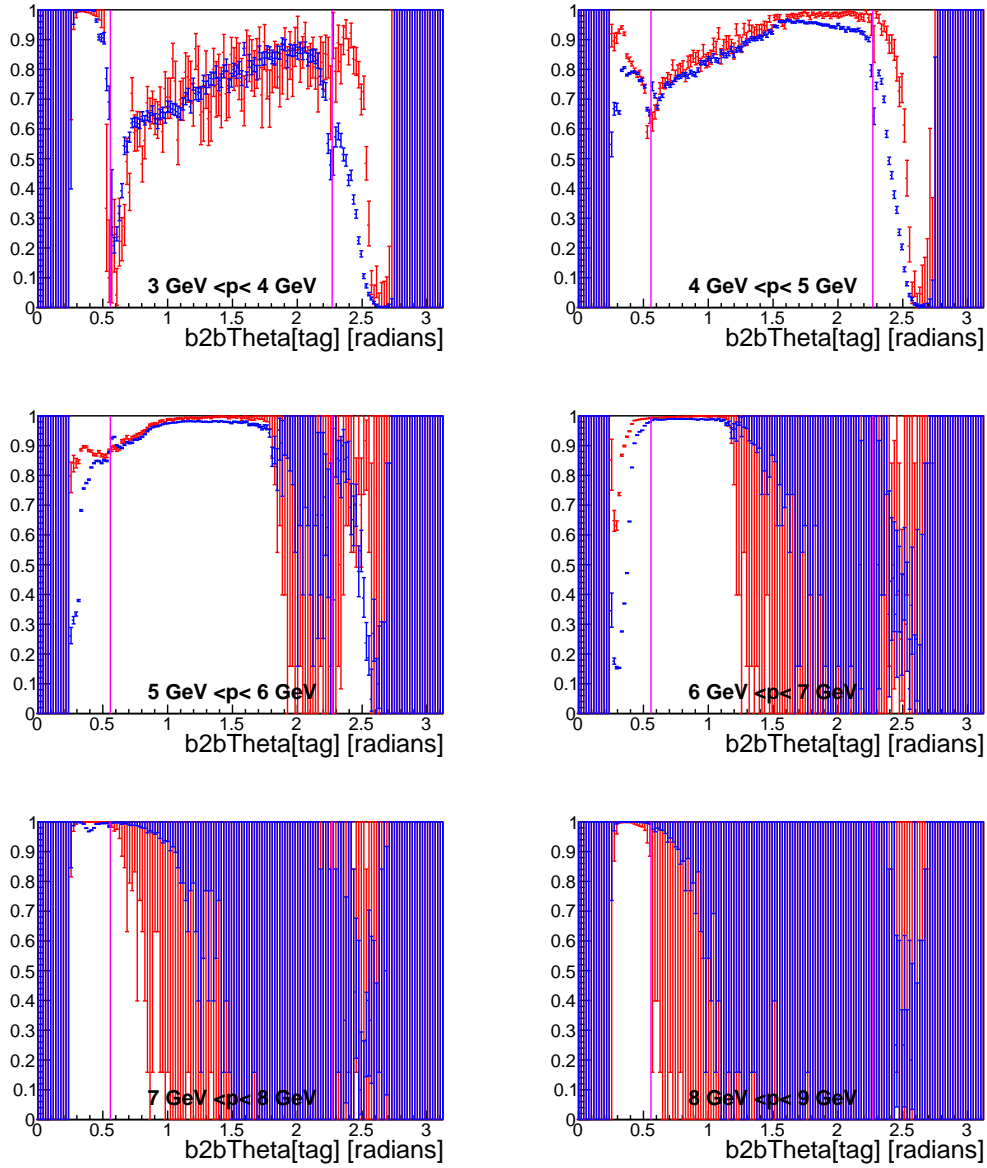


Figure 7.5.: Electron  $\theta$  momentum tracking efficiency plots. The tracking efficiency for phase2 data is shown in blue and phase2 MC in red. The pink line indicates the different sectors of the ECL.

### 7.1. Momentum Efficiencies

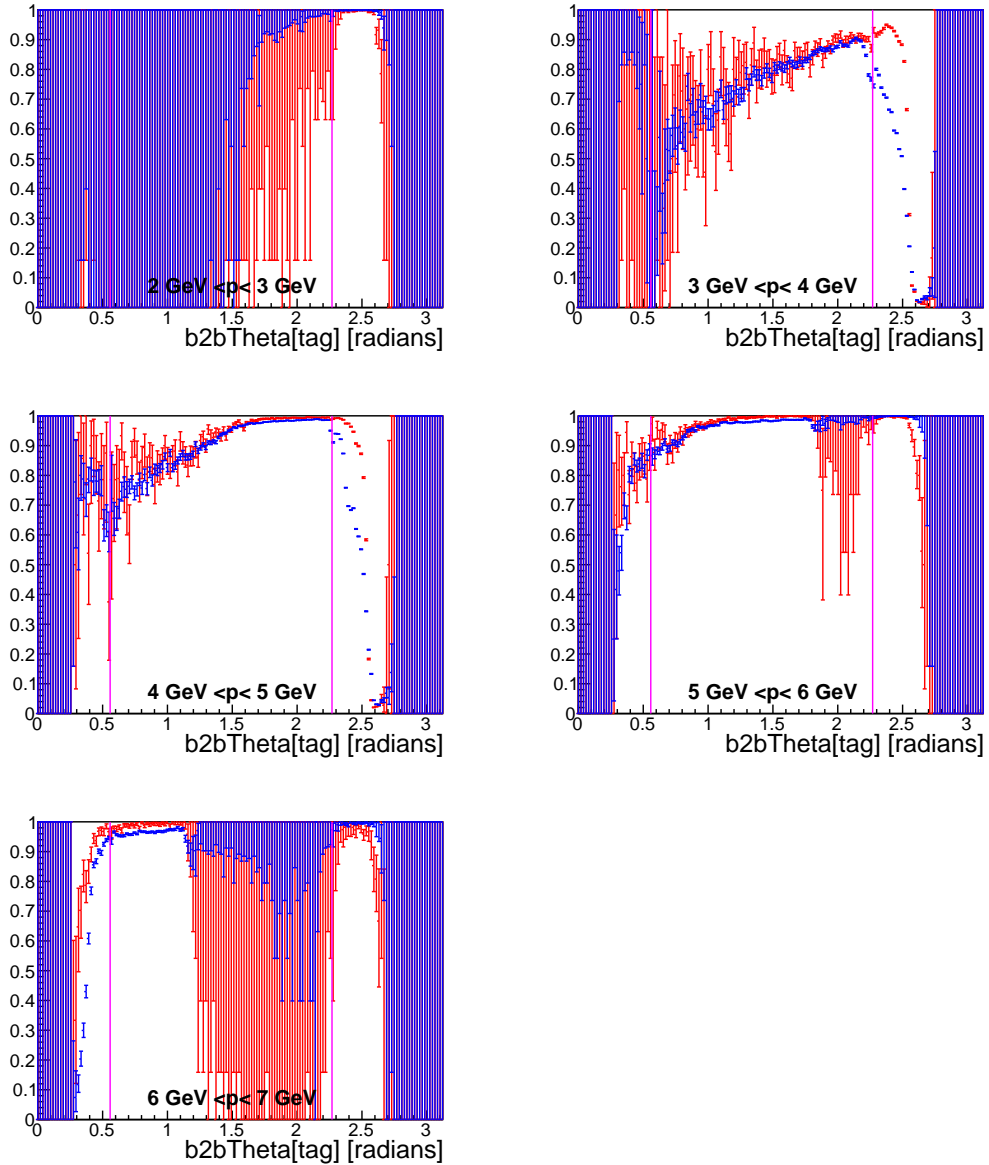


Figure 7.6.: Positron  $\theta$  momentum tracking efficiency plots. The tracking efficiency for phase2 data is shown in blue and phase2 MC in red. The pink line indicates the different sectors of the ECL.

7. Phase2 Tracking Efficiency

## 7.2. Transverse Momentum Efficiencies

### 7.2.1. Forward End Cap

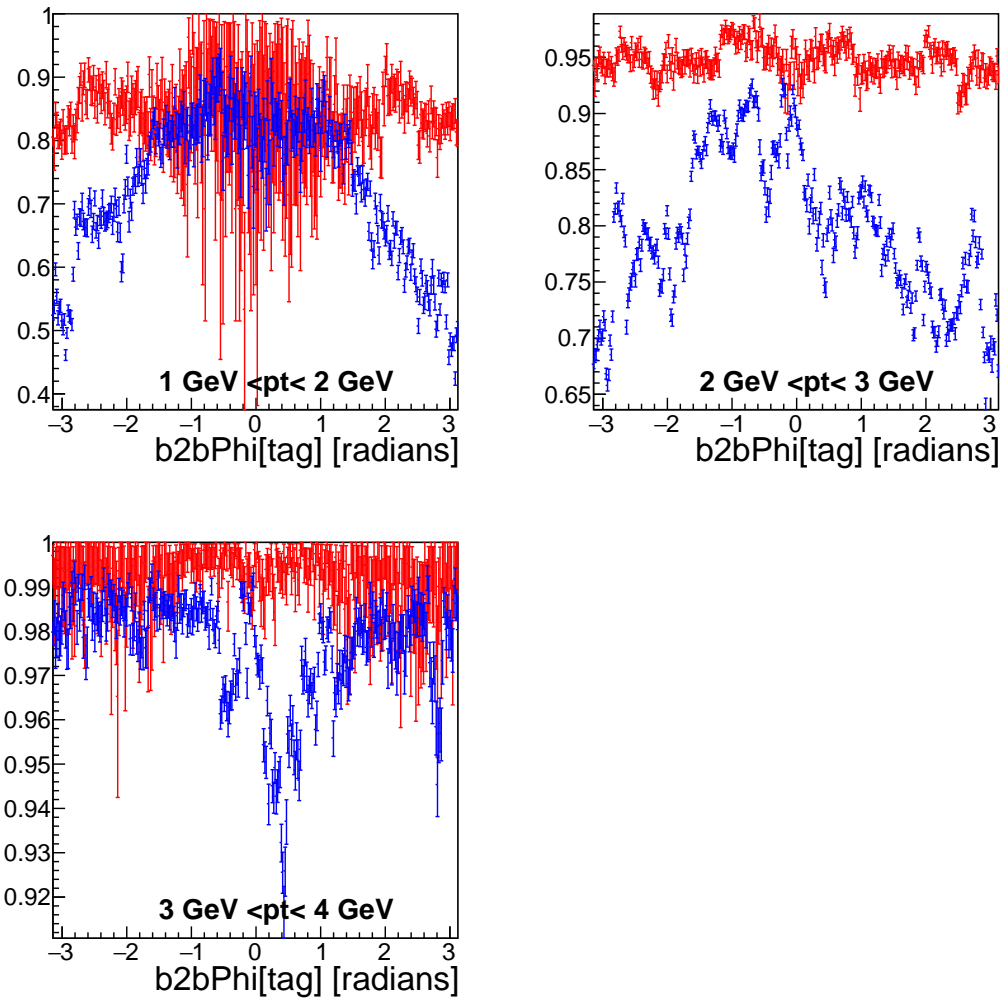


Figure 7.7.: Electron  $\phi$  transverse momentum tracking efficiency plots in the forward end cap. The tracking efficiency for phase2 data is shown in blue and phase2 MC in red.

## 7.2. Transverse Momentum Efficiencies

### 7.2.2. Barrel

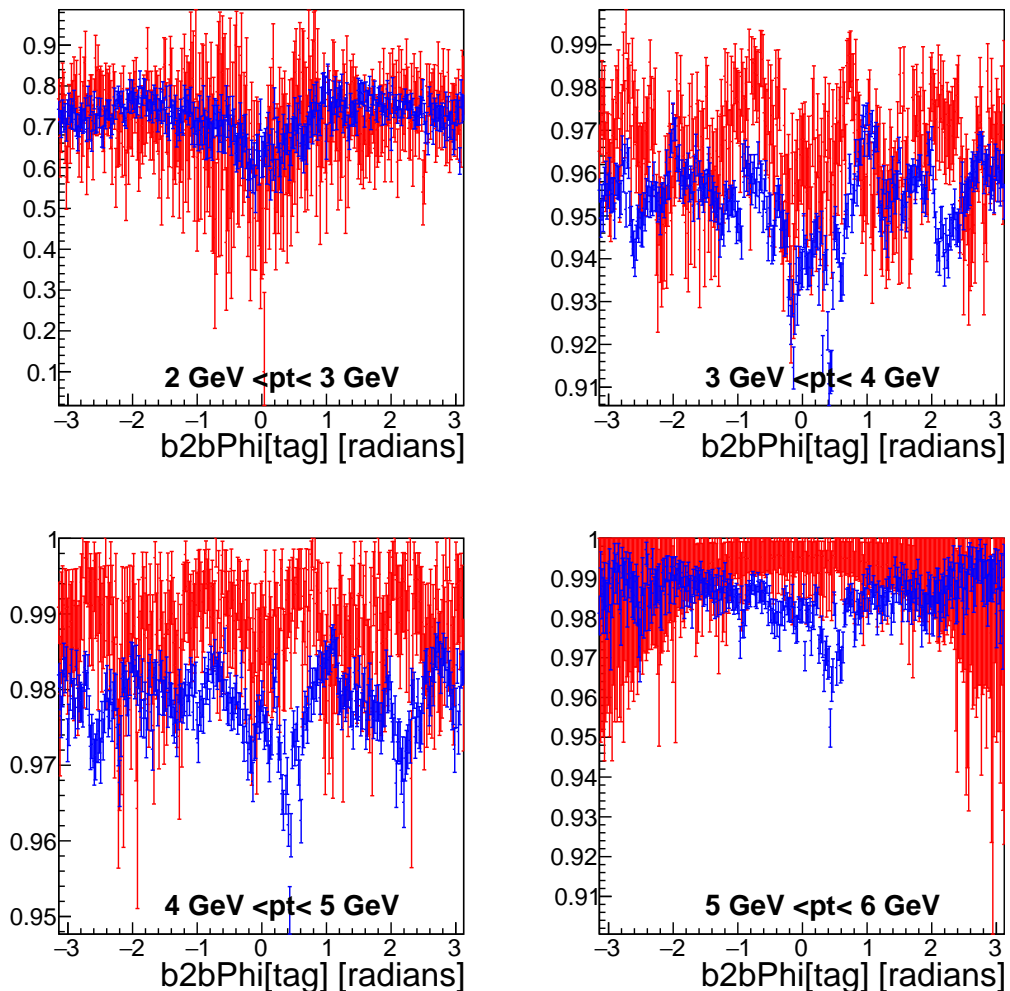


Figure 7.8.: Electron  $\phi$  transverse momentum tracking efficiency plots in the barrel.  
The tracking efficiency for phase2 data is shown in blue and phase2 MC in red.

## 7. Phase2 Tracking Efficiency

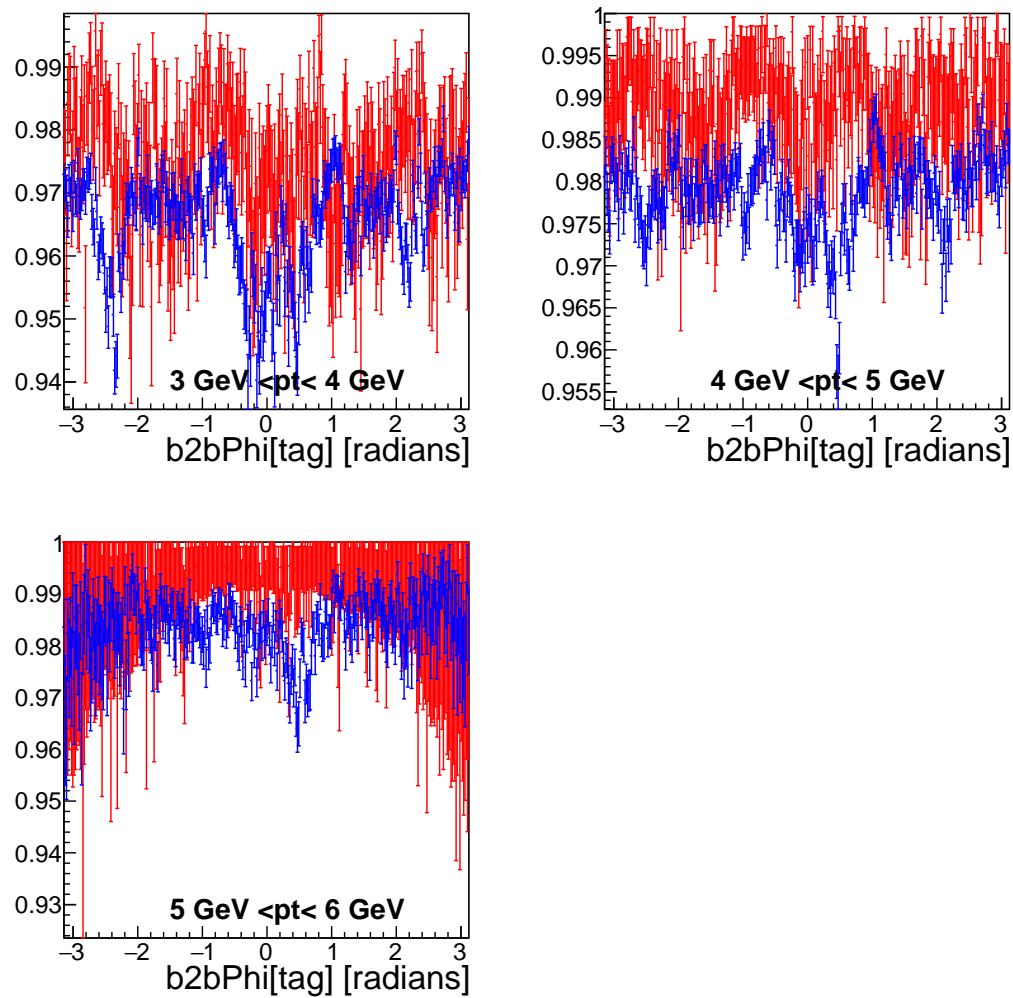


Figure 7.9.: Positron  $\phi$  transverse momentum tracking efficiency plots in the barrel.  
The tracking efficiency for phase2 data is shown in blue and phase2 MC in red.

## 7.2. Transverse Momentum Efficiencies

### 7.2.3. Backward End Cap

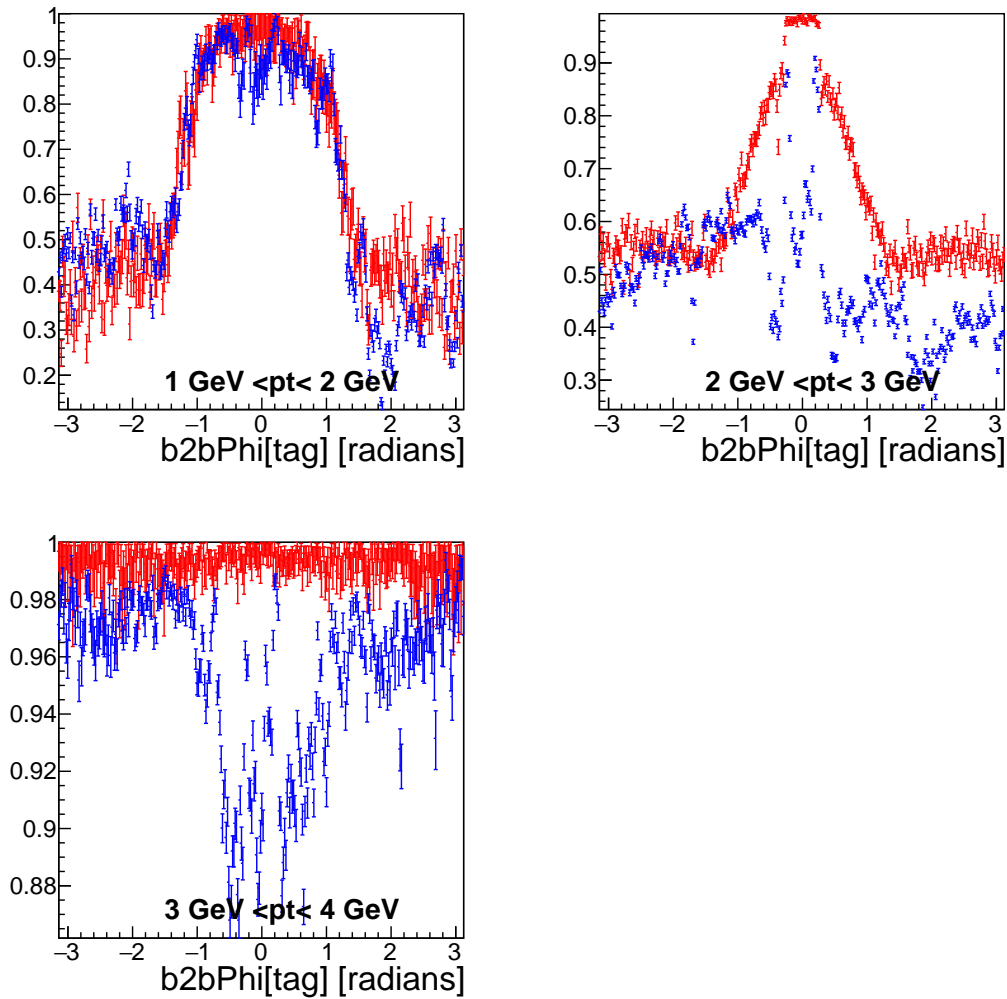


Figure 7.10.: Positron  $\phi$  transverse momentum tracking efficiency plots in the backward end cap. The tracking efficiency for phase2 data is shown in blue and phase2 MC in red.

## 7. Phase2 Tracking Efficiency

### 7.2.4. $\theta$ Efficiencies

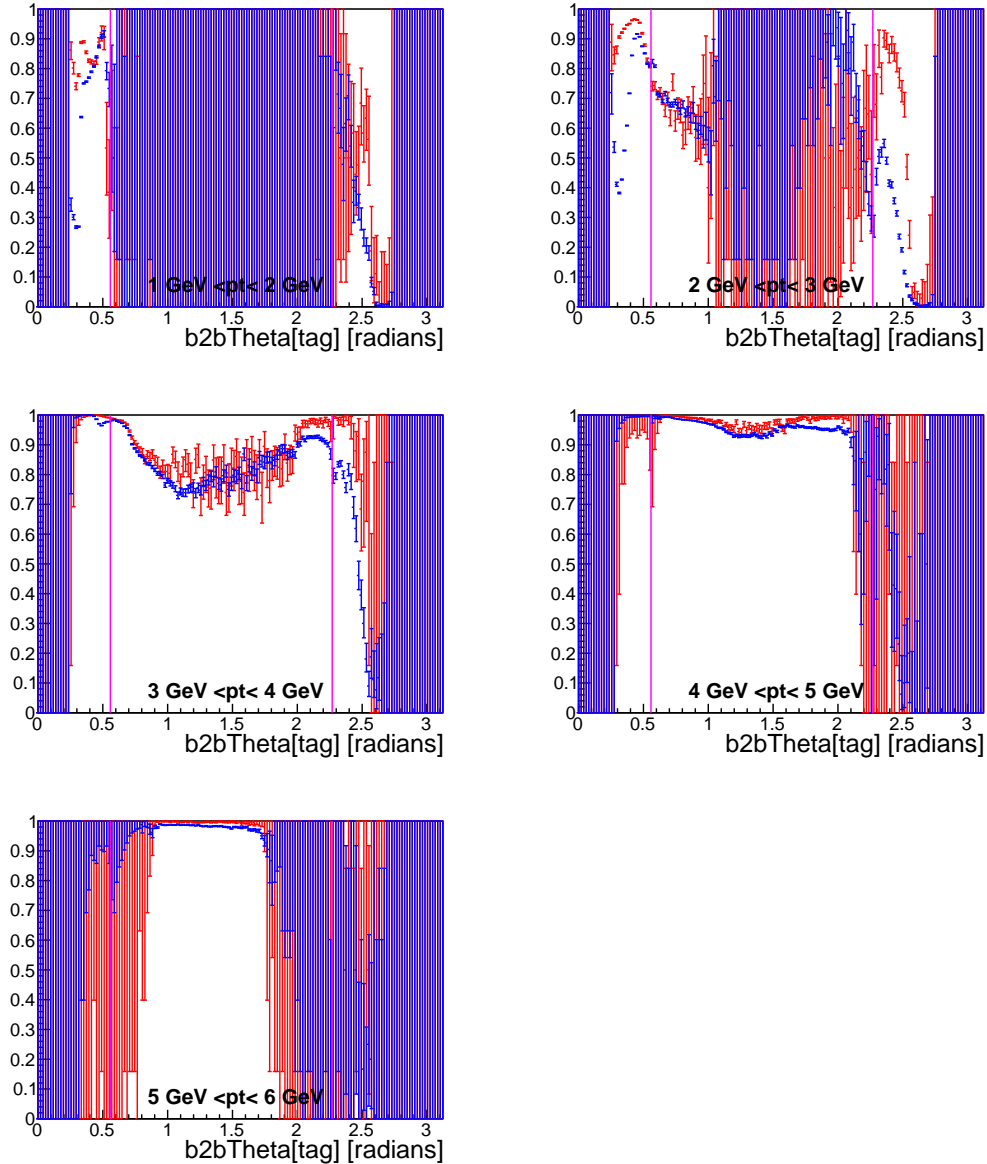


Figure 7.11.: Electron  $\theta$  transverse momentum tracking efficiency plots. The tracking efficiency for phase2 data is shown in blue and phase2 MC in red. The pink line indicates the different sectors of the ECL.

## 7.2. Transverse Momentum Efficiencies

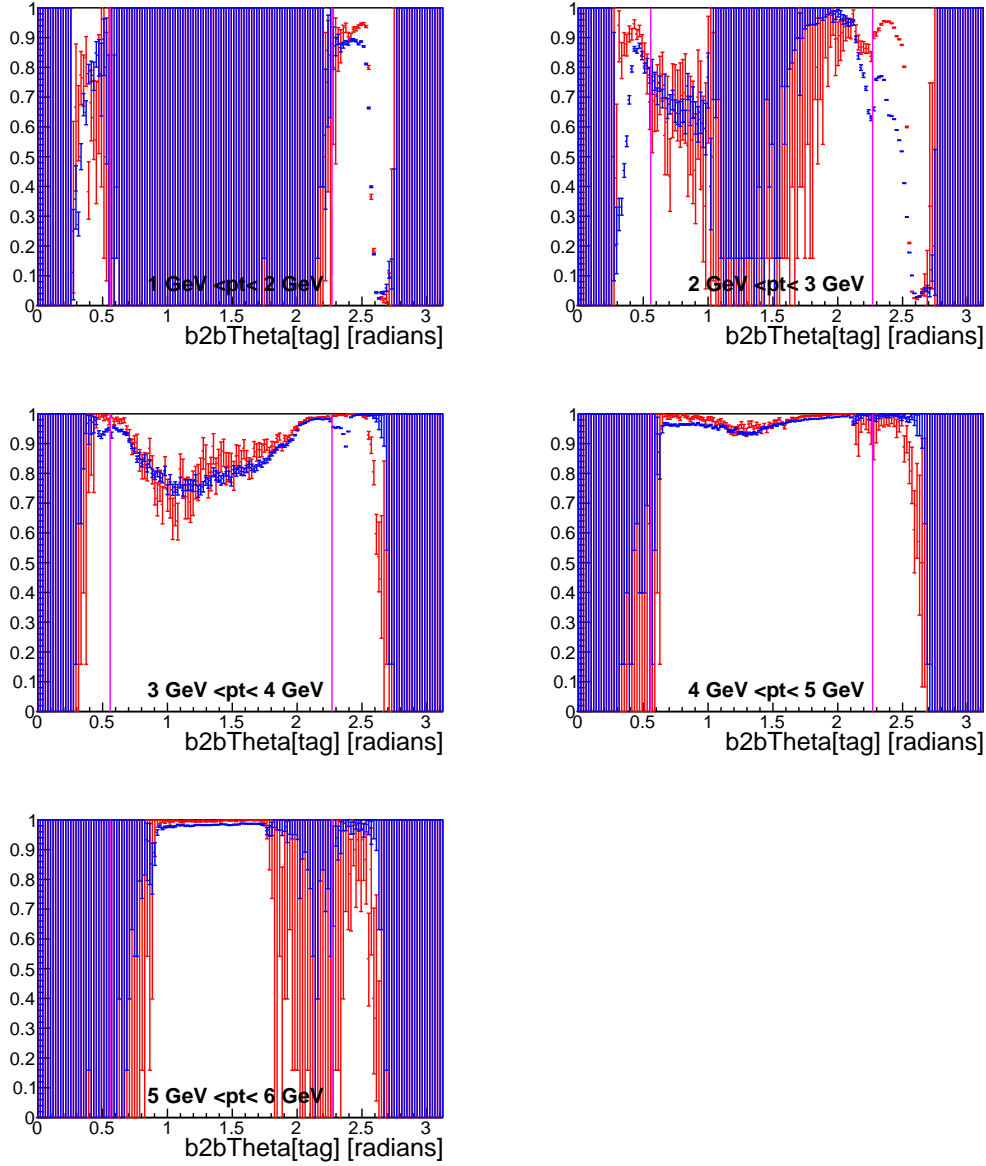


Figure 7.12.: Positron  $\theta$  transverse momentum tracking efficiency plots. The tracking efficiency for phase2 data is shown in blue and phase2 MC in red. The pink line indicates the different sectors of the ECL.



**8.1. Phase3****8.2. Location**

/belle/MC/release-01-00-02/DB00000294/MC10/prod00004664/s00/e0000/4S/  
r00000/3600520000/mdst/sub00

**8.3. Exp7****8.4. Exp8**

All Files at  
except 1544

**8.5. Selected Candidates****8.6. Tracking Efficiency**

MC10



CHAPTER

# 9

---

## Conclusion



---

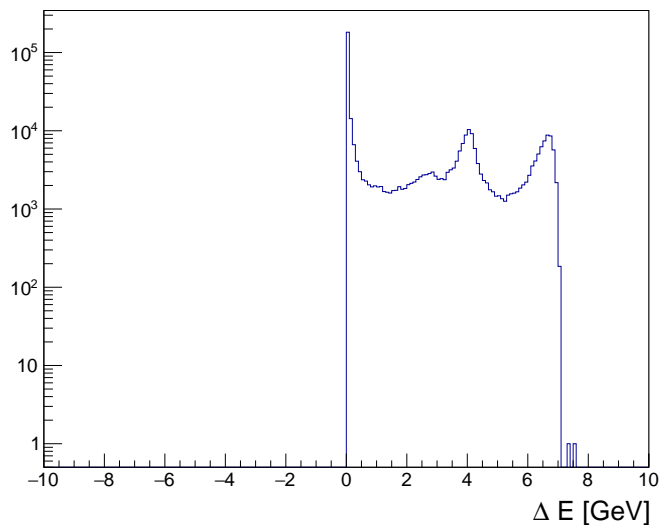
**A** Additional Preparation Plots

Figure A.1.:  $\text{clusterE}(\text{HclE}) - \text{clusterE}(\text{LclE})$  of the reconstructed candidates. This shows that the HclE daughters has always a higher cluster energy than the LclE daughter.

### A. Additional Preparation Plots

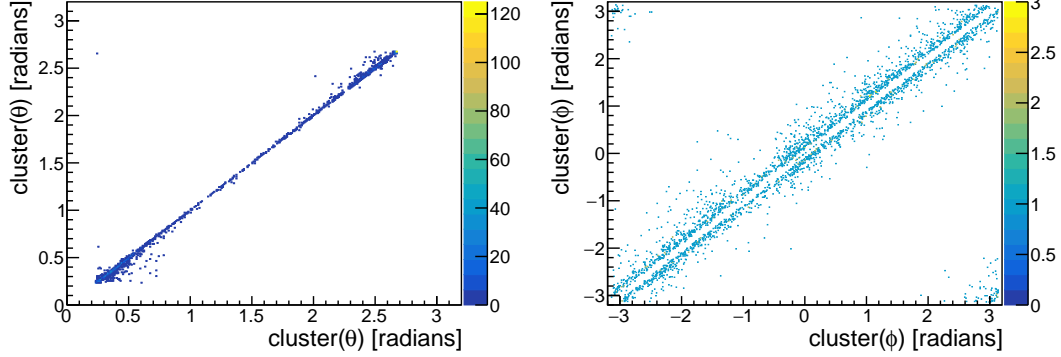


Figure A.2.: Left: The  $\theta$  angle of the clusters after the *cluster splitting*. Almost all the time, both clusters have the same  $\theta$  angle. Right: The  $\phi$  angle of the clusters after the *cluster splitting*. The  $\phi$  angle of both clusters are always slightly different. Therefore, *cluster splitting* always occurs along the polar angle.

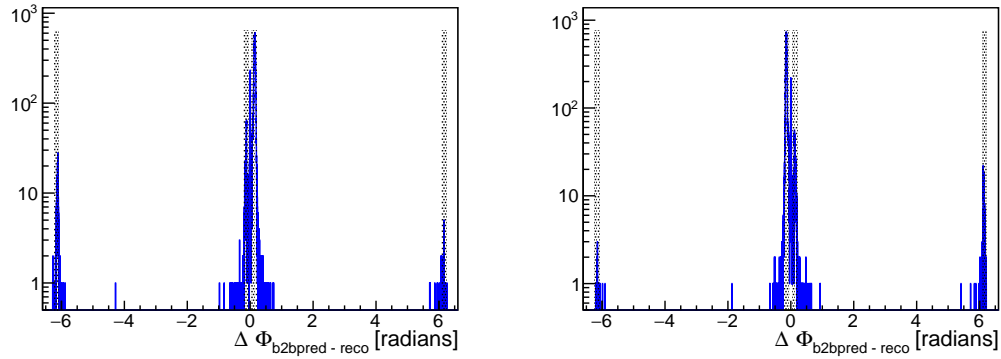


Figure A.3.: Left: Predicted  $\text{clusterPhi}(\text{HclE})$  - Reconstructed  $\text{clusterPhi}(\text{LclE})$ . Right: Predicted  $\text{clusterPhi}(\text{LclE})$  - Reconstructed  $\text{clusterPhi}(\text{HclE})$ . Only particles within the gray area are taken into account. Both plots are created with Beamtime-Data. Note the logarithmic scale.

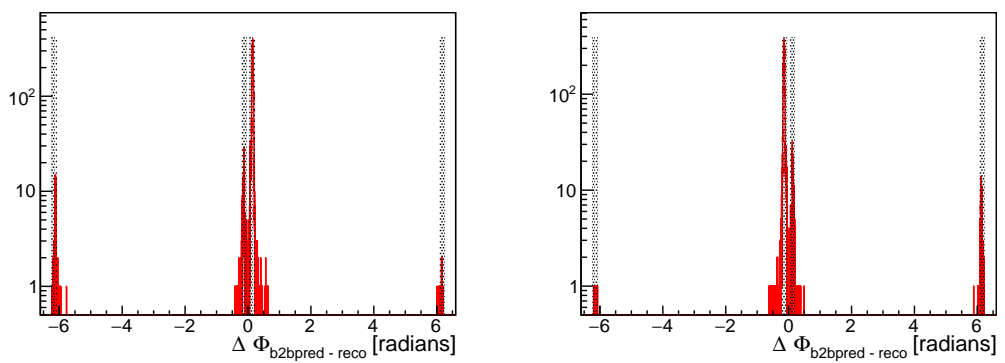


Figure A.4.: Left: Predicted clusterPhi(HclE) - Reconstructed clusterPhi(LclE).  
 Right: Predicted clusterPhi(LclE) - Reconstructed clusterPhi(HclE).  
 Only particles within the gray area are taken into account. Both plots  
 are created with MC data. Note the logarithmic scale.

### A. Additional Preparation Plots

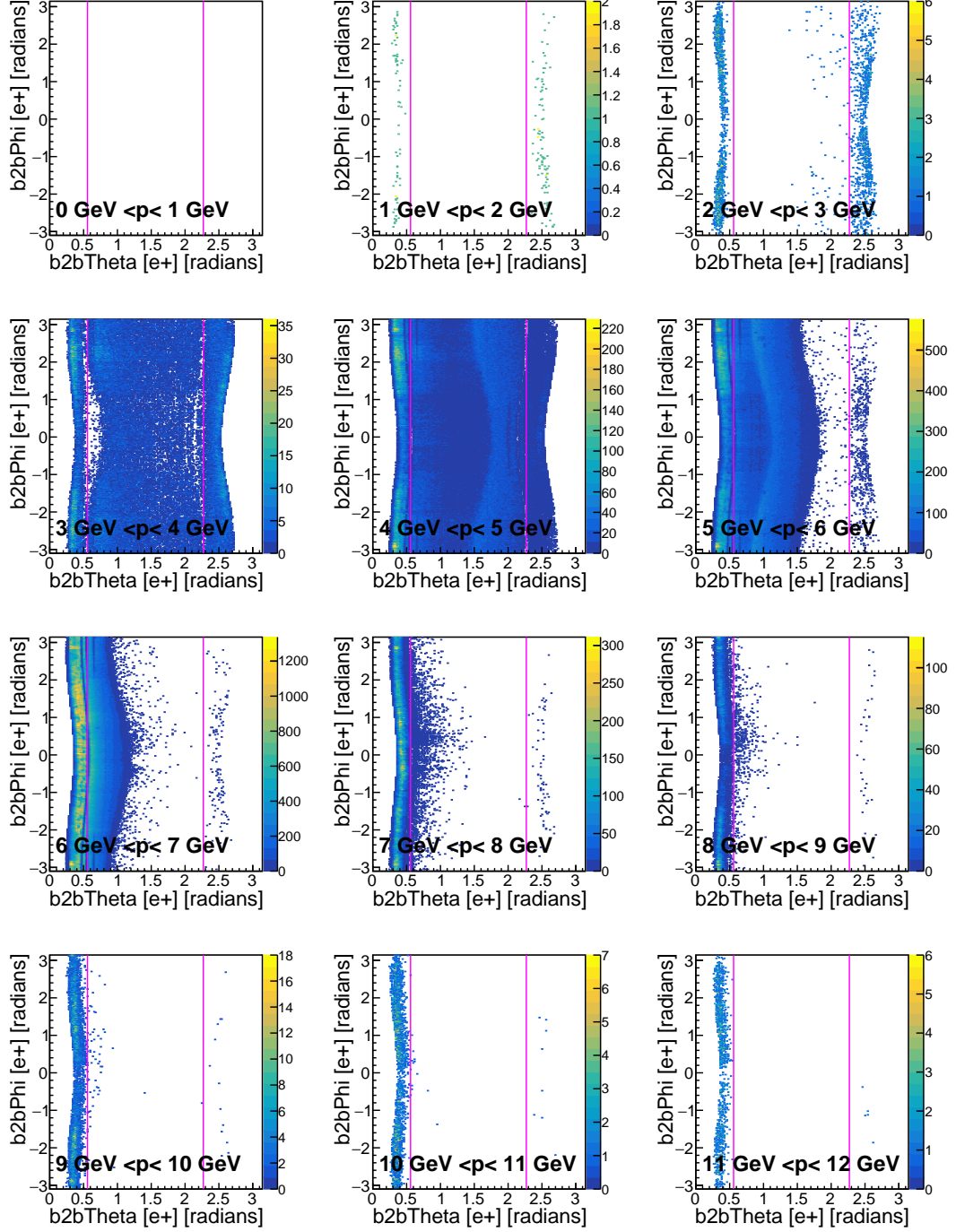


Figure A.5.: Predicted  $\theta$  and  $\phi$  denominator histograms of the *probe* particle for different momenta for electrons for phase2 Data are shown. The different areas of interest are indicated by the pink line.

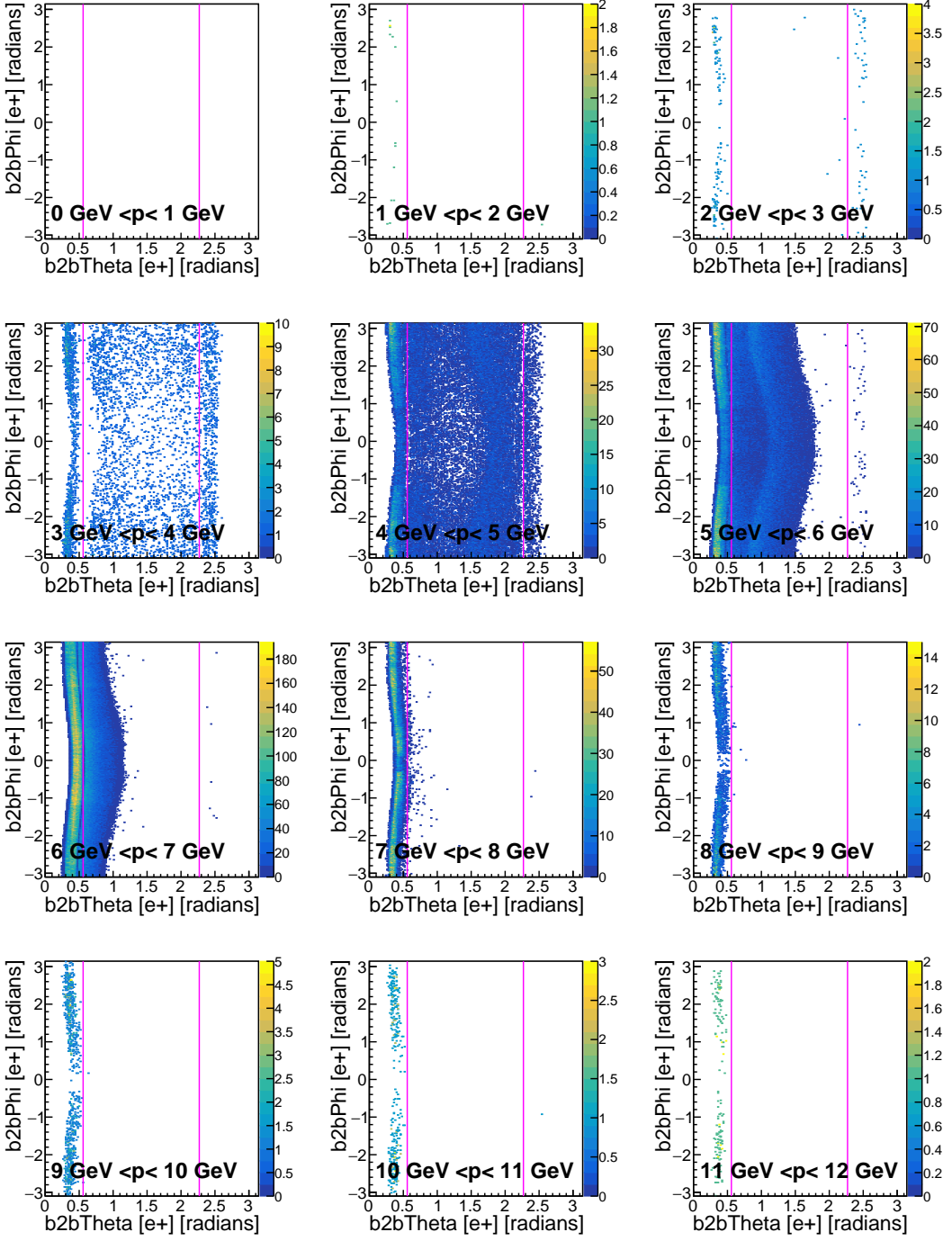


Figure A.6.: Predicted  $\theta$  and  $\phi$  enumerator histograms of the *probe* particle for different momenta for electrons for phase2 MC are shown. The different areas of interest are indicated by the pink line.

### A. Additional Preparation Plots

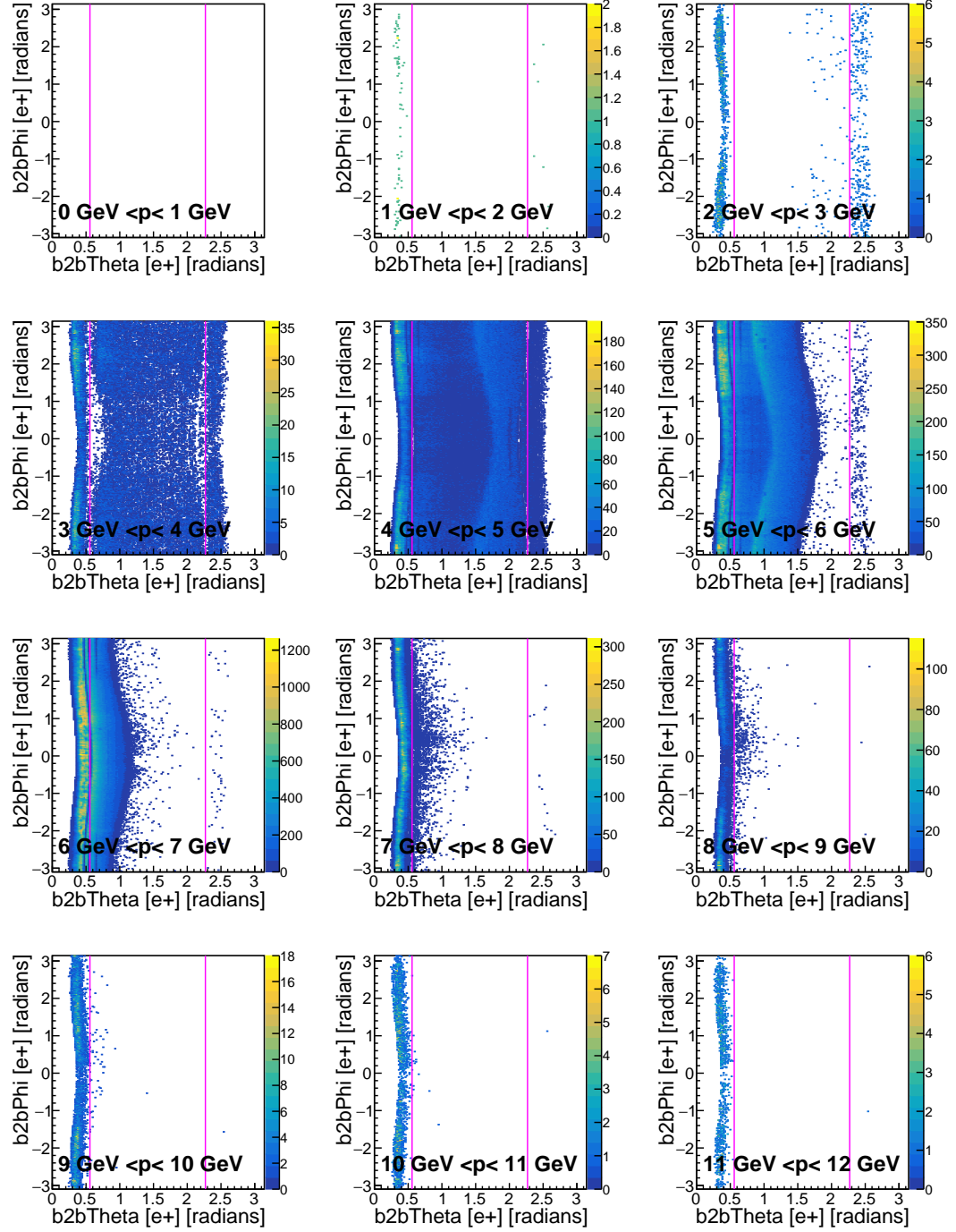


Figure A.7.: Predicted  $\theta$  and  $\phi$  enumerator histograms of the *probe* particle for different momenta for electrons for phase2 data are shown. The different areas of interest are indicated by the pink line.

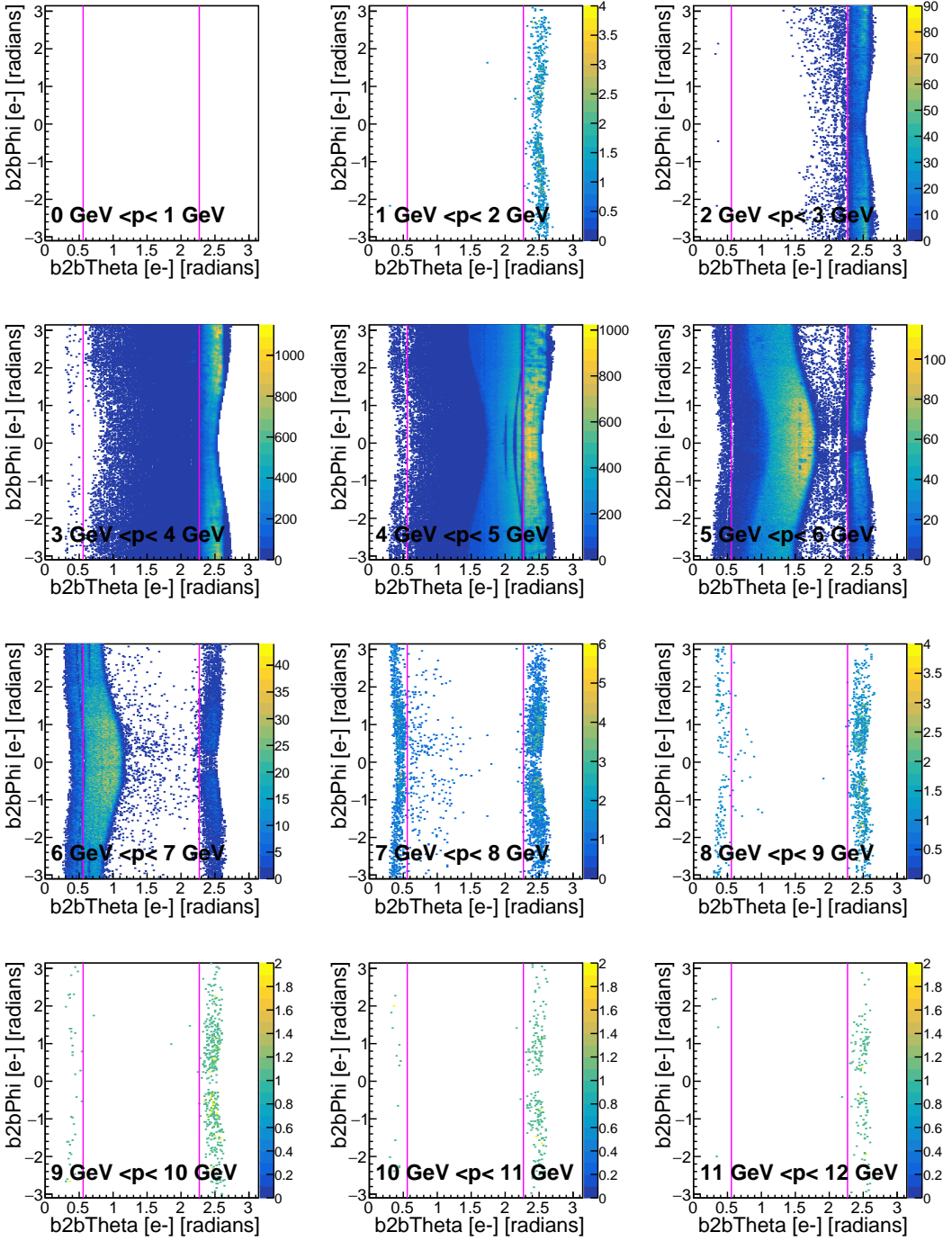


Figure A.8.: Predicted  $\theta$  and  $\phi$  denominator histograms of the *probe* particle for different momenta for positrons for phase2 Data are shown. The different areas of interest are indicated by the pink line.

### A. Additional Preparation Plots

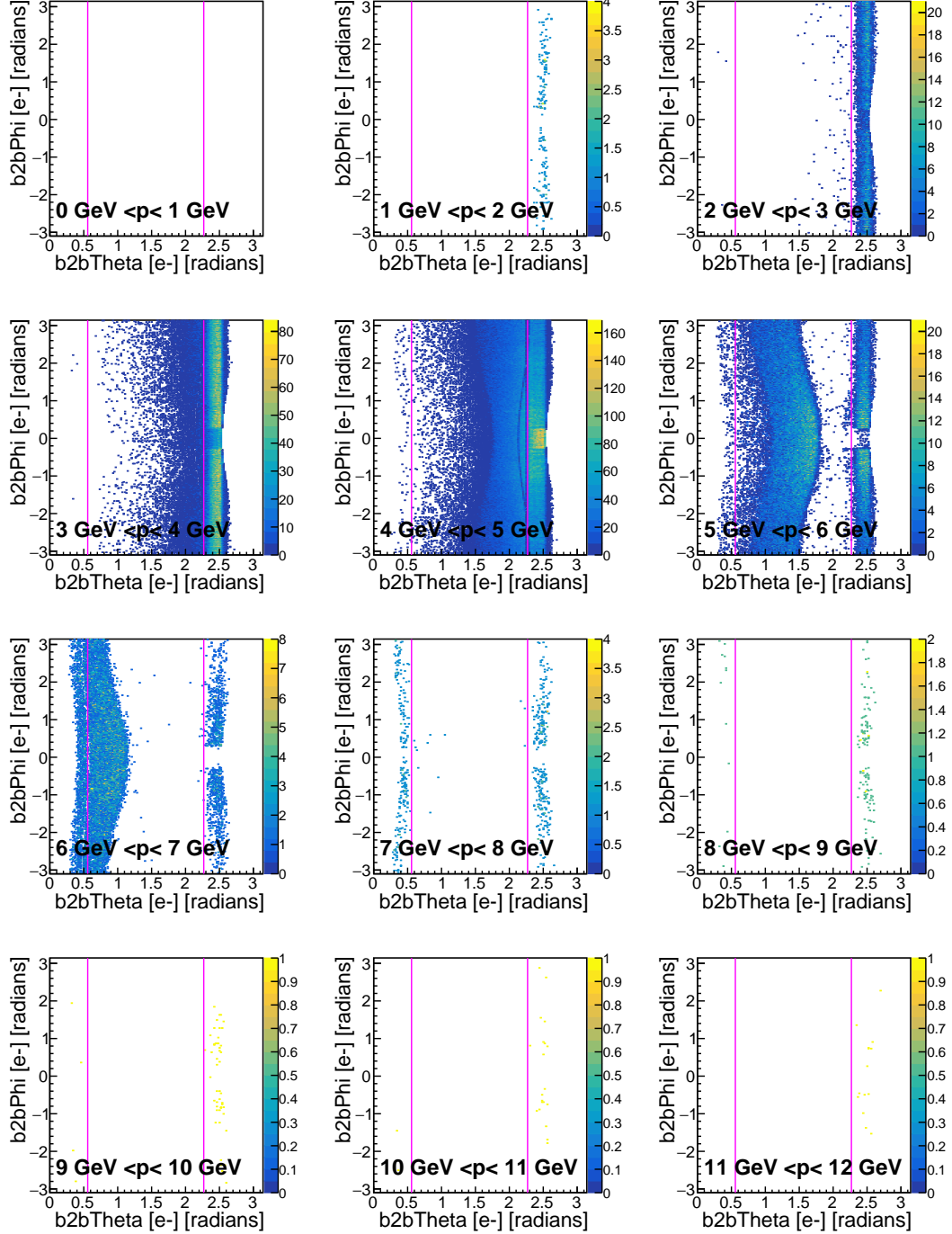


Figure A.9.: Predicted  $\theta$  and  $\phi$  denominator histograms of the *probe* particle for different momenta for positrons for phase2 MC are shown. The different areas of interest are indicated by the pink line.

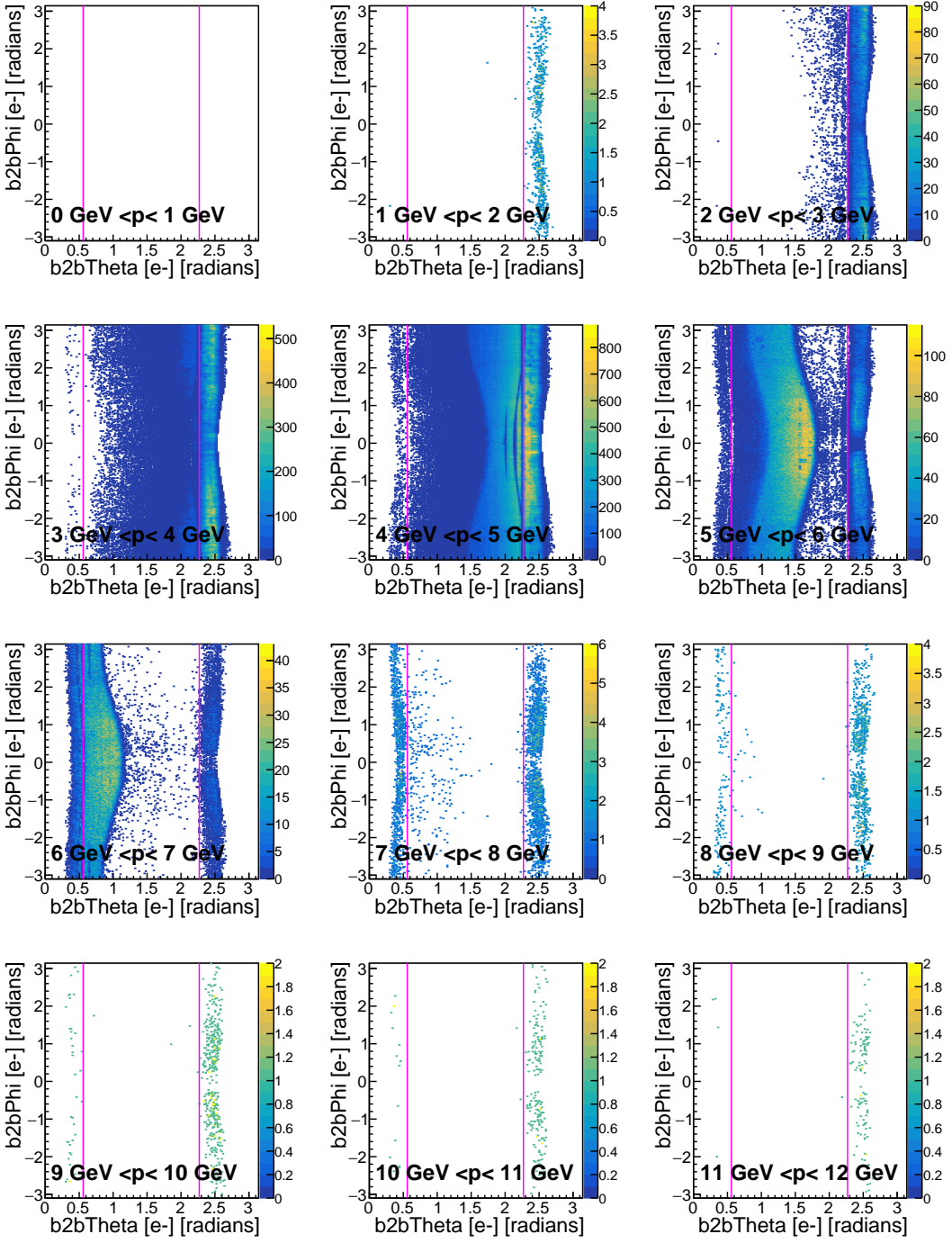


Figure A.10.: Predicted  $\theta$  and  $\phi$  denominator histograms of the *probe* particle for different momenta for positrons for phase2 Data are shown. The different areas of interest are indicated by the pink line.

### A. Additional Preparation Plots

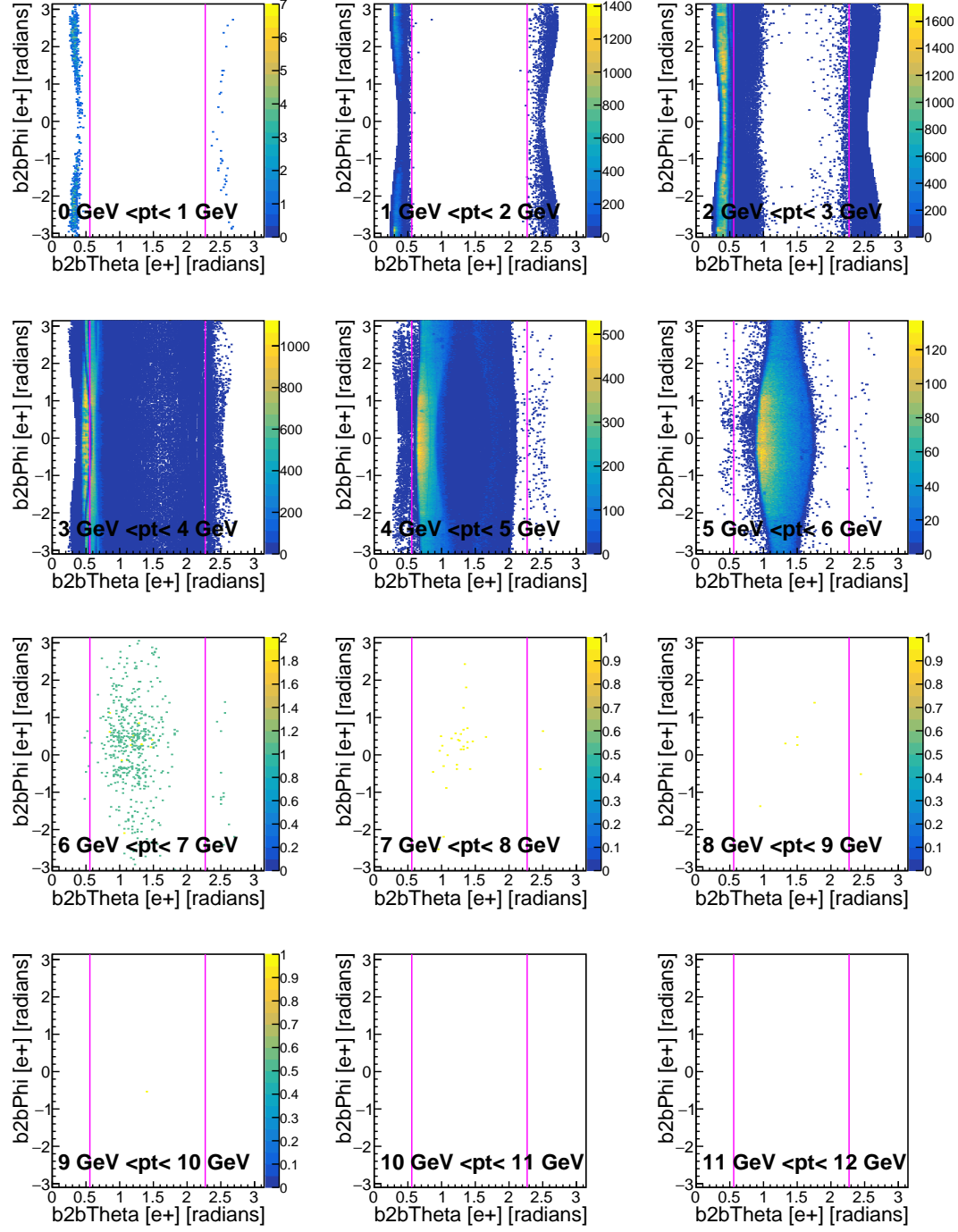


Figure A.11.: Predicted  $\theta$  and  $\phi$  denominator histograms of the *probe* particle for different transverse momenta for electrons for phase2 Data are shown. The different areas of interest are indicated by the pink line.

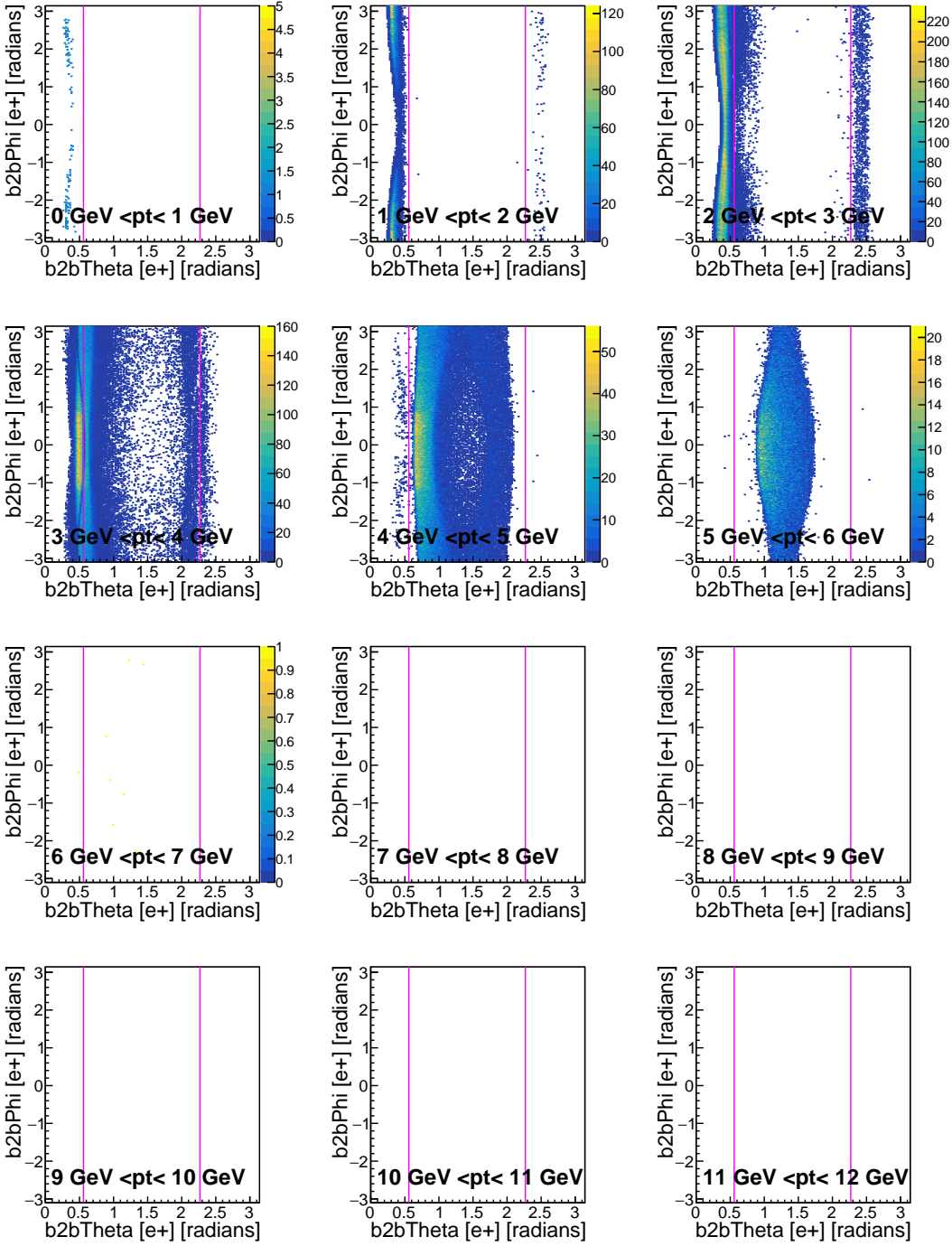


Figure A.12.: Predicted  $\theta$  and  $\phi$  denominator histograms of the *probe* particle for different transverse momenta for electrons for phase2 MC are shown. The different areas of interest are indicated by the pink line.

### A. Additional Preparation Plots

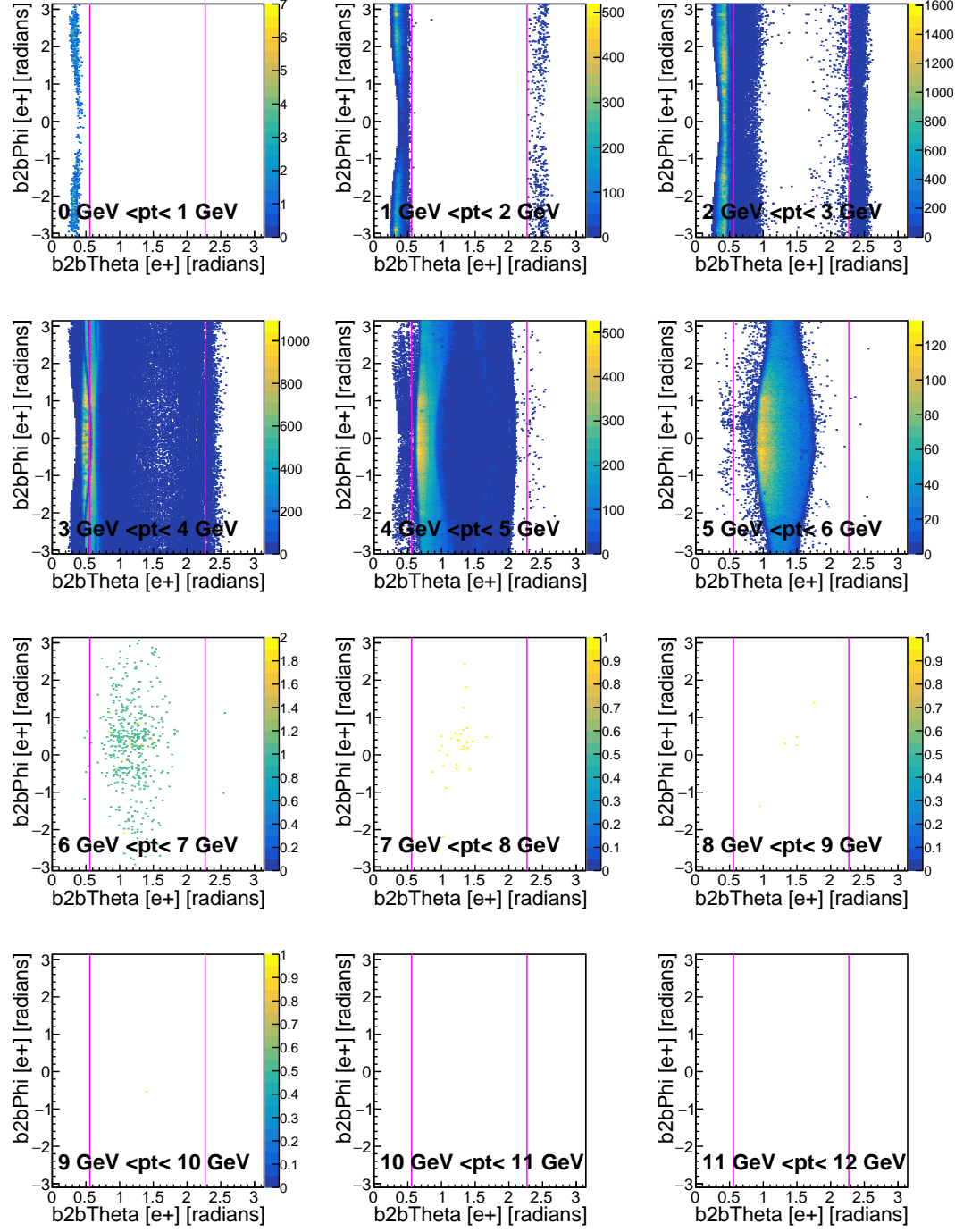


Figure A.13.: Predicted  $\theta$  and  $\phi$  denominator histograms of the *probe* particle for different transverse momenta for electrons for phase2 data are shown. The different areas of interest are indicated by the pink line.

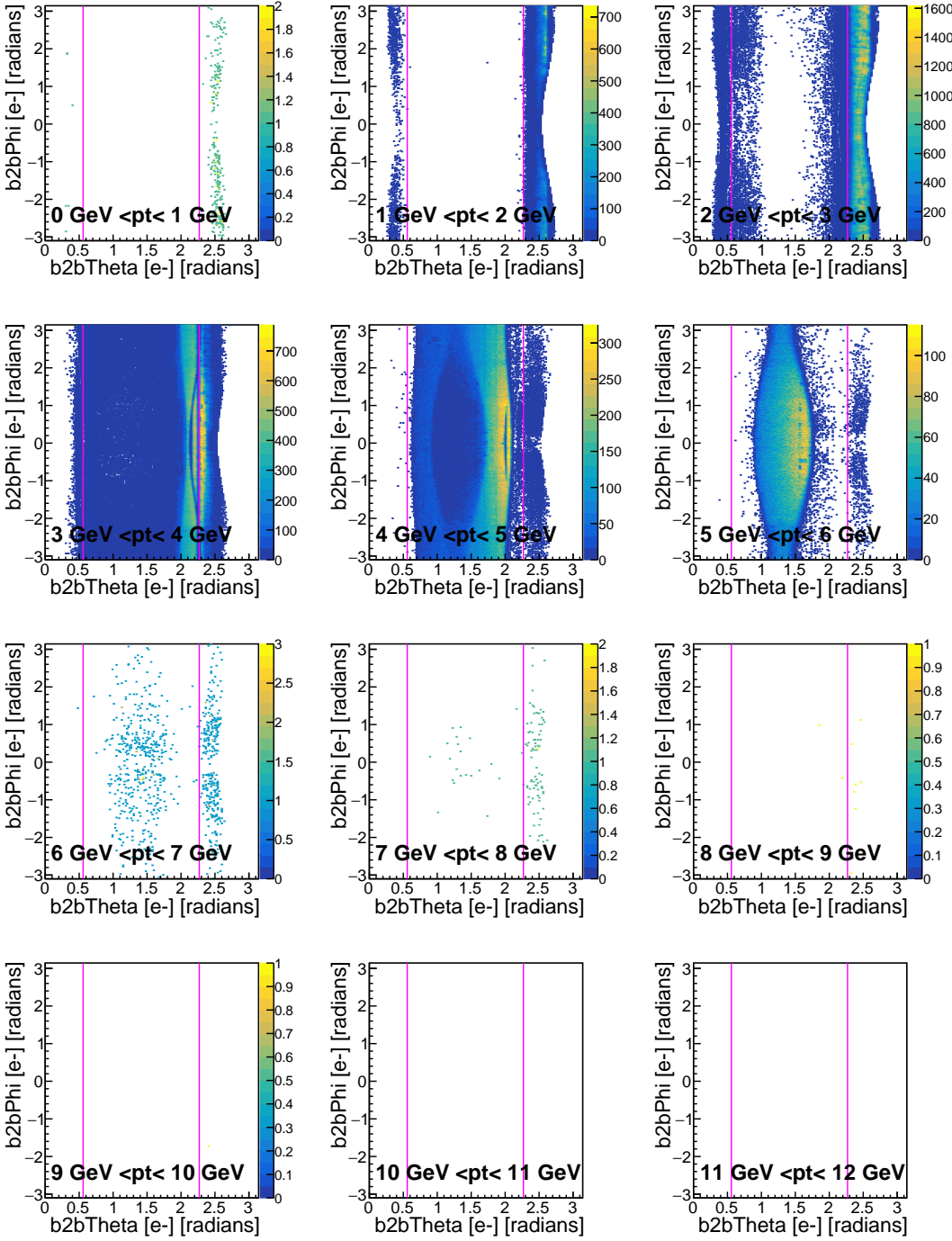


Figure A.14.: Predicted  $\theta$  and  $\phi$  denominator histograms of the *probe* particle for different transverse momenta for positrons for phase2 Data are shown. The different areas of interest are indicated by the pink line.

### A. Additional Preparation Plots

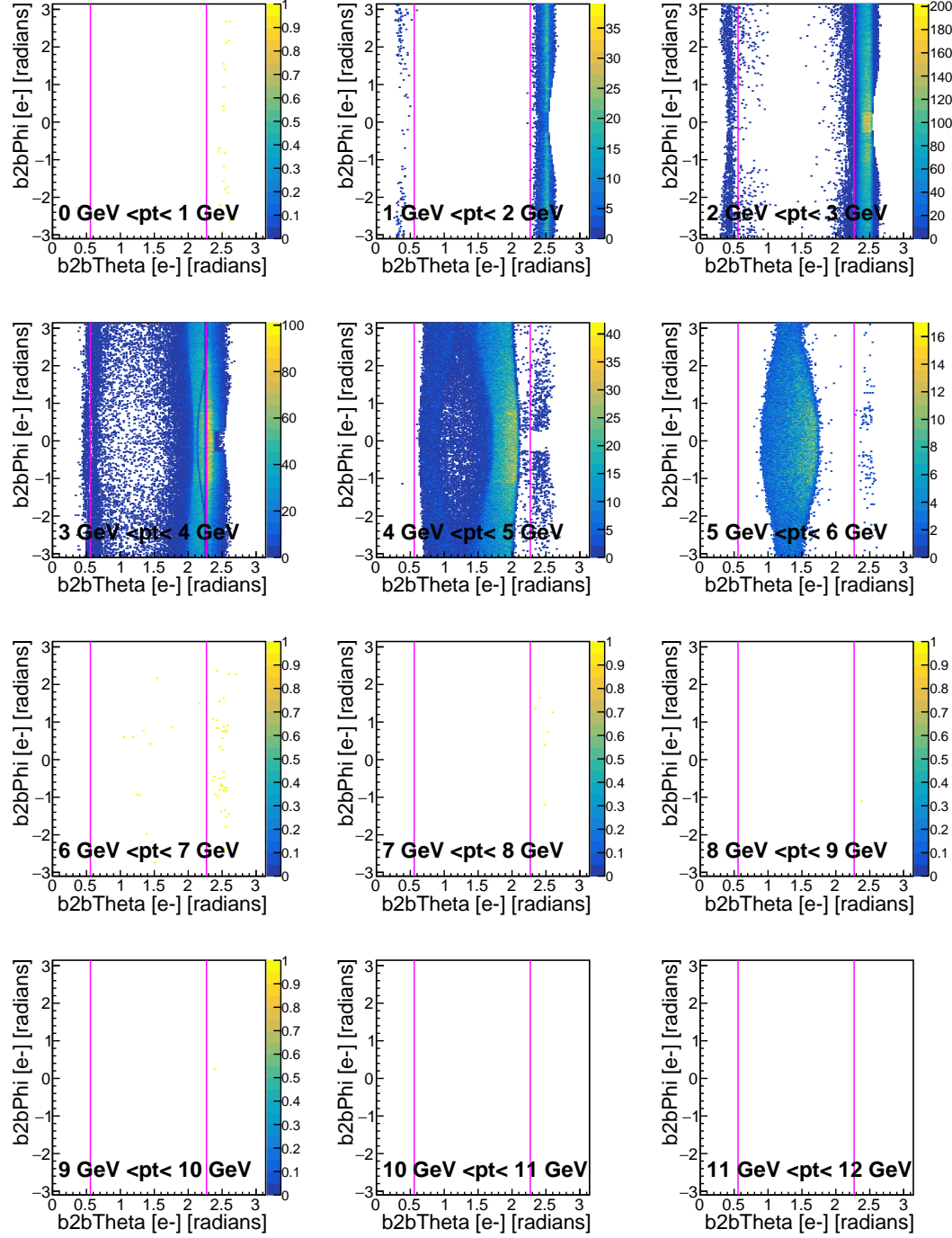


Figure A.15.: Predicted  $\theta$  and  $\phi$  denominator histograms of the *probe* particle for different transverse momenta for positrons for phase2 MC are shown. The different areas of interest are indicated by the pink line.

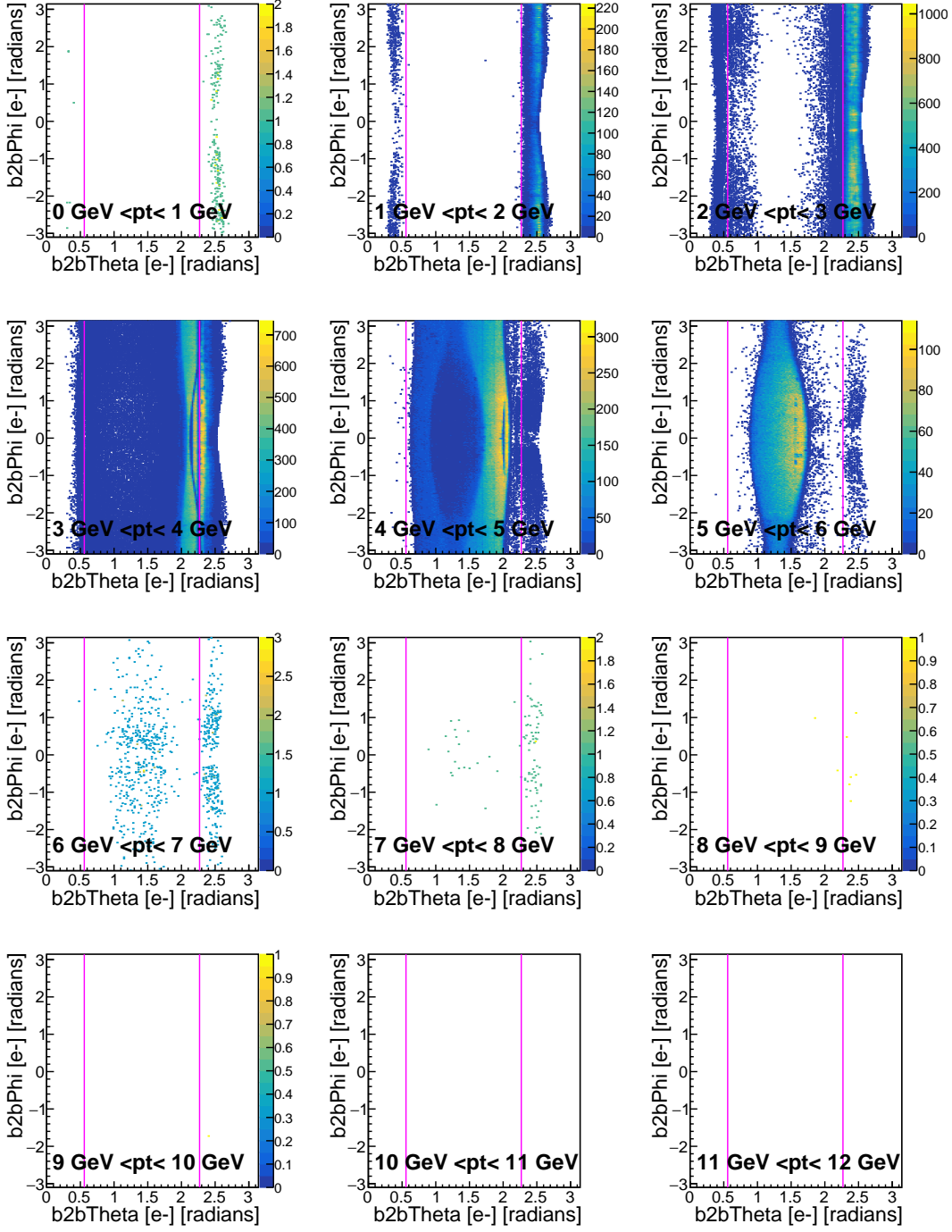


Figure A.16.: Predicted  $\theta$  and  $\phi$  denominator histograms of the *probe* particle for different transverse momenta for positrons for phase2 data are shown. The different areas of interest are indicated by the pink line.



APPENDIX

# B

---

## Additional Phase2 Plots

B. Additional Phase2 Plots

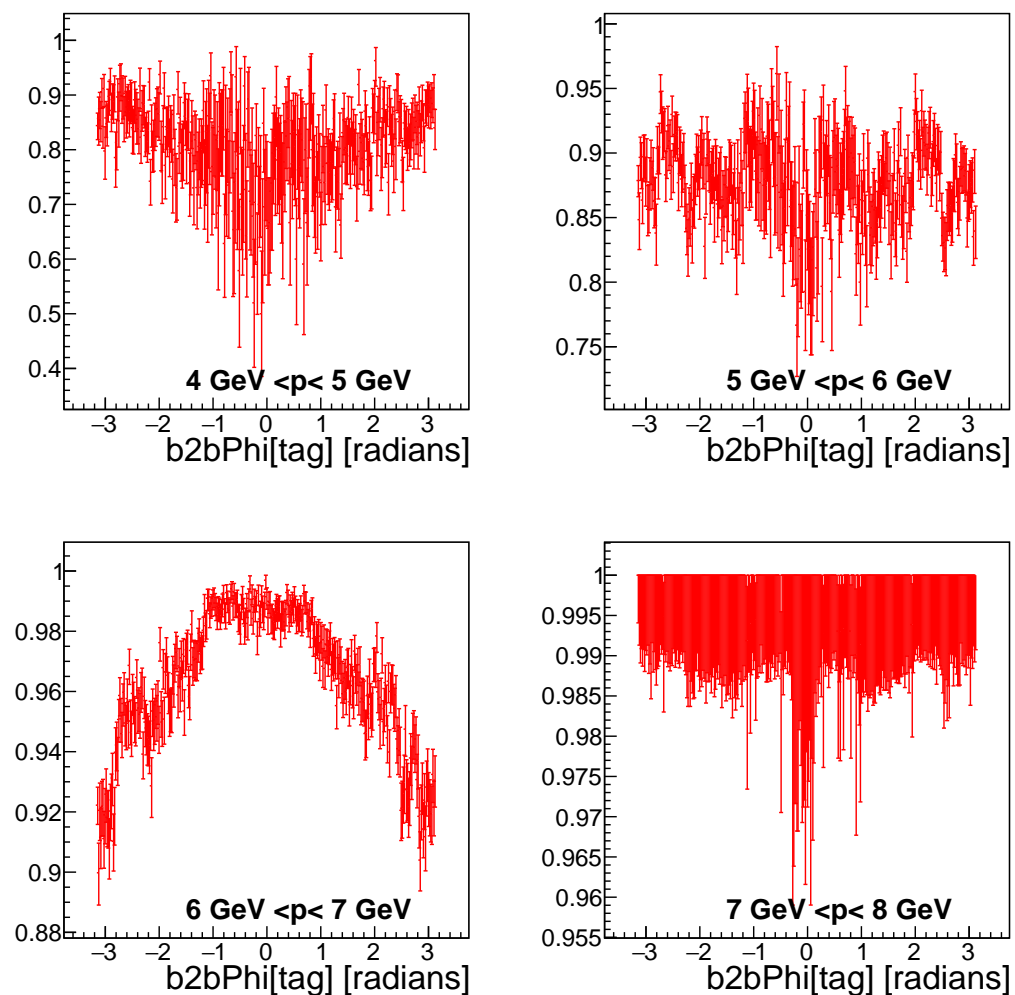


Figure B.1.: Electron  $\phi$  tracking efficiency plots in the forward end cap for phase2 MC.

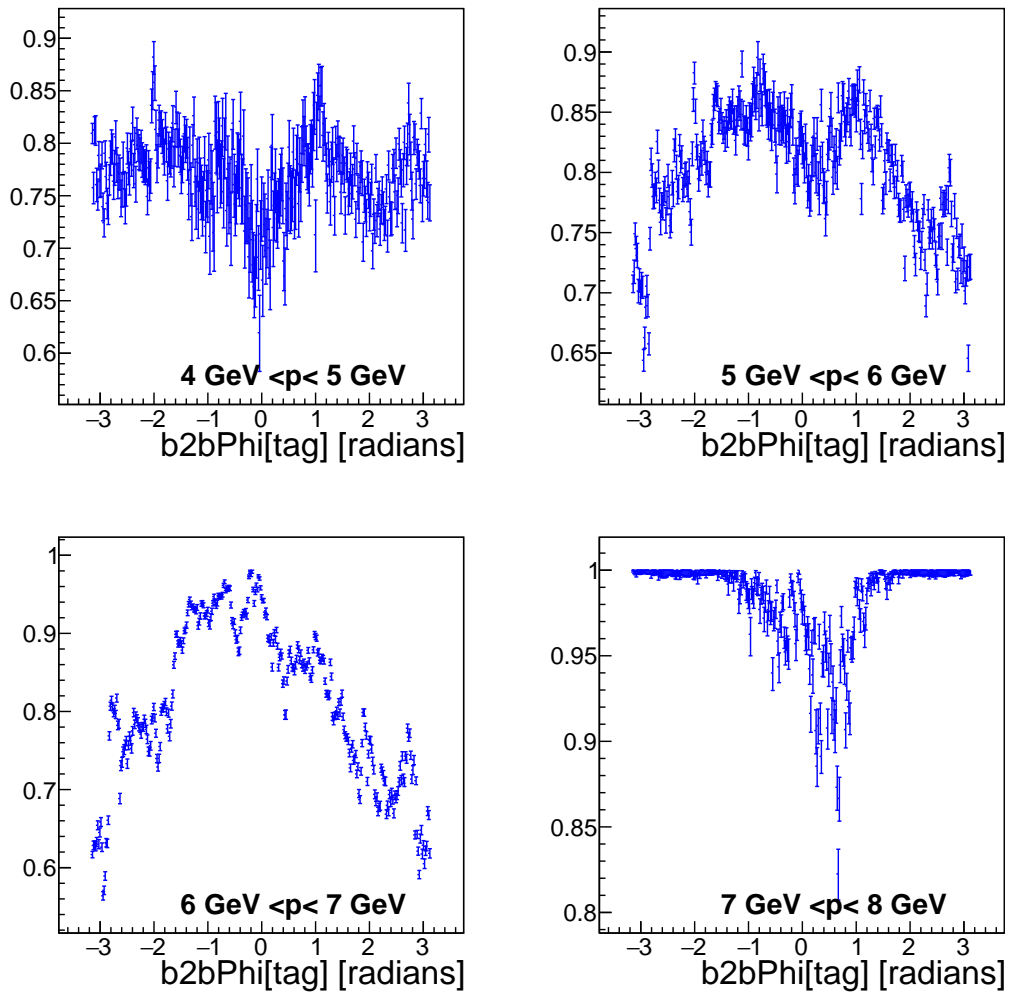


Figure B.2.: Electron  $\phi$  tracking efficiency plots in the forward end cap for phase2 Data.

B. Additional Phase2 Plots

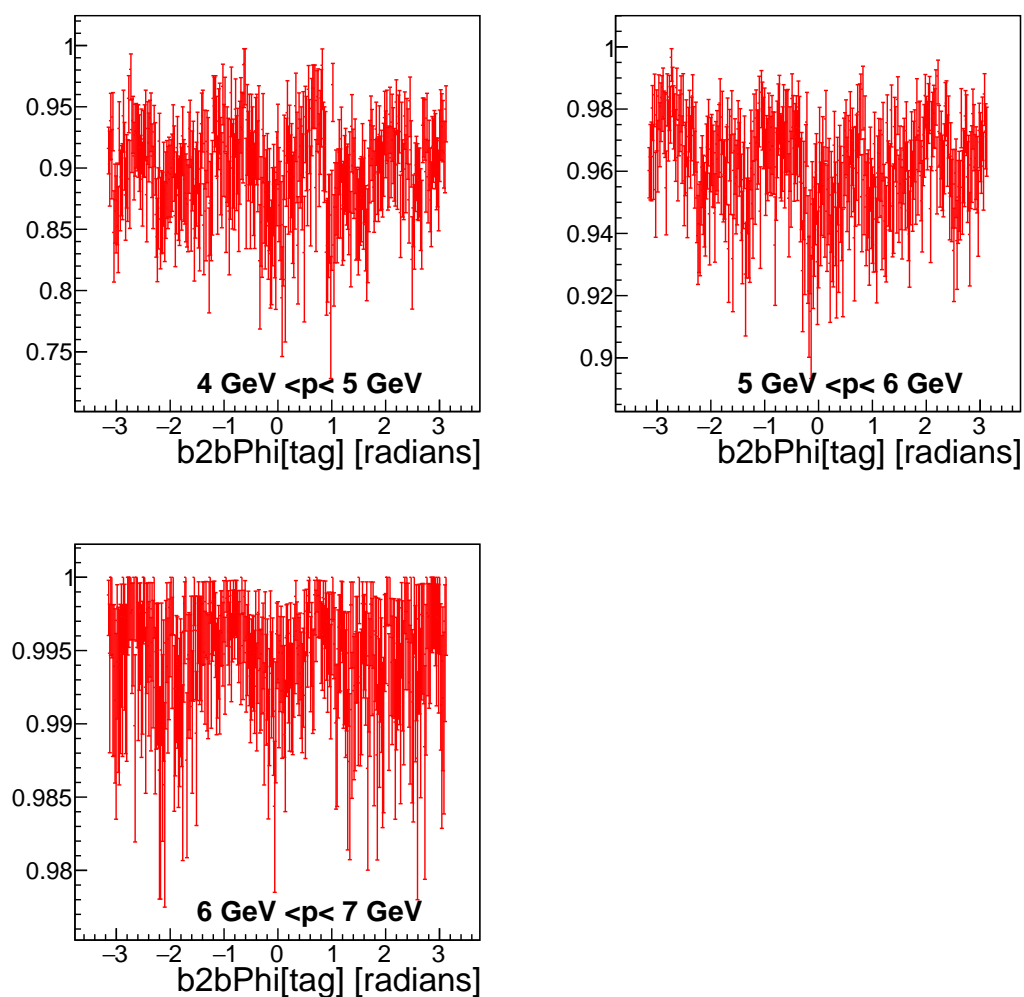


Figure B.3.: Electron  $\phi$  tracking efficiency plots in the barrel for phase2 MC.

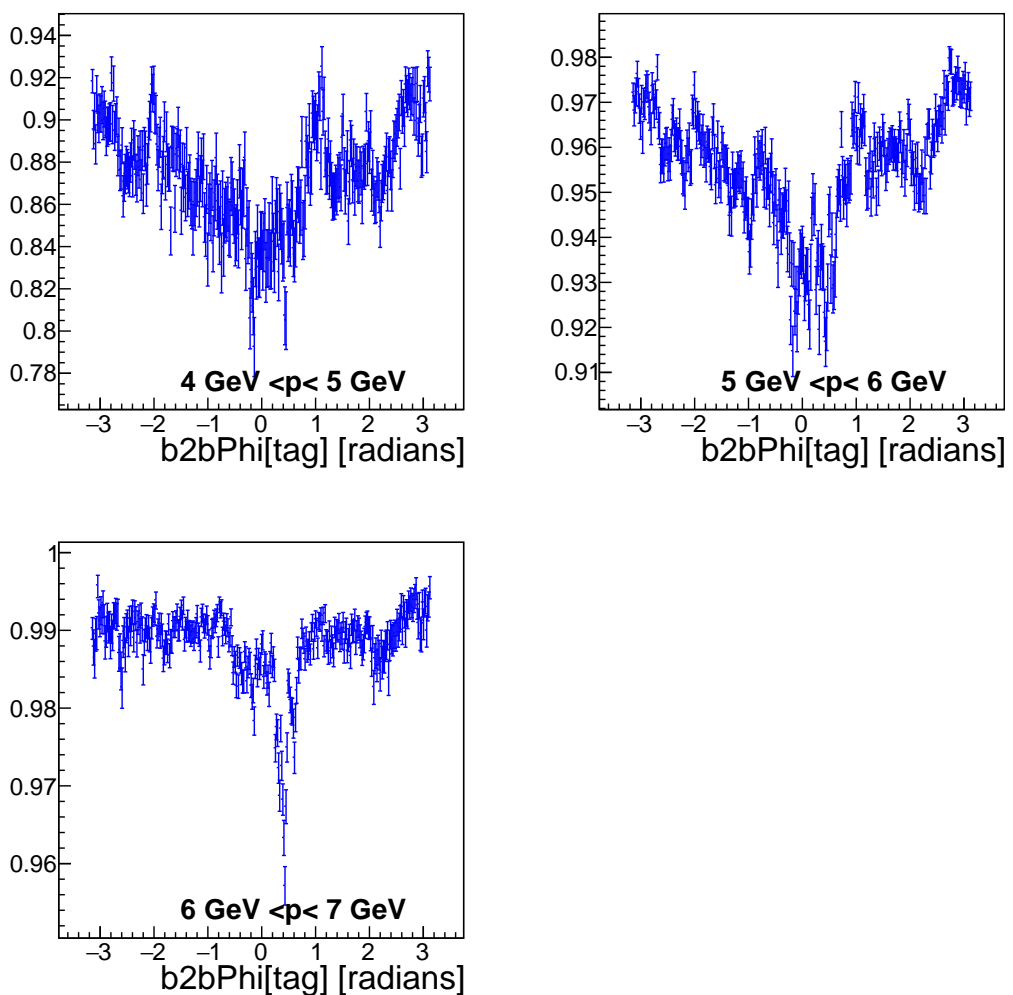


Figure B.4.: Electron  $\phi$  tracking efficiency plots in the barrel for phase2 Data.

B. Additional Phase2 Plots

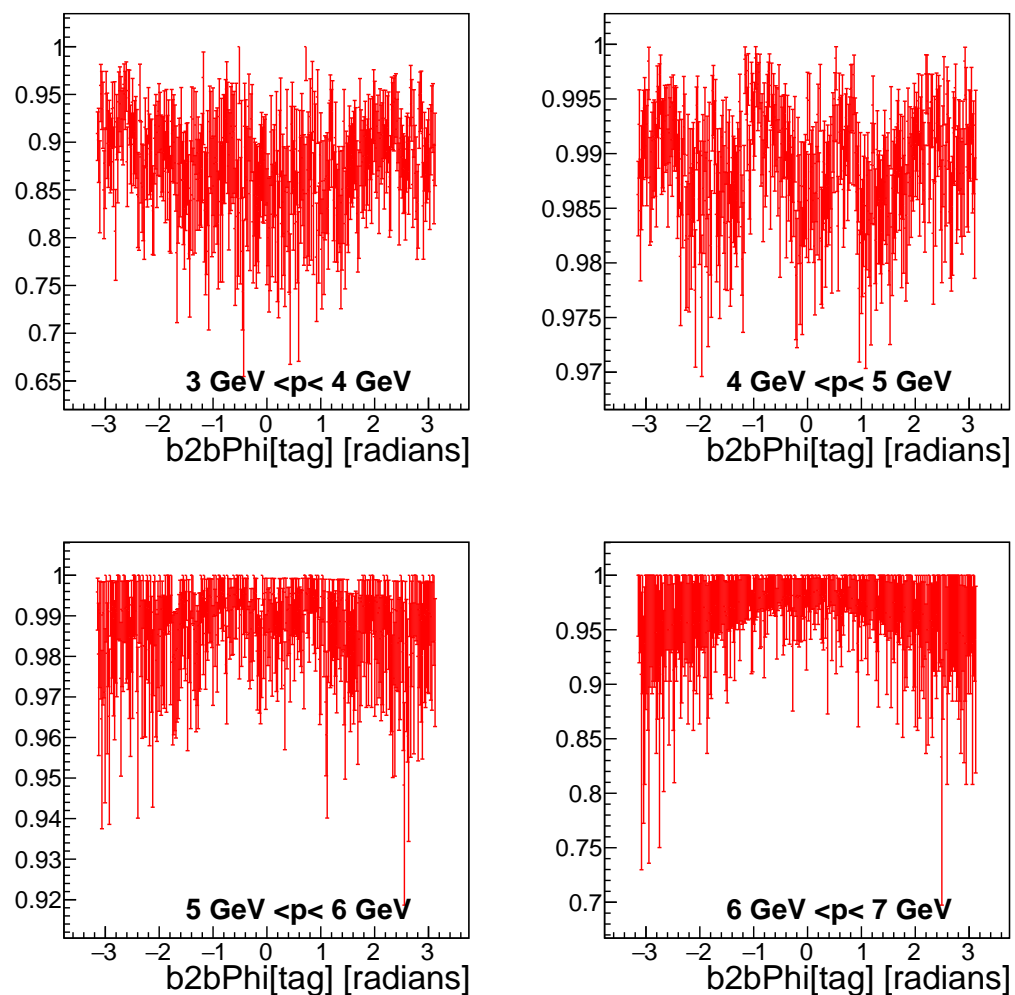


Figure B.5.: Positron  $\phi$  tracking efficiency plots in the barrel for phase2 MC.

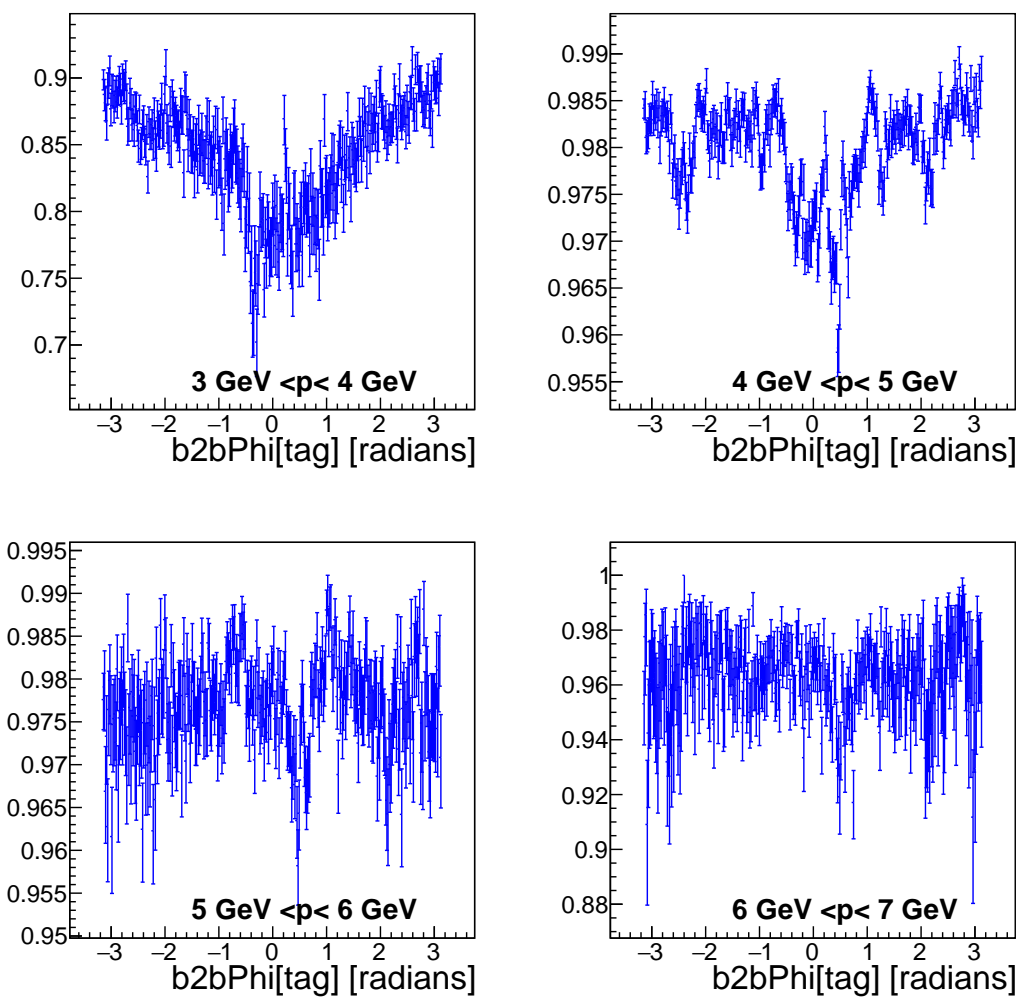


Figure B.6.: Positron  $\phi$  tracking efficiency plots in the barrel for phase2 Data.

B. Additional Phase2 Plots

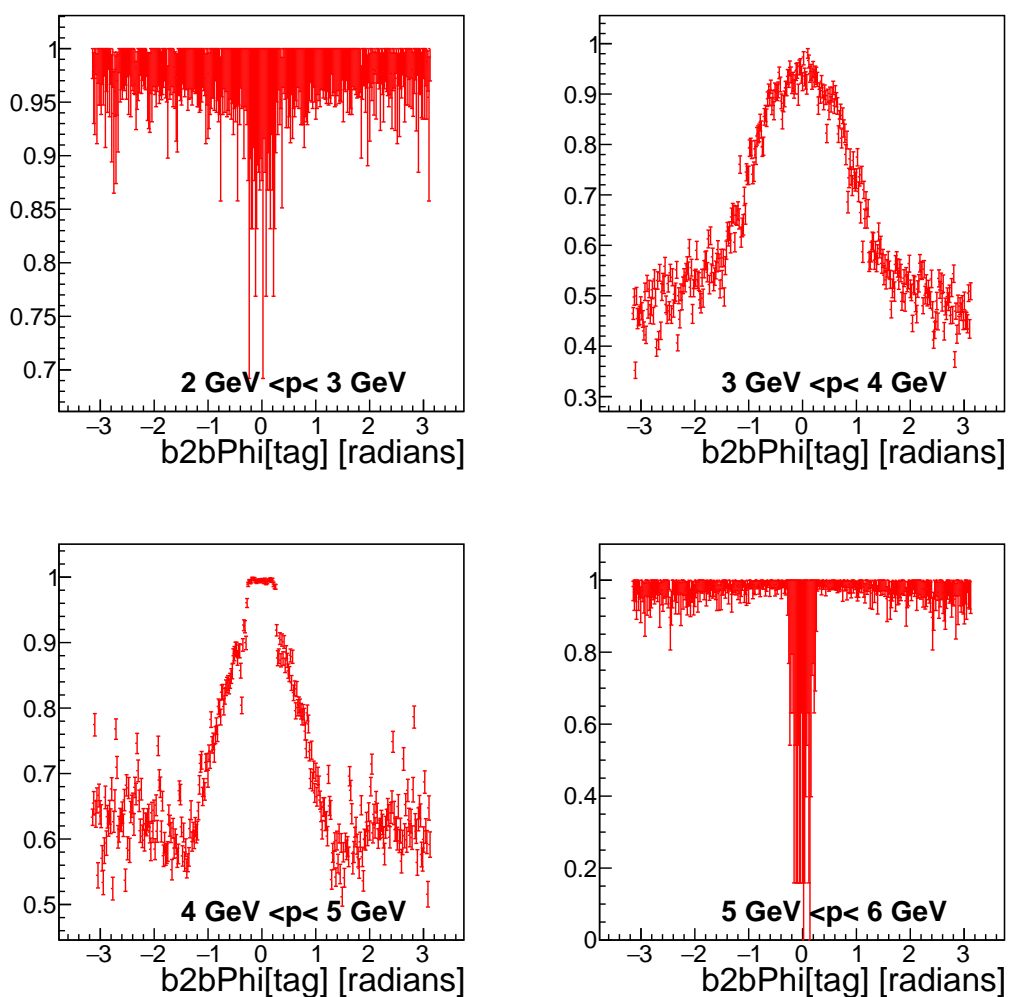


Figure B.7.: Positron  $\phi$  tracking efficiency plots in the backward end cap for phase2 MC.

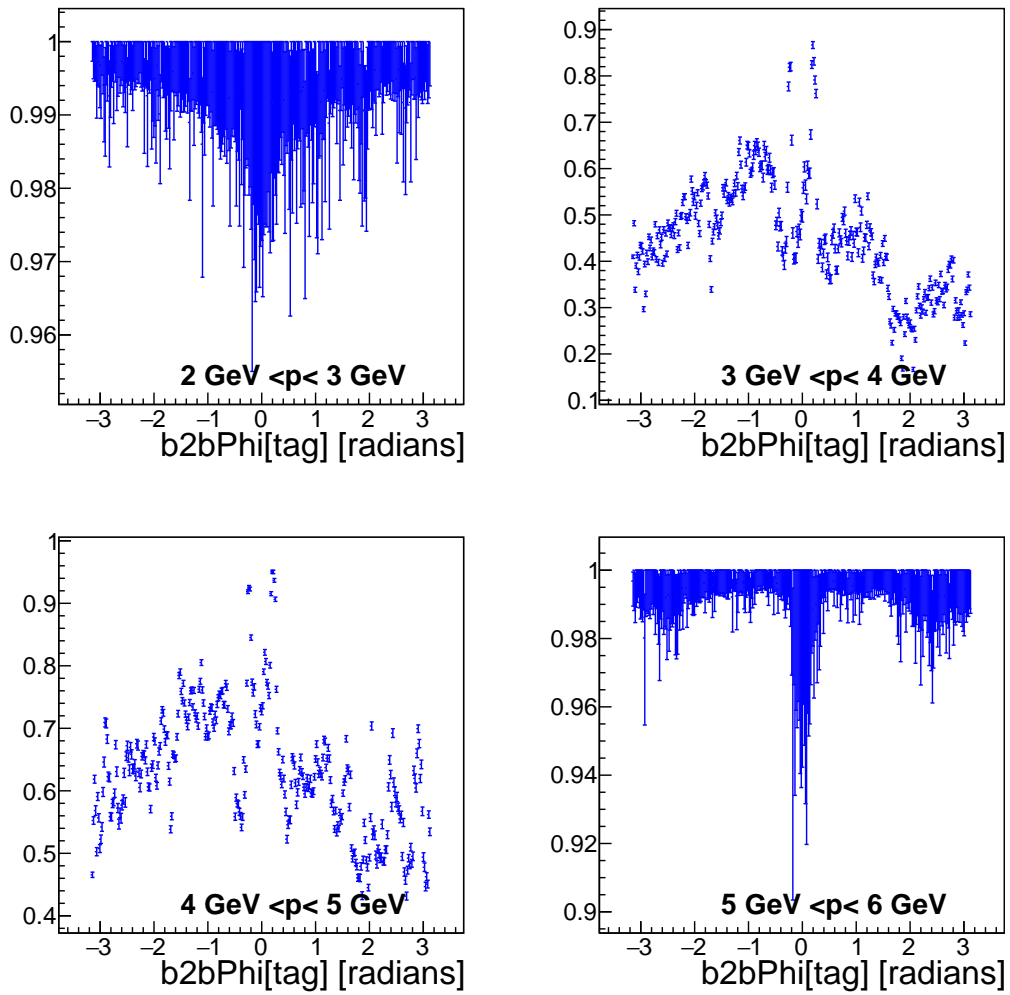


Figure B.8.: Positron  $\phi$  tracking efficiency plots in the backward end cap for phase2 Data.

## B. Additional Phase2 Plots

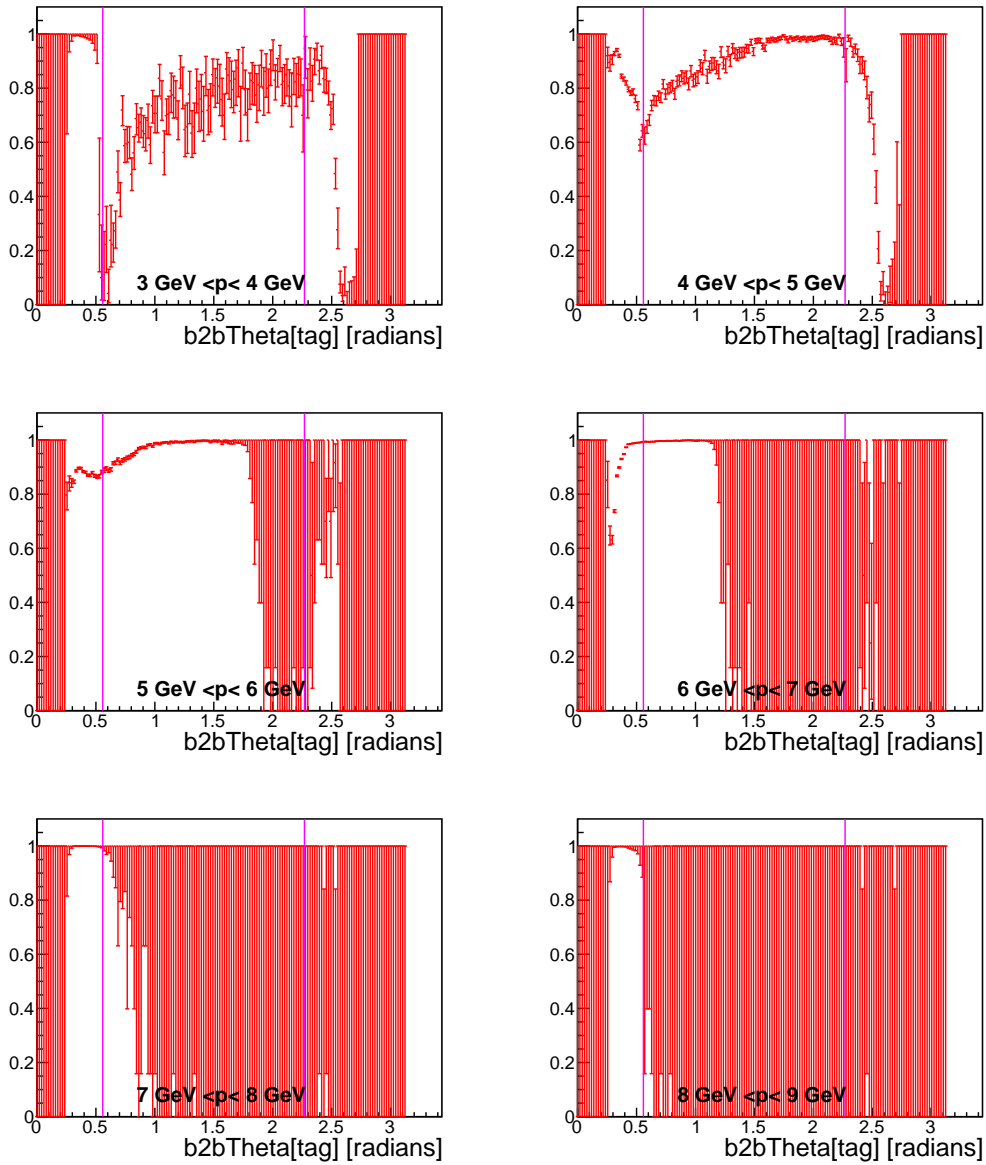


Figure B.9.: Electron  $\phi$  tracking efficiency plots for phase2 MC. The pink line indicates the different sectors of the ECL.

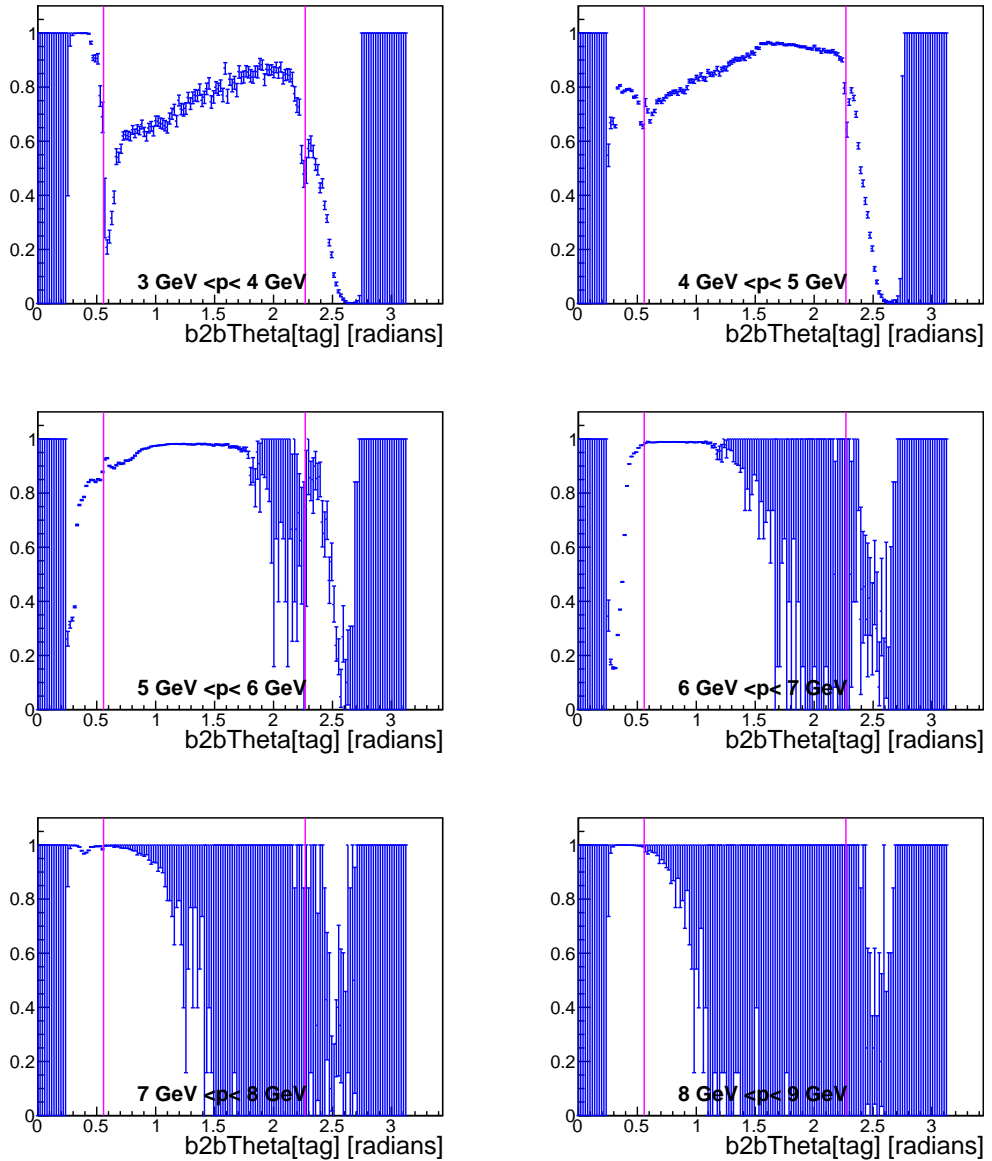


Figure B.10.: Electron  $\phi$  tracking efficiency plots for phase2 Data. The pink line indicates the different sectors of the ECL.

## B. Additional Phase2 Plots

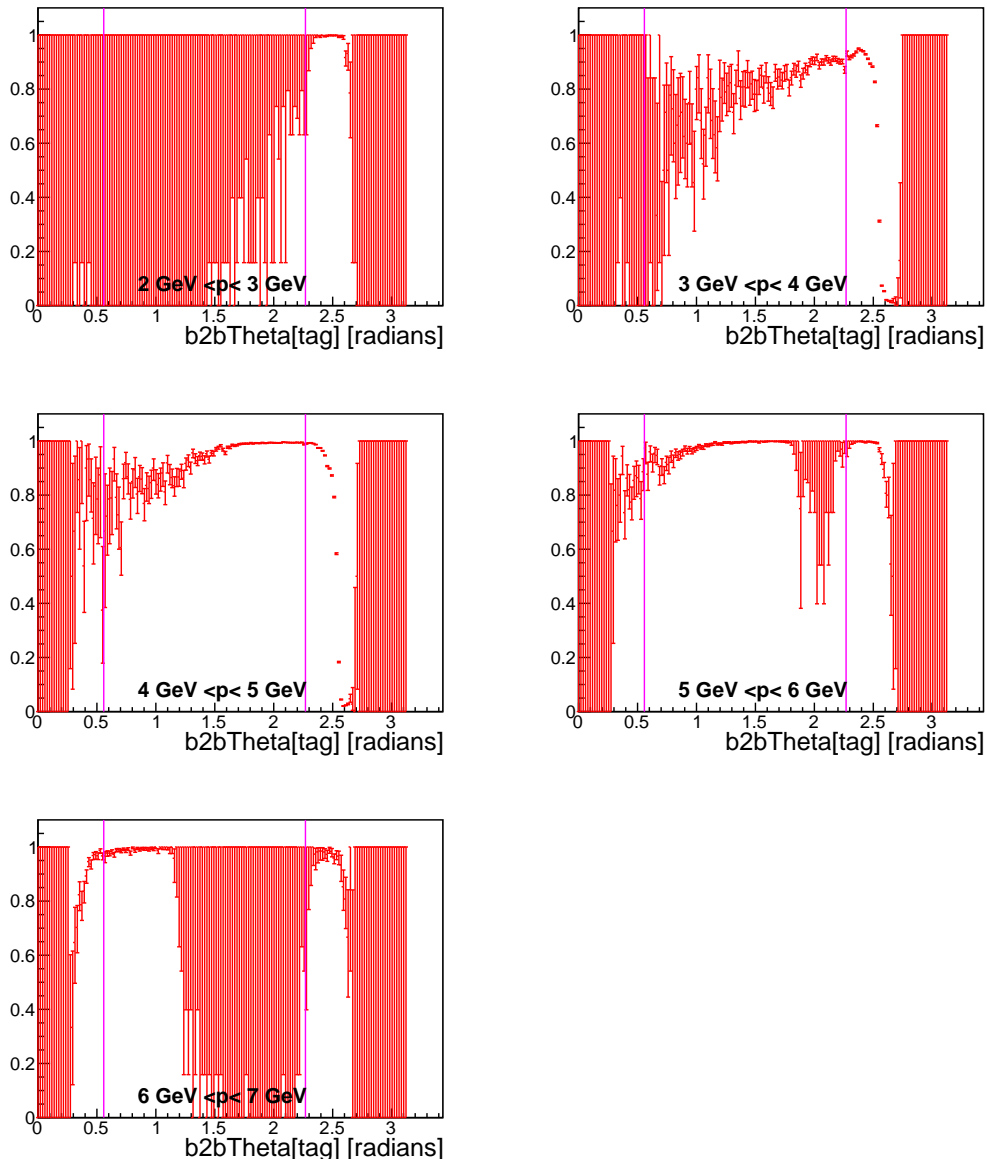


Figure B.11.: Positron  $\phi$  tracking efficiency plots for phase2 MC. The pink line indicates the different sectors of the ECL.

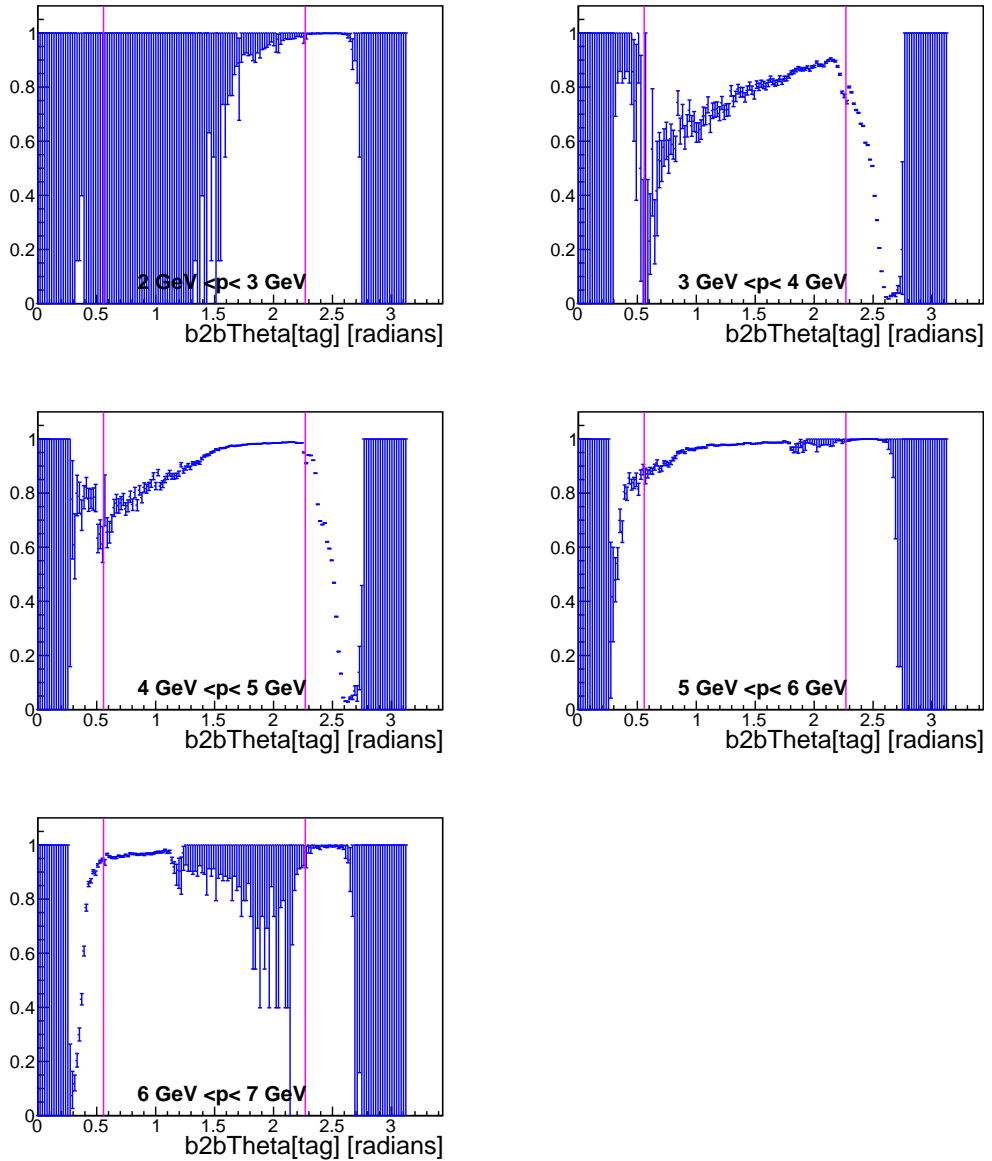


Figure B.12.: Positron  $\phi$  tracking efficiency plots for phase2 Data. The pink line indicates the different sectors of the ECL.

## B. Additional Phase2 Plots

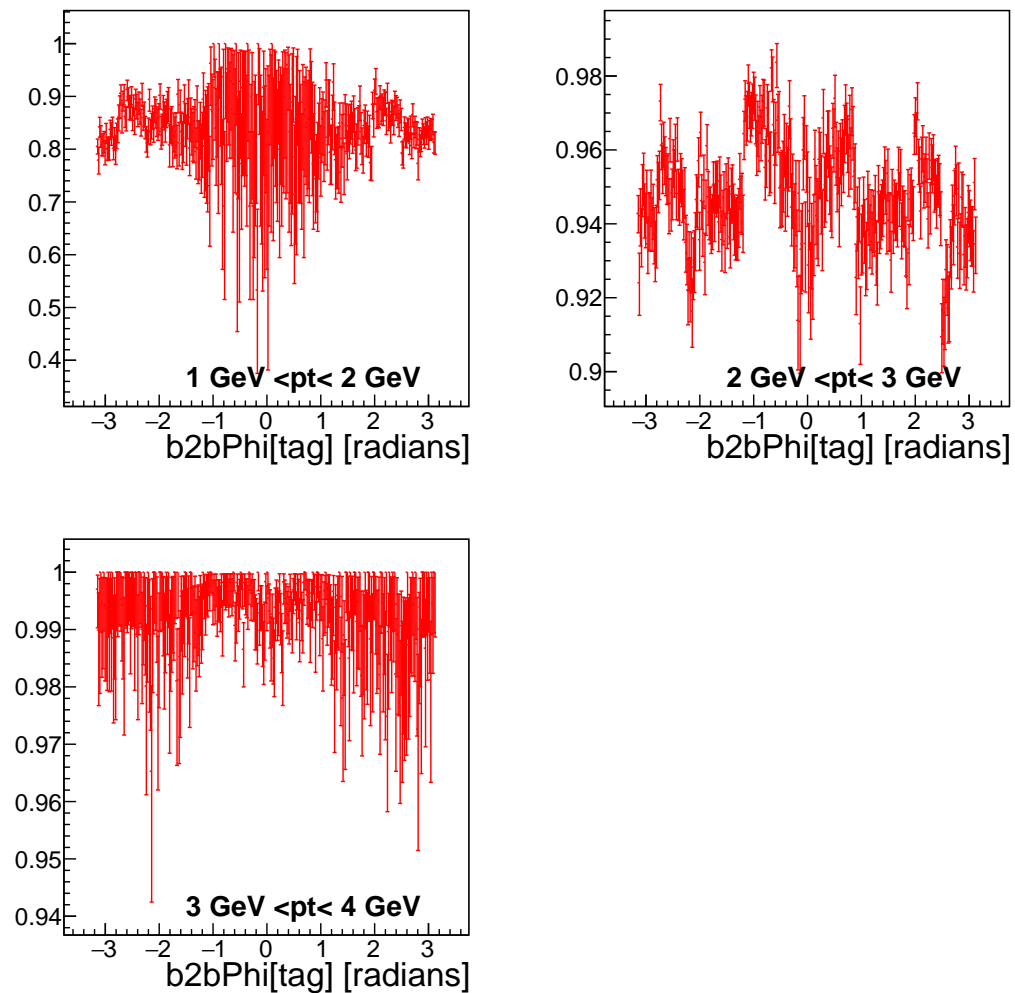


Figure B.13.: Electron  $\phi$  transverse momentum tracking efficiency plots in the forward end cap for phase2 MC.

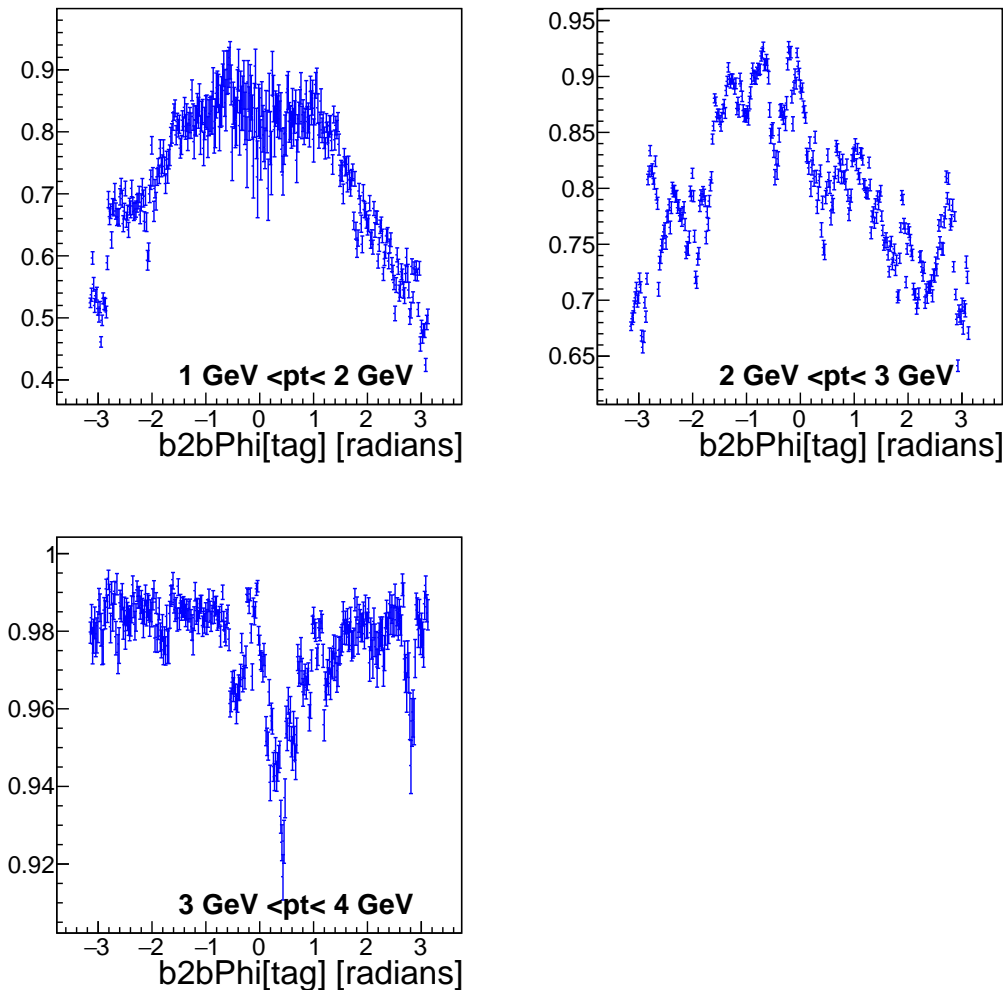


Figure B.14.: Electron  $\phi$  transverse momentum tracking efficiency plots in the forward end cap for phase2 Data.

B. Additional Phase2 Plots

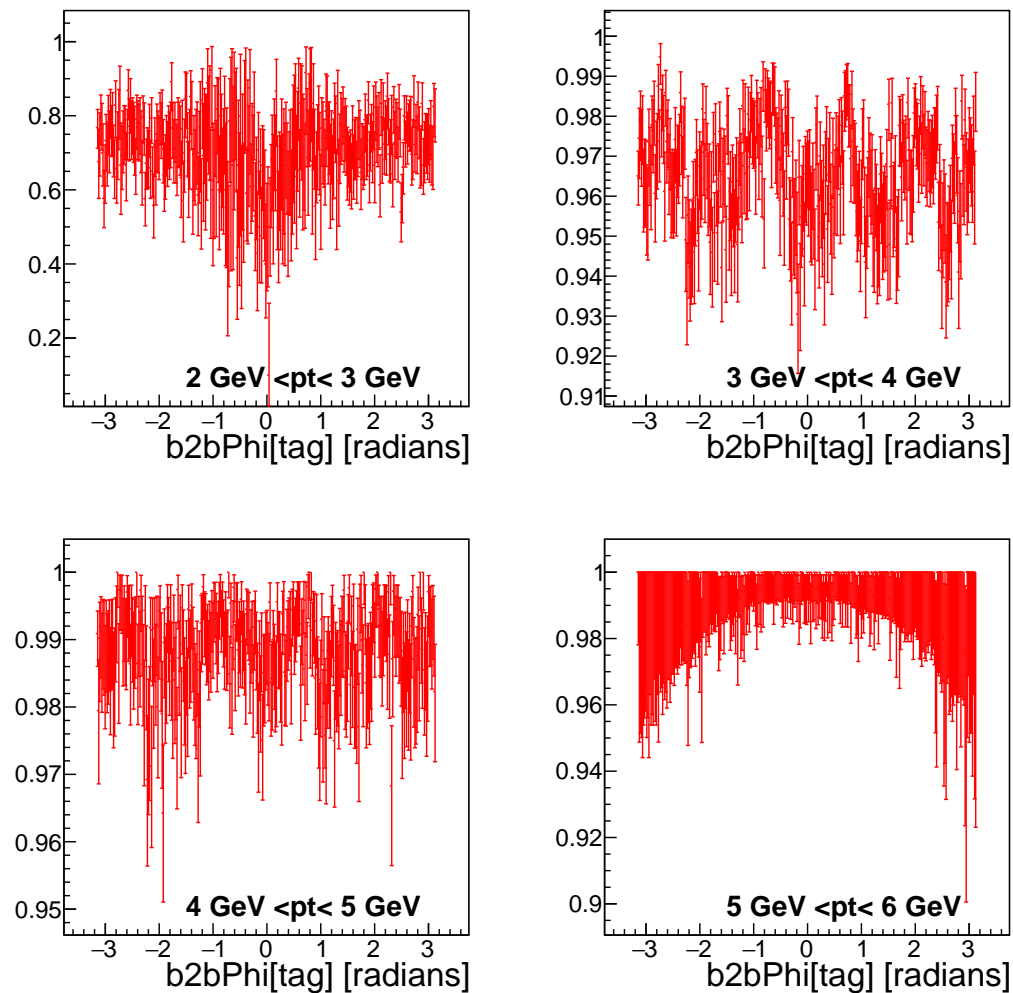


Figure B.15.: Electron  $\phi$  transverse momentum tracking efficiency plots in the barrel for phase2 MC.

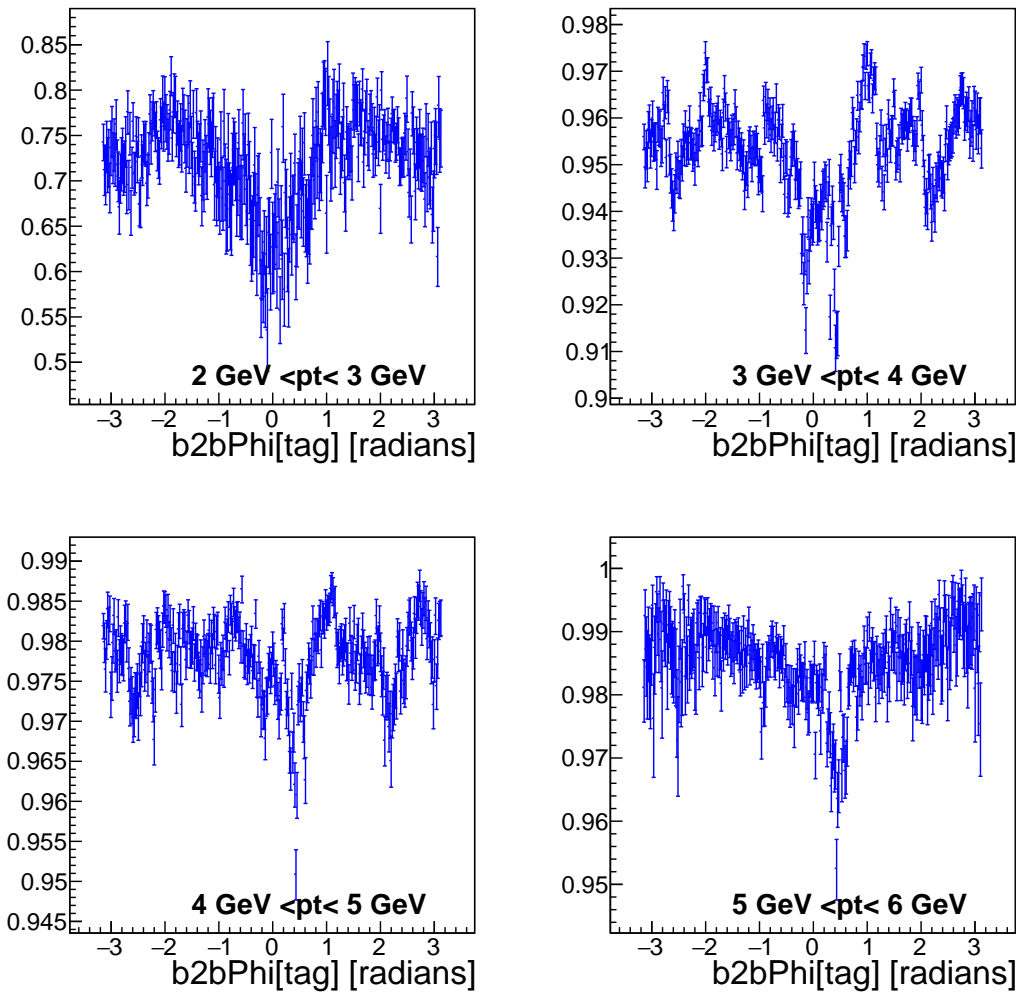


Figure B.16.: Electron  $\phi$  transverse momentum tracking efficiency plots in the barrel for phase2 Data.

## B. Additional Phase2 Plots

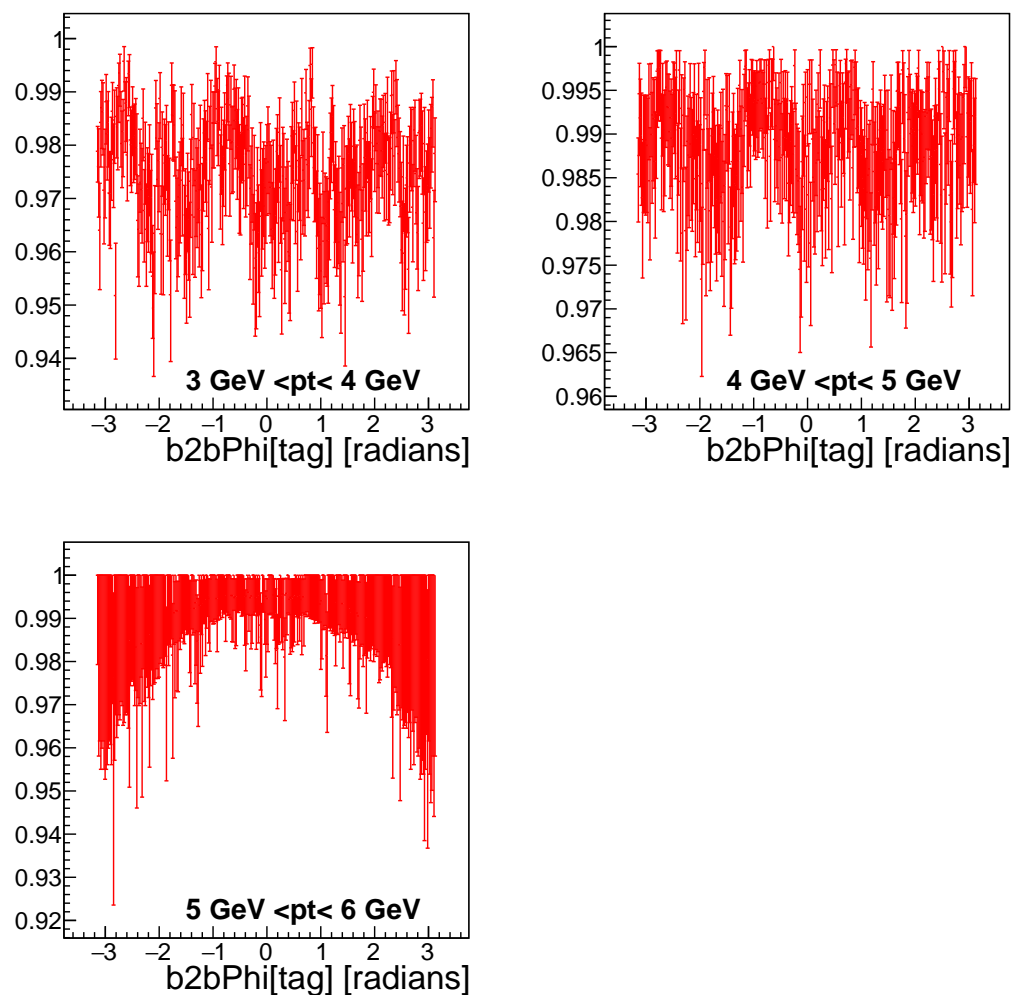


Figure B.17.: Positron  $\phi$  transverse momentum tracking efficiency plots in the barrel for phase2 MC.

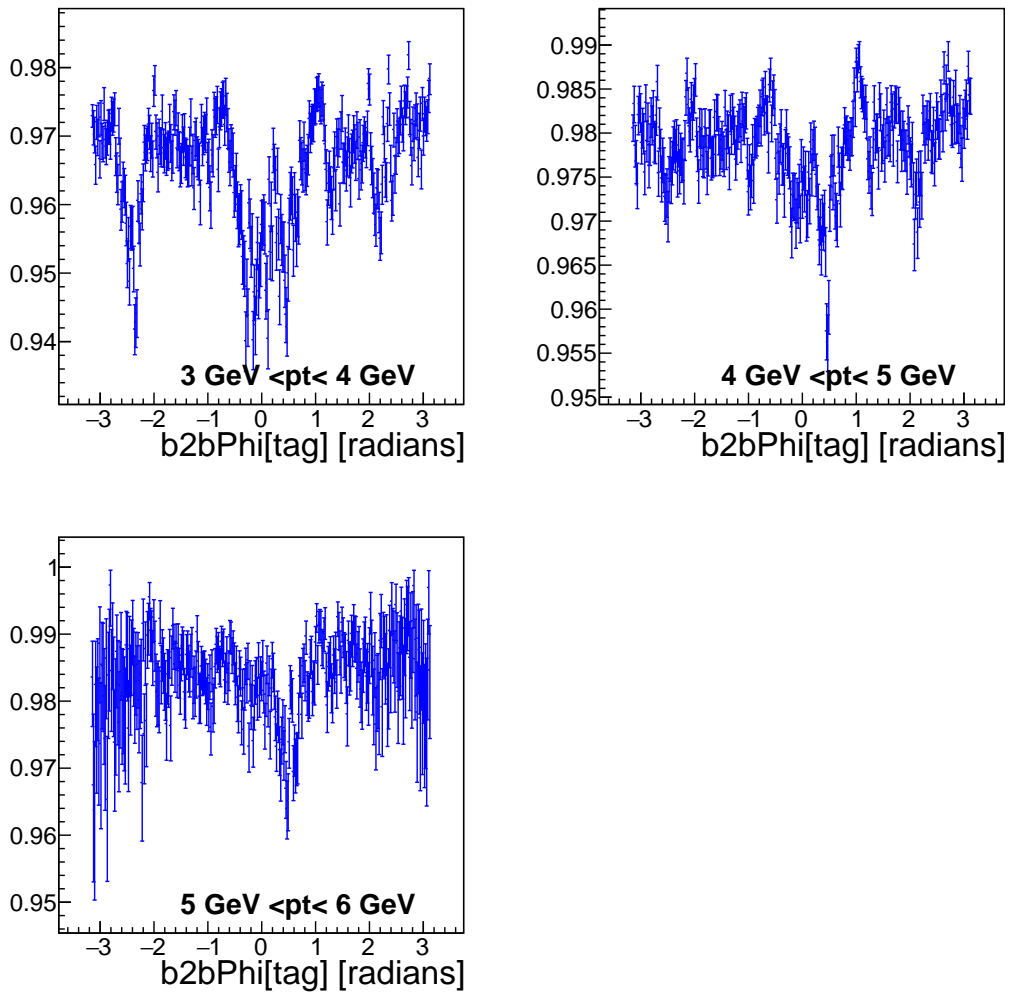


Figure B.18.: Positron  $\phi$  transverse momentum tracking efficiency plots in the barrel for phase2 Data.

B. Additional Phase2 Plots

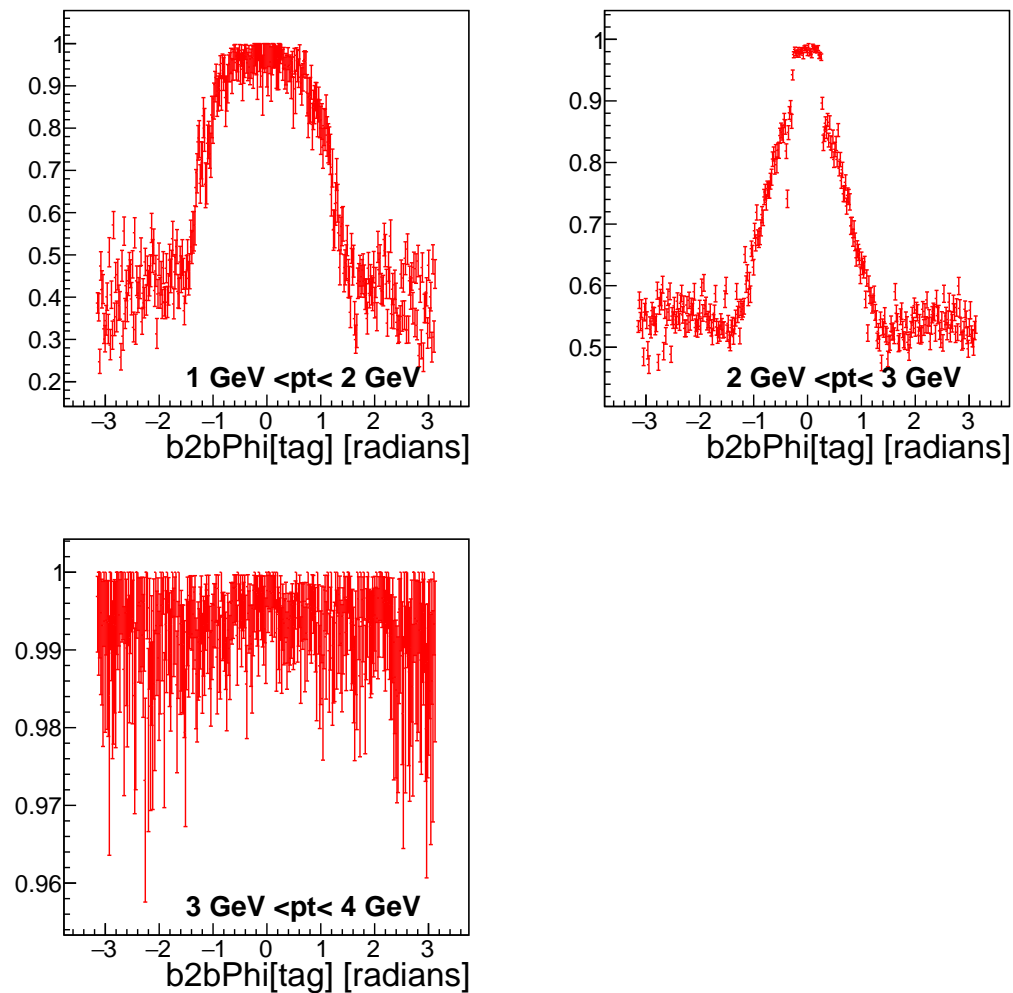


Figure B.19.: Positron  $\phi$  transverse momentum tracking efficiency plots in the backward end cap for phase2 MC.

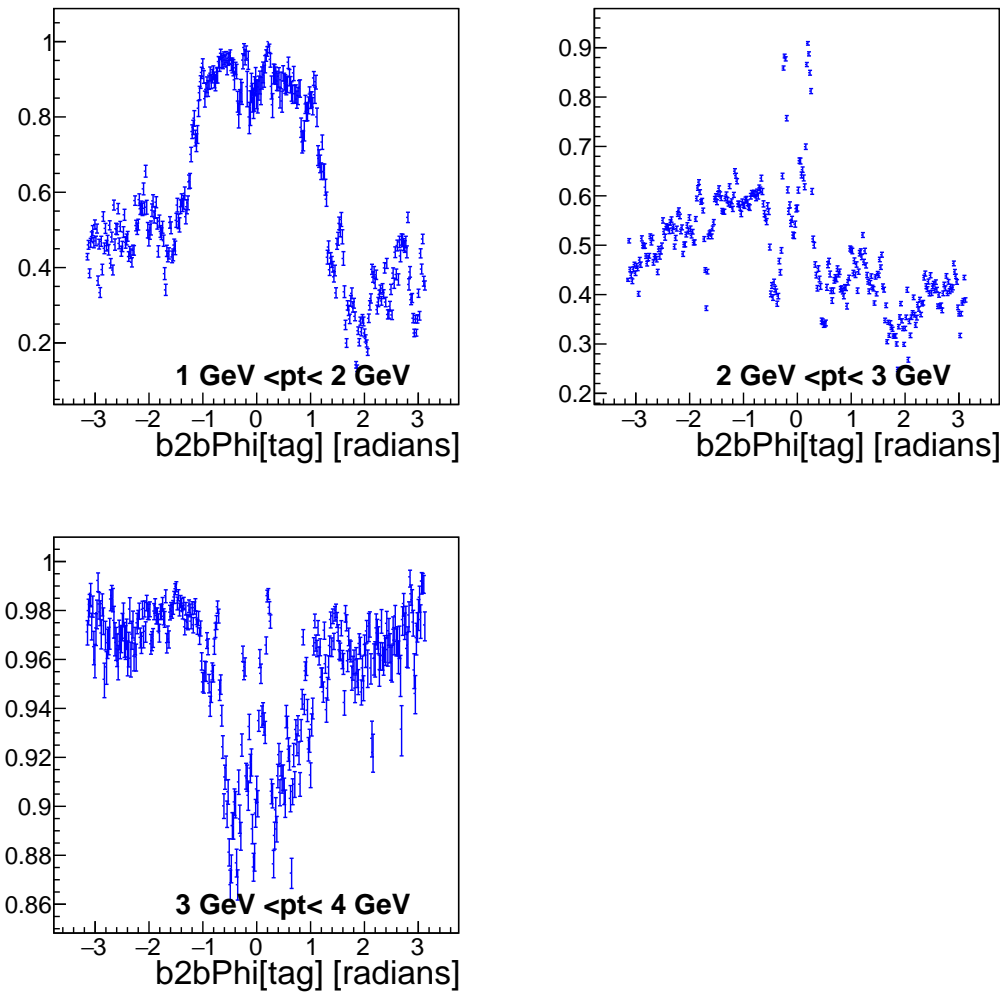


Figure B.20.: Positron  $\phi$  transverse momentum tracking efficiency plots in the backward end cap for phase2 Data.

## B. Additional Phase2 Plots

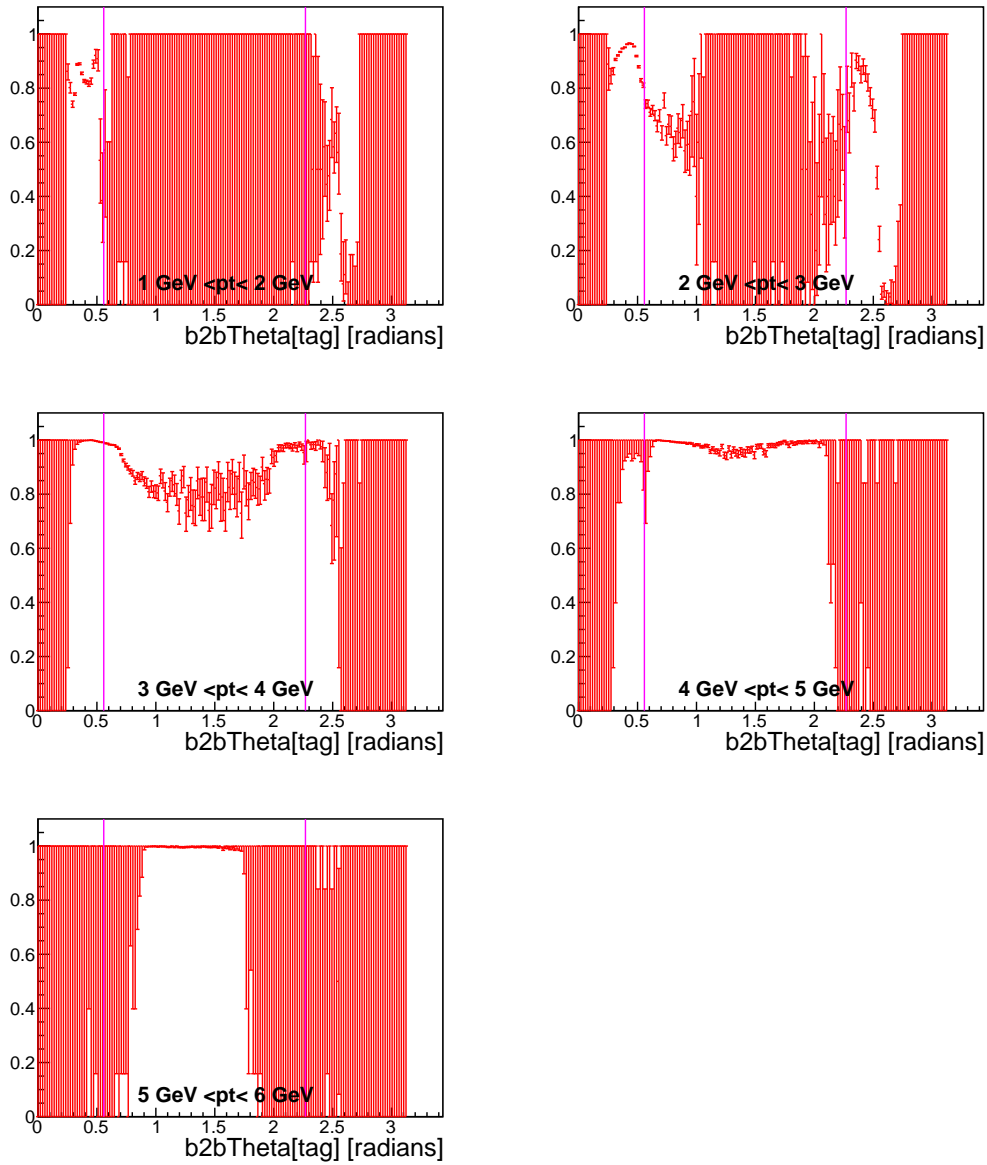


Figure B.21.: Electron  $\phi$  transverse momentum tracking efficiency plots for phase2 MC. The pink line indicates the different sectors of the ECL.

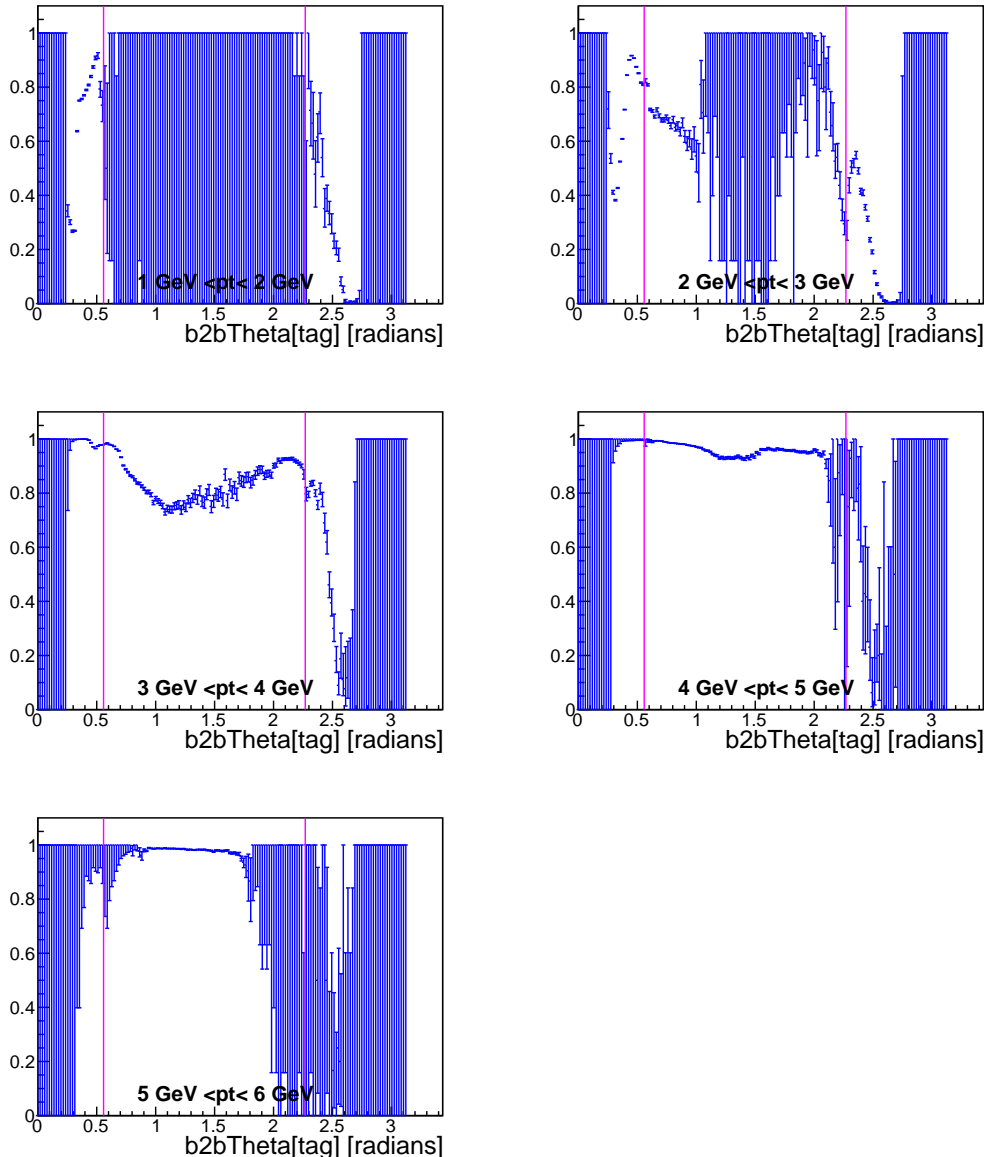


Figure B.22.: Electron  $\phi$  transverse momentum tracking efficiency plots for phase2 Data. The pink line indicates the different sectors of the ECL.

## B. Additional Phase2 Plots

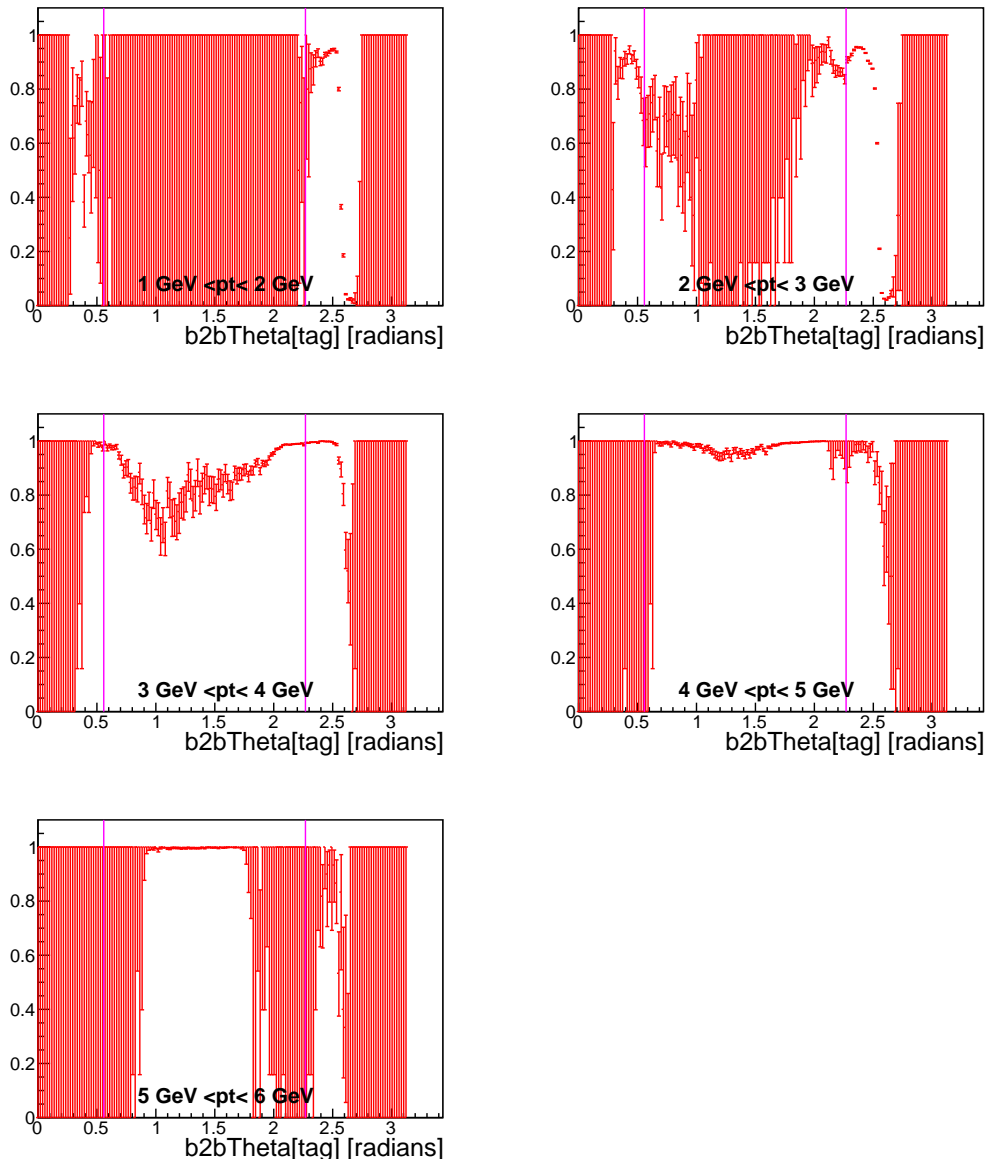


Figure B.23.: Positron  $\phi$  transverse momentum tracking efficiency plots for phase2 MC. The pink line indicates the different sectors of the ECL.

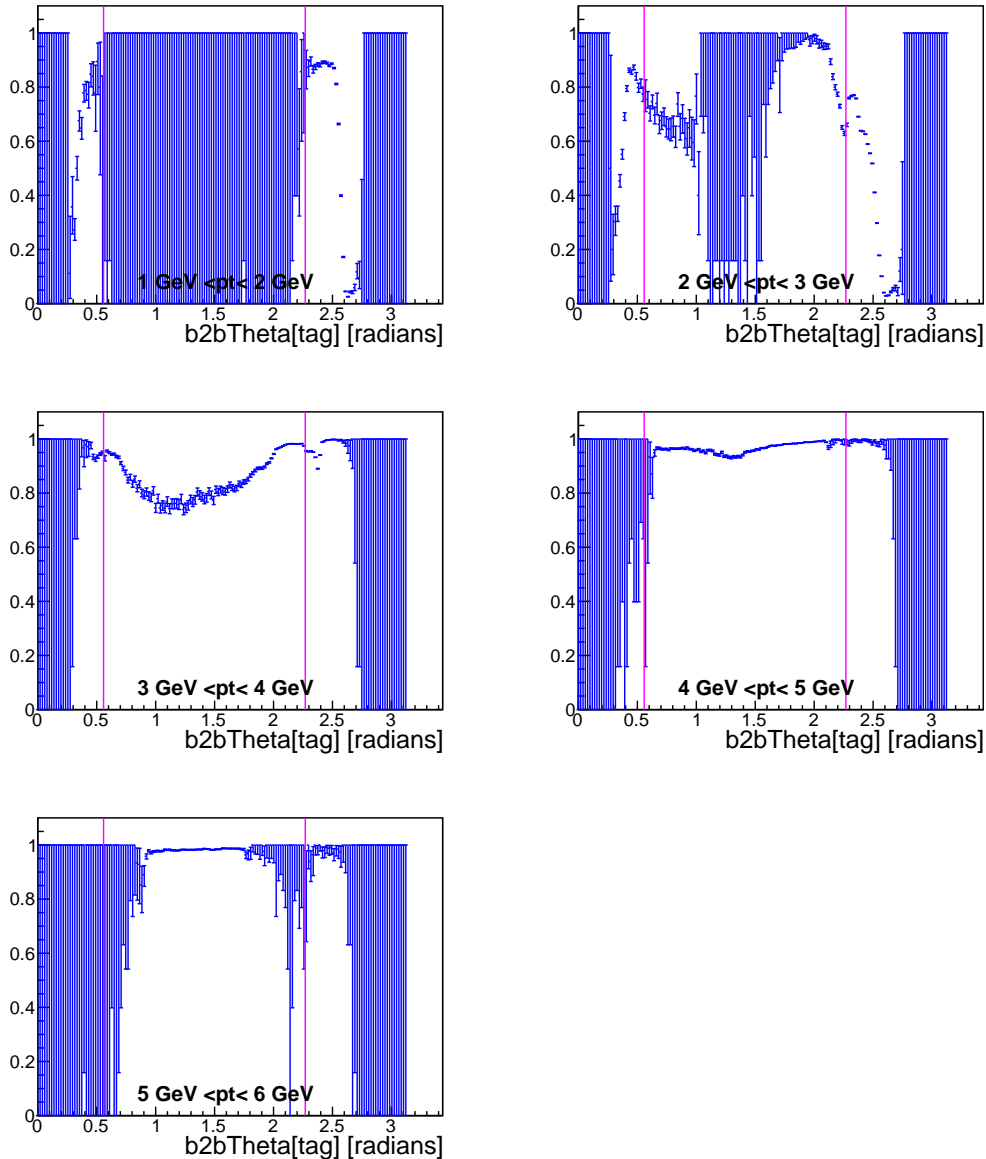


Figure B.24.: Positron transverse momentum  $\phi$  tracking efficiency plots for phase2 Data. The pink line indicates the different sectors of the ECL.



---

## List of Figures

2.1.	Standard Model . . . . .	4
2.2.	Bhabha Feynman Diagrams . . . . .	6
2.3.	Differential Cross Section For Electrons And Positrons In Bhabha Events	7
2.4.	Differential Cross Section For Bhabha Events . . . . .	7
2.5.	$\theta$ -Momentum-Distribution In The CMS And LAB Frame . . . . .	8
2.6.	$\theta$ -Transverse Momentum-Distribution In The CMS And LAB Frame . . . . .	8
2.7.	Energies Of The Outgoing Particle In The LAB Frame . . . . .	9
3.1.	SuperKEKB Collider . . . . .	12
3.2.	Sketch Of The Beam Crossing For KEKB And SuperKEKB . . . . .	13
3.3.	Belle II Detector . . . . .	14
3.4.	Coordinate System Of Belle II . . . . .	15
3.5.	Vertex Detector . . . . .	16
3.6.	Pixel Detector . . . . .	17
3.7.	DePFET . . . . .	17
3.8.	Silicon Vertex Detector . . . . .	19
3.9.	Central Drift Chamber . . . . .	19
3.10.	TOP Principle . . . . .	20
3.11.	ARICH . . . . .	21
4.1.	Schematic Overview Of The Trigger System . . . . .	26
4.2.	Working Principle of the DAQ . . . . .	27
6.1.	Number Of Candidates And Invariant Mass (No Cuts) . . . . .	35
6.2.	Number Of Candidates And Invariant Mass ( $M > 8 \text{ GeV}$ ) . . . . .	35
6.3.	Cluster Splitting Energy Distribution . . . . .	37
6.4.	Number Of Candidates Per Event (All Cuts) . . . . .	38
6.5.	Number Of Candidates Per Event With No MC-Truth Info (All Cuts)	40
6.6.	Number Of Candidates Per Event for Beamtime-Data (All Cuts) . . . . .	40
6.7.	Sketch Of The <code>b2bClusterPhi</code> Variable . . . . .	41
6.8.	<code>b2bClusterPhi</code> - <code>clusterPhi</code> For Beamtime-Data . . . . .	42
6.9.	<code>b2bClusterPhi</code> - <code>clusterPhi</code> For MC . . . . .	43
6.10.	<code>bhabha</code> Trigger Signal After Selection . . . . .	44

## List of Figures

6.11. Total Number Of Events After The Selection . . . . .	46
6.12. Denominator $\theta\phi$ Electron Momentum MC . . . . .	48
6.13. Denominator $\theta\phi$ Positron Momentum MC . . . . .	49
6.14. Denominator $\theta\phi$ Electron Transverse Momentum MC . . . . .	50
6.15. Denominator $\theta\phi$ Positron Transverse Momentum MC . . . . .	51
7.1. Momentum $\phi$ Electron Forward End Cap Efficiency Phase2 . . . . .	54
7.2. Momentum $\phi$ Electron Barrel Efficiency Phase2 . . . . .	56
7.3. Momentum $\phi$ Positron Barrel Efficiency Phase2 . . . . .	57
7.4. Momentum $\phi$ Positron Backward End Cap Efficiency Phase2 . . . . .	59
7.5. Momentum $\theta$ Electron Efficiency Phase2 . . . . .	62
7.6. Momentum $\theta$ Positron Efficiency Phase2 . . . . .	63
7.7. Transverse Momentum $\phi$ Electron Forward End Cap Efficiency Phase2	64
7.8. Transverse Momentum $\phi$ Electron Barrel Efficiency Phase2 . . . . .	65
7.9. Transverse Momentum $\phi$ Positron Barrel Efficiency Phase2 . . . . .	66
7.10. Transverse Momentum $\phi$ Positron backward end cap Efficiency Phase2	67
7.11. Transverse Momentum $\theta$ Electron Efficiency Phase2 . . . . .	68
7.12. Transverse Momentum $\theta$ Positron Efficiency Phase2 . . . . .	69
A.1. clusterE(HclE) - clusterE(LclE) . . . . .	75
A.2. Cluster Splitting Angle Distribution . . . . .	76
A.3. b2bClusterPhi - clusterPhi For Data (Whole Range) . . . . .	76
A.4. b2bClusterPhi - clusterPhi For MC (Whole Range) . . . . .	77
A.5. Denominator $\theta\phi$ Electron Momentum Phase2 Data . . . . .	78
A.6. Enumerator $\theta\phi$ Electron Momentum Phase2 MC . . . . .	79
A.7. Enumerator $\theta\phi$ Electron Momentum Phase2 Data . . . . .	80
A.8. Denominator $\theta\phi$ Positron Momentum Phase2 Data . . . . .	81
A.9. Enumerator $\theta\phi$ Positron Momentum Phase2 MC . . . . .	82
A.10. Enumerator $\theta\phi$ Positron Momentum Phase2 Data . . . . .	83
A.11. Denominator $\theta\phi$ Electron Transverse Momentum Phase2 Data . . . . .	84
A.12. Enumerator $\theta\phi$ Electron Transverse Momentum Phase2 MC . . . . .	85
A.13. Enumerator $\theta\phi$ Electron Transverse Momentum Phase2 Data . . . . .	86
A.14. Denominator $\theta\phi$ Positron Transverse Momentum Phase2 Data . . . . .	87
A.15. Enumerator $\theta\phi$ Positron Transverse Momentum Phase2 MC . . . . .	88
A.16. Enumerator $\theta\phi$ Positron Transverse Momentum Phase2 Data . . . . .	89
B.1. Momentum $\phi$ Electron Forward End Cap Efficiency Phase2 MC . . . . .	92
B.2. Momentum $\phi$ Electron Forward End Cap Efficiency Phase2 Data . . . . .	93
B.3. Momentum $\phi$ Electron Barrel Efficiency Phase2 MC . . . . .	94
B.4. Momentum $\phi$ Electron Barrel Efficiency Phase2 Data . . . . .	95
B.5. Momentum $\phi$ Positron Barrel Efficiency Phase2 MC . . . . .	96
B.6. Momentum $\phi$ Positron Barrel Efficiency Phase2 Data . . . . .	97
B.7. Momentum $\phi$ Positron Backward End Cap Efficiency Phase2 MC . . . . .	98
B.8. Momentum $\phi$ Positron Backward End Cap Efficiency Phase2 Data . . . . .	99

*List of Figures*

B.9. Momentum $\theta$ Electron Efficiency Phase2 MC . . . . .	100
B.10. Momentum $\theta$ Electron Efficiency Phase2 Data . . . . .	101
B.11. Momentum $\theta$ Positron Efficiency Phase2 MC . . . . .	102
B.12. Momentum $\theta$ Positron Efficiency Phase2 Data . . . . .	103
B.13. Transverse Momentum $\phi$ Electron Forward End Cap Efficiency Phase2 MC . . . . .	104
B.14. Transverse Momentum $\phi$ Electron Forward End Cap Efficiency Phase2 Data . . . . .	105
B.15. Transverse Momentum $\phi$ Electron Barrel Efficiency Phase2 MC . . . .	106
B.16. Transverse Momentum $\phi$ Electron Barrel Efficiency Phase2 Data . . .	107
B.17. Transverse Momentum $\phi$ Positron Barrel Efficiency Phase2 MC . . . .	108
B.18. Transverse Momentum $\phi$ Positron Barrel Efficiency Phase2 Data . . .	109
B.19. Transverse Momentum $\phi$ Positron Backward End Cap Efficiency Phase2 MC . . . . .	110
B.20. Transverse Momentum $\phi$ Positron Backward End Cap Efficiency Phase2 Data . . . . .	111
B.21. Transverse Momentum $\theta$ Electron Efficiency Phase2 MC . . . . .	112
B.22. Transverse Momentum $\theta$ Electron Efficiency Phase2 Data . . . . .	113
B.23. Transverse Momentum $\theta$ Positron Efficiency Phase2 MC . . . . .	114
B.24. Transverse Momentum $\theta$ Positron Efficiency Phase2 Data . . . . .	115



---

## List of Tables

4.1. Luminosity at Belle II . . . . .	27
6.1. Cluster Splitting Examples . . . . .	36
6.2. Energy Sum In The ECL Examples . . . . .	37
6.3. Cut Efficiencies . . . . .	39
6.4. Areas Of Interest Different Momenta Ranges . . . . .	46
6.5. Areas Of Interest Different Transverse Momenta Ranges . . . . .	47
6.6. Different (Transverse-) Momenta Ranges For $\theta$ Efficiency . . . . .	47



---

## Bibliography

- [1] Michael Riordan Max Dresden Lillian Hoddeson Laurie Brown.  
*The Rise of the Standard Model: Particle Physics in the 1960's and 1970's.*  
Cambridge University Press, 1997.  
ISBN: 0521578167.
- [2] *Fundamental Particles.*  
URL: <https://www.universetoday.com/tag/fundamental-particles/>.  
visited on 20.05.2019.
- [3] Frederick Reines.  
“40 years of neutrino physics”.  
In: *Progress in Particle and Nuclear Physics* 32 (1994), pp. 1 –12.  
ISSN: 0146-6410.  
URL: <http://www.sciencedirect.com/science/article/pii/0146641094900035>.
- [4] C Sivaram.  
“What is special about the planck mass?”  
In: *arXiv preprint arXiv:0707.0058* (2007).  
URL: <https://arxiv.org/abs/0707.0058>.
- [5] Thomas Hambye.  
“CP violation and the matter–antimatter asymmetry of the Universe”.  
In: *Comptes Rendus Physique* 13.2 (2012). Flavour physics and CP violation / Physique de la saveur et violation de CP, pp. 193 –203.  
ISSN: 1631-0705.  
URL: <http://www.sciencedirect.com/science/article/pii/S1631070511001873>.
- [6] Daniel V. Schroeder.  
*Feynman Diagrams and Electron-Positron Annihilation.*  
Oct. 2002.  
URL: <https://physics.weber.edu/schroeder/feynman/>.  
visited on 27.05.2019.
- [7] E. Kou et al.  
*The Belle II Physics Book*.

## Bibliography

- Aug. 2018.  
URL: <https://arxiv.org/abs/1808.10567>.
- [8] Abe et al.  
“Achievements of KEKB”.  
In: *Progress of Theoretical and Experimental Physics* 2013.3 (Mar. 2013).  
ISSN: 2050-3911.  
DOI: 10.1093/ptep/pts102.  
eprint: <http://oup.prod.sis.lan/ptep/article-pdf/2013/3/03A001/4440618/pts102.pdf>.  
URL: <https://dx.doi.org/10.1093/ptep/pts102>.
- [9] Ivan Heredia de la Cruz.  
“The Belle II experiment: fundamental physics at the flavor frontier”.  
In: *Journal of Physics: Conference Series* 761 (Sept. 2016).  
DOI: 10.1088/1742-6596/761/1/012017.
- [10] Akemoto et al.  
“The KEKB injector linac”.  
In: *Progress of Theoretical and Experimental Physics* 2013.3 (Mar. 2013).  
ISSN: 2050-3911.  
DOI: 10.1093/ptep/ptt011.  
eprint: <http://oup.prod.sis.lan/ptep/article-pdf/2013/3/03A002/4441335/ptt011.pdf>.  
URL: <https://dx.doi.org/10.1093/ptep/ptt011>.
- [11] Werner Herr and Bruno Muratori.  
“Concept of luminosity”.  
In: (Feb. 2006).  
DOI: 10.5170/CERN-2006-002.361.
- [12] Fernando Abudinén.  
“Development of a  $B^0$  flavor tagger and performance study of a novel time-dependant  $CP$  analysis of the decay  $B^0 \rightarrow \pi^0\pi^0$  at Belle II”.  
PhD Thesis. Ludwig-Maximilians-Universität München, Sept. 2018.
- [13] Abe et al.  
“Belle II Technical Design Report”.  
In: (Nov. 2010).  
URL: arXiv:1011.0352.
- [14] *Electrons and Positrons Collide for the first time in the SuperKEKB Accelerator*.  
Apr. 2018.  
URL: <https://www.kek.jp/en/newsroom/2018/04/26/0700/>.  
visited on 25.02.2019.
- [15] Sara Pohl.  
“Track Reconstruction at the First Level Trigger of the Belle II Experiment”.  
PhD Thesis. Ludwig-Maximilians-Universität München, Dec. 2017.

## Bibliography

- URL: <https://edoc.ub.uni-muenchen.de/22085/>.
- [16] Nobuhiro Shimizu.  
“Development of the Silicon Vertex Detector for Belle II experiment”.  
Department of Physics, University of Tokyo.  
URL: [http://hep.phys.s.u-tokyo.ac.jp/?page\\_id=229](http://hep.phys.s.u-tokyo.ac.jp/?page_id=229).  
visited on 25.02.2019.
- [17] F. Bernlochner et al.  
“Online Data Reduction for the Belle II Experiment using DATCON”.  
In: (Sept. 2017).  
DOI: 10.1051/epjconf/201715000014.  
URL: <https://arxiv.org/abs/1709.00612>.
- [18] C. Marinas and M. Vos.  
“The Belle-II DEPFET pixel detector: A step forward in vertexing in the superKEKB flavour factory”.  
In: *Nuclear Instruments and Methods in Physics Research Section A: Accelerators, Spectrometers, Detectors and Associated Equipment* 650.1 (2011). International Workshop on Semiconductor Pixel Detectors for Particles and Imaging 2010, pp. 59 –63.  
ISSN: 0168-9002.  
DOI: <https://doi.org/10.1016/j.nima.2010.12.116>.  
URL: <http://www.sciencedirect.com/science/article/pii/S0168900210028962>.
- [19] Belle II Italian collaboration.  
*Silicon Vertex Detector*.  
Mar. 2019.  
URL: <https://web.infn.it/Belle-II/index.php/detector/svd>.  
visited on 06.03.2019.
- [20] Thomas Bergauer.  
“The silicon vertex detector of the Belle II experiment”.  
In: *PoS* (2010), p. 044.
- [21] Thomas Hauth.  
*Pattern Recognition at Belle II*.  
Dec. 2016.
- [22] PA Cerenkov.  
“PA Cerenkov, Phys. Rev. 52, 378 (1937).”  
In: *Phys. Rev.* 52 (1937), p. 378.
- [23] E. Torassa.  
“Particle identification with the TOP and ARICH detectors at Belle II”.

## Bibliography

- In: *Nuclear Instruments and Methods in Physics Research Section A: Accelerators, Spectrometers, Detectors and Associated Equipment* 824 (2016). Frontier Detectors for Frontier Physics: Proceedings of the 13th Pisa Meeting on Advanced Detectors, pp. 152 –155.  
ISSN: 0168-9002.  
URL: <http://www.sciencedirect.com/science/article/pii/S0168900215013789>.
- [24] V. Aulchenko et al.  
“Electromagnetic calorimeter for Belle II”.  
In: *Journal of Physics: Conference Series* 587 (2015), p. 012045.  
DOI: 10.1088/1742-6596/587/1/012045.  
URL: <https://doi.org/10.1088%2F1742-6596%2F587%2F1%2F012045>.
- [25] William R Leo.  
*Techniques for nuclear and particle physics experiments: a how-to approach.*  
Springer Science & Business Media, 2012.  
DOI: 10.1007/978-3-642-57920-2.
- [26] T. Aushev et al.  
“A scintillator based endcap K L and muon detector for the Belle II experiment”.  
In: (Apr. 2015).  
DOI: 10.1016/j.nima.2015.03.060.  
URL: <https://arxiv.org/abs/1406.3267v3>.
- [27] Yoshihito Iwasaki et al.  
“Level 1 trigger system for the Belle II experiment”.  
In: *2010 17th IEEE-NPSS Real Time Conference*.  
IEEE. 2010,  
Pp. 1–9.
- [28] Filippo Dattola, Lorenzo Vitale, and Diego Tonelli.  
“Tracking studies for the Belle II detector”.  
Presented on 20 07 2018.  
PhD thesis. Trieste: University of Trieste, 2018.
- [29] Andreas Moll.  
“The Software Framework of the Belle II Experiment”.  
In: *Journal of Physics: Conference Series* 331.3 (2011), p. 032024.  
DOI: 10.1088/1742-6596/331/3/032024.  
URL: <https://doi.org/10.1088%2F1742-6596%2F331%2F3%2F032024>.
- [30] Rod Pierce.  
“Triangular Number Sequence” *Math Is Fun*.  
Nov. 2018.  
URL: <http://www.mathsisfun.com/algebra/triangular-numbers.html>.  
visited on 27.05.2019.
- [31] *Trigger Bit Table*.

## Bibliography

- June 2019.  
URL: <https://confluence.desy.de/display/BI/TriggerBitTable>.  
visited on 22.08.2019.
- [32] *TEfficiency Class Reference*.  
2019.  
URL: <https://root.cern.ch/doc/master/classTEfficiency.html>.  
visited on 09.10.2019.
- [33] Robert Oerter.  
*The theory of almost everything - The Standard Model*.  
2006.  
ISBN: 978-1-101-12674-5.
- [34] "Doreen Wackerlo".  
*"Cross Section"*.  
Mar. 2001.  
URL: "<https://ed.fnal.gov/painless/htmls/cross.html>".  
visited on 08.08.2019.